TECHNISCHE UNIVERSITÄT MÜNCHEN

Lehrstuhl für Nukleartechnik

Computational Simulations of Direct Contact Condensation as the Driving Force for Water Hammer

Sabin-Cristian Ceuca

Vollständiger Abdruck der von der Fakultät für Maschinenwesen
der Technischen Universität München zur Erlangung des akademischen Grades eines

Doktor-Ingenieurs (Dr.-Ing.)

genehmigten Dissertation.

Vorsitzender:	Univ.-Prof. dr. ir. Daniel J. Rixen
Prüfer der Dissertation:	1. Univ.-Prof. Rafael Macián-Juan
	2. Univ-Prof. Dr.-Ing. Michael Schlüter,
	Technische Universität Hamburg-Harburg

Die Dissertation wurde am 24.06.2014 bei der Technischen Universität München
eingereicht und durch die Fakultät für Maschinenwesen am 27.04.2015 angenommen.

Abstract

An analysis, based on Computer Simulations of the Direct Contact Condensation as the Driving Force for the Condensation Induced Water Hammer phenomenon is performed within this thesis. The goal of the work is to develop a mechanistic HTC model, with predictive capabilities for the simulation of horizontal or nearly horizontal two-phase flows with complex patterns including the effect of interfacial heat and mass transfer. The newly developed HTC model was implemented into the system code ATHLET and into the CFD tools ANSYS CFX and OpenFOAM. Validation calculations have been performed for horizontal or nearly horizontal flows, where simulation results have been compared against the local measurement data such as void and temperature or area averaged data delivered by a wire mesh sensor.

Contents

List of Figures

List of Acronyms

AEKI Atomic Energy Research Institute

ATHLET Analysis of Thermal-Hydraulics and LEaks

BC Boundary Condition

BWR Boiling Water Reactor

CEL CFX Expression Language

CFD Computational Fluid Dynamics

CFL Courant-Friedrich-Levy Number

CIWA Condensation Induced WAter Hammers

CIWH Condensation Induced Water Hammer

CV Control Volume

DCC Direct Contact Condensation

ECCS Emergency Core Cooling System

FSI Fluid-Structure Interaction

FZD Forschungszentrum Dresden Rosendorf

GRS Gesellschaft für Anlagen- und Reaktorsicherheit

HFKI Hungarian Academy of Sciences

HTC Heat Transfer Coefficient

IAD Interfacial Area Density

IAPWS International Association for the Properties of Water and Steam

LDA Laser Doppler Anemometer

LES Large Eddy Simulation

LOCA Loss of Coolant Accident

LSM Level Set Method

LWR Light Water Reactors

MaSE Macro Scale Eddies

MiSE Micro Scale Eddies

NPP Nuclear Power Plant

OpenFOAM Open Source Field Operation and Manipulation

PDE Partial Differential Equation

PISO Pressure Implicit with Splitting of Operators

PTS Pressurized Thermal Shock

PWR Pressurized Water Reactor

RANS Reynolds Averaged Navier-Stokes

RHS Right Hand Side

RPV Reactor Pressure Vessel

SG Steam Generator

SRP Surface Renewal Period

SRT Surface Renewal Theory

SST Shear Stress Transport

TKE Turbulent Kinetic Energy

TUHH Technische Universität Hamburg-Harburg

TUM Technische Universität München

UMSICHT Frauenhofer Institut für Umwelt-, Sicherheits- und Energietechnik

UNIBW Universität der Bundeswehr München

USNRC U.S. Nuclear Regulatory Commission

VOF Volume Of Fluid

VVER Water-Water Power Reactor

WMS Wire Mesh Sensor

Dimensionless Numbers

At Atwood Number

Fr Froude Number

Ja Jakob Number

Pr Prandtl Number

Re Reynolds Number

Roman Symbols

a Speed of sound

a_i Interfacial area density

$A_{interface}$ Interfacial area

c_p Specific heat capacity

D Pipes inner diameter

e Pipe wall thickness

E Young's modulus of the pipe wall

g Gravitational acceleration

h Enthalpy

HTC Heat transfer coefficient

I Turbulence intensity

j Superficial velocity

k Turbulent kinetic energy

K Bulk modulus, i.e. the inverse value of the compressibility

L_t Turbulent eddy length scale

n Normal vector to the interface

p Pressure

Q Volumetric flow rate

q Heat flux

S Source term

t Time

t_{rp} Surface renewal period

T Temperature

U Velocity

V Volume

V_t Turbulent eddy velocity scale

Sub Scripts

1 Liquid

2 Gas

eff Effective

c Compression

g Gas

i Interfacial

k Phase index

liq Liquid

max Maximum

mix Mixture

rel Relative

sat Saturation

t Turbulent

x Component along the x axes

y Component along the y axes

z Component along the z axes

Super Scripts

$\rightarrow$ Vector

$-$ Average value

$MaSE$ Macroscopic eddies

$MiSE$ Microscopic eddies

$\prime$ Fluctuating component

t turbulent

tot total

Greek Symbols

α Volumetric gas fraction or thermal diffusivity

ϵ Eddy dissipation rate

Δ Difference

γ Volumetric liquid fraction

Γ Phase exchange rate

κ Surface curvature

λ Thermal conductivity

μ Dynamic viscosity

ν Kinematic viscosity

ω Turbulent frequency

ρ Density

σ Surface tension

τ Interfacial friction

Acknowledgment

The following work was performed during my stay at the Department of Nuclear Engineering at the Technische Universität München as part of the *CIWA* project funded by the German Federal Ministry of Education and Research *BMBF*, under the reference number 02NUK011E, which I would like to thank at this point.
First of all I would like to send special thanks to my two supervisors namely Univ-Prof. Rafael Macián-Juan PhD, for giving me the opportunity to do this research work at the TUM and being a constant source of support and Univ-Prof. Dr.-Ing. Michael Schlüter from TUHH, for his continuous support and the scientific input for my work. I would like to thank Prof. dr. ir. Daniel Rixen for kindly taking the role of commission chairman. Special thanks go out to the entire staff of the department, technical or administrative, to all my students and to all the people I met who influenced this work as well as to all the other fellow researchers at the department; I know, I have put your patience to a test, when talking to you about the problems encountered in my research and every day life. My best thoughts go out to all *CIWA* project partners, with whom I have enjoyed sharing the time with during interesting project meetings and helpful discussions. I also want to mention the very helpful and supportive conversations with many of the GRS staff, related to the implementation of the hybrid model in ATHLET: Dr. H. Austregesilo, Mr. G. Lerchl and Mr P. Schöffel, just to name the main contributors. Working with all of You in such an environment was a great pleasure and contributed a lot to this work.
Looking back at the years spent to accomplish this work, one realizes that in life not everything lies in our own hands. At this point I want to mention and to

commemorate two experts that accompanied this work for only a too short time: Univ-Prof. Dr.-Ing. Erik Pasche from TUHH, whom I had the honor to meet if only briefly at the beginning of my work and Dipl.-Ing. Harald Swidersky from TÜV SÜD, to whom I am grateful for the time we worked together, for his support and advice both invaluable and difficult to express in words.
Last but not least I would like to thank my family, especially my parents, my brother, my 'Munich based family' and to all my friends for their continuous understanding and support. Special thanks go to my beloved girlfriend *Olivia* I would like to thank her, for the ongoing encouragement, as she was a very important drive for this work.

To all of You I can only say: *Vă mulţumesc!*

Chapter 1

Introduction

Simultaneous interfacial heat and mass transfer due to condensation or evaporation is a commonly encountered phenomenon in many systems through various industrial applications. Accurate simulation models are of particular importance in industries where higher safety standards are applied, as in the case of the nuclear and chemical industries. The realistic modeling of the interfacial heat and mass transfer phenomenon is a key goal for best estimate simulations of Condensation Induced Water Hammer (CIWH). The prompt and potentially violent CIWHs events generate locally additional mechanical loads. If these loads are not considered, during the designing phase of that component, they can potentially result in mechanical component failure. Experiments have highlighted the destructive force of such pressure surges, especially in the low pressure levels, where peaks more than 10 times higher than the system pressure have been measured. In the past a lot of effort has been put on the development of avoidance and mitigation guidelines for the CIWH phenomenon. Recently guidelines have even been released for the avoidance of CIWH events in thermal solar plants.

The danger of CIWH events in nuclear power plants was already highlighted by the U.S. Nuclear Regulatory Commission (USNRC) in the 1970's, getting in the spotlight after the incident at the Nuclear Power Plant Indian Point No. 2. The ability to analyze the complex dynamic two-phase flow behavior with computer

system codes is an integral part of any safety assessment study in which detailed scenarios such as the postulated Loss of Coolant Accident (LOCA) or loss of off-site power are analyzed. During a LOCA event, subcooled water can be injected by the Emergency Core Cooling System (ECCS), into the pipe network of the primary power plant loop, counter-currently to the gas phase exiting the reactor pressure vessel. A CIWH can under certain circumstances arise during an off-site power loss, an event expected to occur at least once during the life time of the nuclear power plant. During the loss of off-site power, depending on the steam generator feed-water inlet design, auxiliary *cold* water can be injected through a horizontal pipe into the steam generator. If this steam generator has a low enough liquid level a water hammer event can be triggered by direct contact condensation. CIWH potentially occurs in any one-component two-phase flow whenever an entrapped gas bubble suddenly collapses due to high turbulence and due to a sufficiently high liquid phase subcooling. As underlined within this work, Direct Contact Condensation (DCC) can independently act as the main driving force for flow pattern changes in horizontal or nearly horizontal flow. The difference in the phase densities between the vapor and the liquid results in local depressurization and in the acceleration of the liquid phase which has to fill the void of the condensed steam thus enhancing the Kelvin-Helmholtz instability. The present work focuses on the two-phase flow of liquid water and steam, as water is still one of the most widely used working fluid in the field of commercial energy production. Examples of famous investigations for CIWH for working fluids different than water were done by Martin et al., [13].

Complex dynamic mechanisms in the interactions between the two-phases present in two-phase flow have to be considered in realistic computer simulations. Computer simulations are currently intensively used in deterministic safety assessments or during the designing phase of industrial scale facilities. Depending on the desired results accuracy, two computing approaches are commonly used: system code or computational fluid dynamics simulations. The system codes are fast running computer codes, which can perform full-system analysis employing relatively

coarse computational grids. The spatial resolution of their results is good enough to understand the overall system behavior. If more local and physically accurate results are needed, then high resolution resource intensive Computational Fluid Dynamics (CFD) simulations have to be employed. The relatively large computational resources required by CFD simulations limit their applicability to full system behavior analysis. Interfacial momentum, heat and mass exchange are described in computer codes based on so called closure laws. In the particular case of DCC, which occurs on the interface separating the phases key variables to be modeled by a computer code in order to correctly capture the phase change are the HTC and the Interfacial Area Density (IAD). The temperature and enthalpy difference required for the calculation of the condensation rate results after solving the conservation equations. The present work focuses on the mechanistic modeling of the HTC and presents the development of a new hybrid model. This hybrid model takes into consideration the effect of turbulent eddies on the structure of the two-phase flow. In order to assess its performance, this new model is implemented into two CFD codes, ANSYS CFX and Open Source Field Operation and Manipulation (OpenFOAM) and one system code, ATHLET. A validation of the hybrid HTC model together with the Volume Of Fluid (VOF) approach for CFD simulations and with the two-fluid model for the system code simulation will be presented for a set of experiments performed at three different facilities.

Outline of the Thesis

The thesis contains the following five major sections:

- Chapter 2 gives a general description of the two-phase flow dynamics, focusing on horizontal and nearly horizontal flow channels. Typical flow patterns emerging in such channels will be presented with special emphasis on those relevant for the description of the particular type of water hammers, driven by direct contact condensation. Some dimensionless numbers, used for a later analysis of the influence of particular parameters on the occurrence and magnitude of the condensation induced water hammer, will also be introduced within this chapter.

- Chapter 3 gives an overview on the computational tools later used in chapter 6, for the simulation of two-phase flow with heat and mass transfer. This chapter also includes the description of the conservation equations employed by the models and the description of the mechanistic HTC approach based on the surface renewal theory.

- The development work of the new hybrid HTC is presented in chapter 4. After the new model is set up, its implementation into the used CFD tools and the system code is presented. The threshold for the dynamic switch of the hybrid HTC model is calibrated based on the measurement data acquired in a quasi-steady state experiment.

- Chapter 5 includes the description of the experimental facilities which delivered the measurement data used for the assessment of the developed HTC model. Special focus is set on the geometric set-up of the core part, the test-section and the particularities of the installed data acquiring system at each facility.

- The 6th chapter contains the simulation results of the computer calculations. In total, 36 different experiments have been simulated for the assessment of the hybrid HTC model, 33 experiments have been simulated with the system code and 4 experiments have been simulated with the CFD codes.

Chapter 2

Horizontal and nearly Horizontal Two-Phase Flow Dynamics

A short overview will be given in this chapter on the two-phase flow dynamics, the possible complex flow configuration of two-phase flow, the flow patterns and the effect of DCC on the two-phase flow dynamics in a horizontal or nearly horizontal channel. This chapter introduces the theoretical background required for the analysis of a horizontal or nearly horizontal two-phase flow. A general overview of the different types of water hammer phenomena will also be presented within this chapter. Special emphasis will be put on the particular case of water hammer driven by the contact condensation phenomenon.
Within this work, experiments of horizontal or nearly horizontal two-phase flow between saturated steam and subcooled water will be analyzed. Due to this reason only horizontal or nearly horizontal two-phase flow patterns will be introduced and discussed in the next chapters.

2.1 Introduction to Two-Phase Flow Dynamics

The understanding and the study of multiphase flow is of great importance in many technological applications, especially in industrial facilities. In particular

two-phase flows consisting of a liquid and a gas phase are found in many industries, such as power production, chemical and petro-chemical installations, process engineering, lubrication systems and environmental control including meteorological phenomena, etc.[14]. A correct understanding and modeling of the physics of two-phase flow plays a very important role during the design phase of new equipment and in the assessment of the safety and efficiency of its operation.
One of the most important areas in which two-phase flow dynamics is of special relevance is in power systems engineering. Heat and mass transfer processes are crucial in the performance of power plants. The nuclear industry in particular is very active in the development of detailed and reliable two-phase flow models that can be implemented into computer codes and used for the assessment of thermal-hydraulic systems. Large increases in computational power in the recent past have facilitated the development of sophisticated computer programs capable of simulating the behavior of entire plants in two-phase flow conditions, while considering the complex heat, momentum and mass transfer mechanisms between the phases and between these and the systems components.

The need for even more accurate simulations of the behavior of complex fluid based systems, in which multiphase conditions play a crucial role in defining the operation and safety of fluid based systems, has been a strong drive for research and development aiming for a better understanding of the two-phase flow phenomenon. This has led to the development of more mechanistic models, based on physical principles, rather than empirical correlations based on relatively simple adjustments of measured data that can then be implemented into computer codes. This trend has accelerated with the need for an increase in the operational safety and in the efficiency, which can result in an optimized use of the natural resources in industrial systems. Even more, in the safety oriented nuclear industry, state-of-the-art two-phase models are required in order to enhance the safety of a facility and thus to decrease the risk of potential accidents.

2.2 Horizontal or nearly Horizontal Two-Phase Flow Patterns

Horizontal or nearly horizontal pipes are used in many industrial facilities, such as power plants, chemical and petro-chemical installations, thermo-solar parks, process facilities, etc.

The phase distribution within a flow channel with two-phase flow is one of the most important aspects of its description. Flow regime maps have been historically developed in order to more easily characterize two-phase flow dynamics [15]. These maps determine the structure and morphology of the flow as a function of variables such as characteristic phase velocities, mass fluxes, void fractions, etc. that delimit specific regions in the map with similar phase distribution characteristics: the so-called flow regimes. Flow regime maps are empirically developed and therefore, depend to a certain extent on the geometrical set-up of the facility on which the experiments have been conducted, on the thermo-physical properties of the working fluid or fluids used and on the volumetric phase concentration within the experimental section of the channel.

In particular, horizontal or nearly horizontal two-phase flow patterns usually show a clear phase separation caused by the influence of the gravitational force on the phases with different densities. If the inclination angle formed with the horizontal axis is only a few degrees ($< 5°$), the influence of the gravity on the phase distribution is only limited. Thus a common practice is to use adapted horizontal flow patterns for slightly inclined flow channels, mainly because very few flow-regime maps are available in the literature that account for every possible pipe inclination. The lack of available flow regime maps for nearly inclined pipes is partially due to the practical impossibility of creating these maps for every desirable inclination. Still some important experimental investigations have been performed for inclined pipes with upward flow by Weisman and Kang [16] and by Barnea et. al[17].

In the present thesis two-phase flow of subcooled liquid water and saturated steam together with the phenomenon of CIWH in horizontal or slightly inclined pipes is analyzed. Therefore, only flow regimes for such inclinations will be discussed

next. The schematic representation of the most characteristic flow patterns for horizontal two-phase flow are shown in figure 2.1. In the literature different terminology has been used by different authors for the characterization of the flow patterns based on the void fraction distribution in the flow channel [2], resulting in different terminologies for the similar flow patters. These flow patterns apply also to slightly inclined pipes, such as those considered later in chapter 6. In figure 2.1 the white color represents the gaseous phase, whereas the blue color stands for the liquid phase. Generic, theoretical flow configurations will be presented for a simplified 2D case.

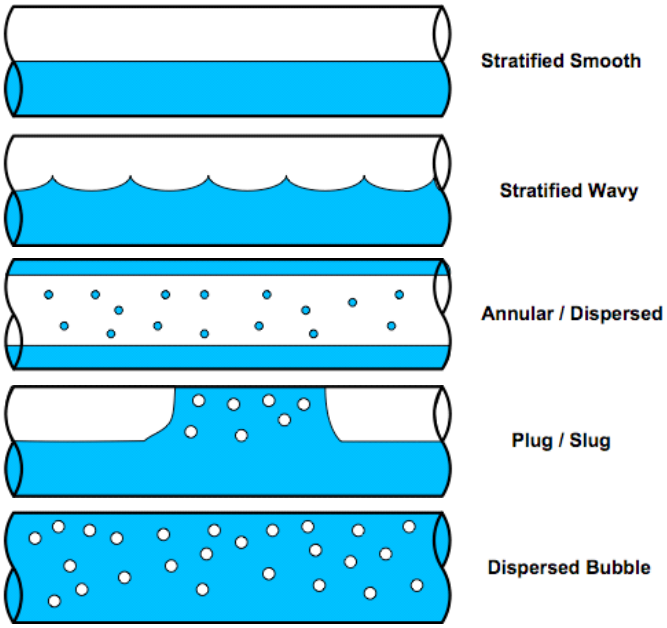

Figure 2.1: Schematic representation of typical flow patterns for horizontal two-phase flow [1]

Traditional methods of flow pattern identification, applicable to all possible flow regimes, include in increasing order of their complexity: visual observation, pressure fluctuations measurement, electrical tomography and photon attenuation. The simplest technique, the visual observation, requires only a transparent test rig and is consequently limited in the pressure and temperature ranges in which it can be employed. Another drawback of this method lies in the subjective identification of the patterns. The technique consisting in the measuring of pressure

fluctuations can be applied to a broader range of pressures and temperatures, with the price of losing the optical investigation possibility because of the use of metallic, opaque pipes. The more sophisticated and expensive photon attenuation technique can still give an insight into opaque pipes. Electrical tomography is a method of area averaged phase tracking with the major drawback typical to all flow invasive measurement techniques of perturbing the flow. Still it is a widely used method, which can deliver useful results with the high temporal and spacial resolution required for the validation of CFD-codes for two-phase flow conditions.

Variables often used as parameters in the axes of flow regime maps include: the volumetric phase concentration also referred to as the void fraction defined in the equation (2.1), where V represents the volume; and the phasic gas and liquid superficial velocities, as defined in the equation (2.2), where Q_k represents the volumetric flow rate of phase k, A represents the cross-section area and U_k is the velocity of phase k. The void fraction, can be computed as a volumetric or an area averaged value, and represents the amount of gaseous phase in the region where it is computed. Equation (2.1) presents the volumetric averaged void fraction, as it is used also in the finite volume computer codes, later employed for the simulation of two-phase flow with DCC in chapter 6. The superficial velocity j_k describes the hypothetical velocity of a specific phase k, as if it flowed alone in the entire channel shared by the two phases. The superficial velocity can be calculated as the ratio between volumetric flow rate of the phase k and the entire channel cross-sectional area or by forming the product between the phase k fraction multiplied by its phase velocity.

$$\alpha = \frac{1}{V} \iiint_V \alpha dV = \frac{V_g}{V} \tag{2.1}$$

$$j_k = \frac{Q_k}{A_{channel}} = \alpha \cdot U_k \tag{2.2}$$

The most known and still most used flow regime maps in order of their publication date are: the one developed by Baker [18], Mandhane's et al. [19] and Taitel and Dukler's [20].

Baker's experimental investigations for adiabatic horizontal flows, resulted in the design of one of the first flow regime maps, [18]. He stressed the influence of the flow pattern on pressure losses and heat and mass transfer in tubes. The two axes of his map consider the superficial phase-velocity and some additional parameters accounting for the influence of the thermo-physical properties of the fluids, in order to offer extrapolation capabilities to other combinations of working fluids. The map was developed using experimental data from large diameter pipes of adiabatic air-water or water-oil flow.

The Mandhane et al. flow regime map was developed for low system pressure conditions with small gas density changes [19]. Mandhane et al. consider that the influence of the thermo-physical properties on the flow pattern is not that strong as stated by Baker, [19]. This map builds up on the Baker map, but neglects the pipe diameter, resulting in a map with limited applicability even if a large database of measurements of adiabatic air-water flow was used for its development.

Perhaps the most used and implemented horizontal two-phase flow regime map in computer codes is the Taitel and Dukler map [20]. They developed a flow regime map after realizing, based on the comparison of different available maps, that sometimes big discrepancies exist between these maps, especially in the transition regions. Using a more theoretical approach, Taitel and Dukler combined the influences of the thermo-physical properties, the gravitational acceleration, the pressure gradient, phase velocities, channel inclination and channel geometry in a more mechanistic model.

A short characterization of the main flow patterns for horizontal or nearly horizontal two-phase flow will be defined based on the flow regime map developed by Mandhane et al. [19] and represented in figure 2.2. Mandhane et al. initially developed this map for adiabatic flow conditions within a channel with a circular cross section. Starting from low volumetric fluxes and going in a counter-clockwise direction in the map, the following major patterns are identified: stratified, (strat-

ified) wavy, annular, slug, plug and bubbly flow.

Each flow pattern is characterized as follows:

- *Stratified* - possible only at low volumetric fluxes for both phases. Gas flows on top of the liquid creating a smooth interface.
- *(stratified) Wavy* - possible at low liquid and slightly higher gas volumetric fluxes. Gas flows on top of the liquid creating a wavy interface. Kelvin-Helmholtz instability gives rise to surface waves. This regime can act as a transition to slugging.
- *Annular* - possible for high gas and moderate liquid volumetric fluxes. The gas creates a core within the liquid and flows in the center of the pipe, while the liquid creates a film with varying thicknesses, close to the channel walls. The gas core has a considerably higher velocity in comparison to the liquid film. Surface waves are almost always present on the liquid film, due to shear effect caused by the gaseous bulk.
- *Slug* - possible for moderate volumetric fluxes for both phases. Characterized by the intermittent flow of liquid masses which isolate gas pockets. The liquid masses travel approximately with the gas velocity. Slug flow includes liquid flowing downstream and upstream from the location where the slug is created.
- *Plug* - possible at moderate liquid and low gas volumetric fluxes. Similar to the slug flow but characterized by a higher flow dynamics. Formed usually by coalesced slugs.
- *Bubbly* - possible at high liquid and gas volumetric fluxes. Dispersed flow of various gas bubbles sizes in the continuous liquid core. High turbulence in the liquid side leads to the break-up of the large gas pockets into smaller bubbles.

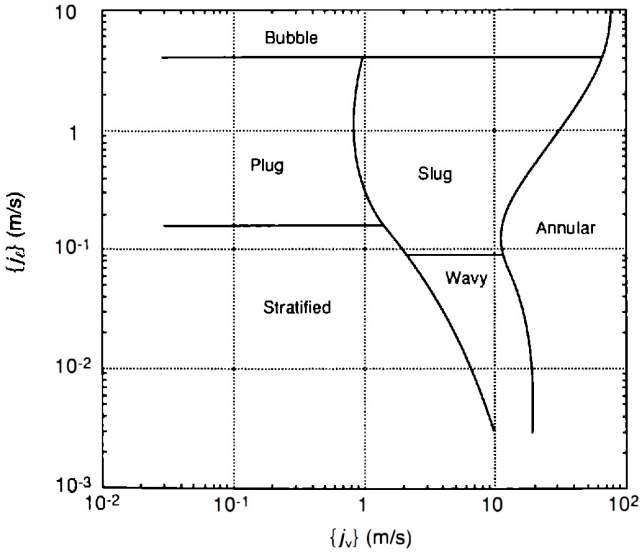

Figure 2.2: The Mandhane et al. horizontal flow regime map [2]

The regime map based on a mechanistic model rather than on visual observation presented by Taitel and Dukler [20], considers *(only)* the following flow patterns: smooth stratified, wavy stratified, intermittent flow (including slug, plug and elongated bubble flow), annular flow with entrapped liquid and dispersed bubble flow. A mechanistic description, i.e. based on physical concepts, for the departure from horizontal separated flow pattern is the Kelvin-Helmoltz instability which describes the wave amplitude growth at the interface of the two phase mixture.

The onset of intermittent flow is described by Taitel and Dukler as the moment when finite amplitude wave will grow on the stratified interface [20]. This leads to a local liquid level rise that potentially reaches the top of the pipe, thus blocking the gas flow. In this situation slug or plug flow is induced, depending on the liquid level. If the gas rate is high enough, annular flow is induced as the liquid wave is swept away and a gas bulk is formed with a liquid around the pipe walls. The criteria defined by Taitel and Dukler for the onset of intermittent flow is a balance between the Bernoulli effect and the gravity. As a wave is built up, gas is accelerated, leading to the growth of wave. This comes as an opposing effect to

the wave decreasing effect of the gravitational acceleration. The presentation of the characteristic patterns in a horizontal two-phase flow was presented based on the Mandhane flow regime map, because the axis of the Taitel and Dukler map depend on the flow conditions, the geometric set up of the flow channel and on the thermo-physical properties of the fluids.

The Taitel and Dukler flow regime map was developed for adiabatic flow conditions but is widely applied to diabatic flow regimes.
Since these maps have been developed under adiabatic conditions, it is difficult to account for the effect of phase change onto the two-phase flow dynamics. The literature presents some examples of flow regime maps where the effect of phase change has been included within heat exchangers. Extensive research was also done for refrigeration agents in small diameter tubes. One of the first studies was carried out by Haraguchi et al. [21] later, work was done and published by the group of Cavallini, Thome and El Hajal [22], [23], [24], [25]. Within these publications phase change occurs preponderantly at the flow channel walls and not, as in the case of the analyzed DCC in this thesis, at the two-phase interface. Section 2.3 will present the influence of phase change in two-phase flow dynamics, while chapter 6 will highlight this influence based on computer simulations.

2.3 The Influence of Phase Change on Horizontal or nearly Horizontal Two-Phase Flow Dynamics

The DCC describes a phase change that takes place at the interface of direct contact between the liquid and vapor phases. The interface is assumed to be at saturation conditions, whereas the liquid and/or the steam can be away from saturation. Thermal equilibrium is locally assumed and the interface is not considered to add any resistance to the heat and mass transfer between the phases.
Interfacial heat and mass transfer, such as the DCC, is encountered in many in-

dustrial systems. It is of particular importance in the nuclear power and chemical installations. DCC is a phenomenon which can appear in any system-component with a single component two-phase flow. This phenomenon can appear with any combination of a liquid and its vapor under thermal non-equilibrium conditions. In the power generation industry water is the most often used work fluid, but DCC can also occur in refrigeration systems or petro-chemical installations with other fluids.
The modeling of DCC must consider several key parameters that describe the macroscopic phase change phenomena, such as the local heat transfer coefficient HTC, the area of contact between both phases (interfacial area), and the subcooling of the liquid phase. The first two parameters have to be correctly predicted by using special models in computer simulations, while the last one is a direct consequence of solving the conservation equations with a strong feedback from the first two parameters.

The effect of the condensation process on the IAD is opposed to the case of vaporization because the interfacial area density tends to decrease, as condensation damps the interfacial ripples [15].
In the case of vaporization (boiling), the formation of bubbles and the bubble induced turbulence and bubble break-up mechanisms tend to increase the interfacial area available for heat and mass transfer between the phases. The decrease of phase contact surface in DCC reduces the phasic interchange of energy and mass and has an influence on the overall condensation rate, which in turn, determines the magnitude of the pressure spikes in CIWH situations.
An example of scenarios in which DCC plays an important role is during a postulated LOCA in a Nuclear Power Plant (NPP) especially during the re-flooding stage as subcooled water is injected by the Emergency Core Cooling System (ECCS) into the primary side pipes and it flows counter-currently to the steam exiting the reactor core. Accurate safety related simulations of the re-flooding stage of a LOCA, require models that can predict high condensation rates as correctly as possible, particularly at locations close to the injection point of the ECCS or

in areas of high flow turbulence which, together with a high sub-cooling of the water in contact with the saturated or superheated steam can lead to sudden flow regime changes and very fast condensation of the steam. The analysis of the local effects during the re-flooding stage of the LOCA is very complex due to the highly dynamic character of the two-phase flow. A reliable prediction of the transient flow patterns is required, in addition to the correct modeling of the heat and mass transfer processes over the wide range of flow patterns.
A visual investigation on a transparent test-section with a geometry similar to that of the ECCS injection was performed at the Technische Universität Hamburg-Harburg (TUHH) and showed the changes in flow pattern caused by the condensation process. Measurement data from the Universität der Bundeswehr München (UNIBW), the TUHH and the PMK-2 facility in Hungary clearly proved the influence of DCC in two-phase flow dynamics.
Flow patterns that can occur in horizontal or nearly horizontal flow channels can be grouped based on the values of local parameters such as the superficial velocities of the phases and local void fraction. These flow patterns span from stratified to slug flow with entrainment of the disperse phase, which can be both steam bubbles and water droplets depending on the two-phase flow configuration and void fraction. Under certain conditions DCC can also act as the driving force for changes in the flow pattern. The flow regime maps that can be used in such conditions should take into account the influence of local depressurization due to DCC when defining the transition regions on the maps.

A local decrease in pressure within a pipe containing a two-phase mixture caused by phase change can lead to the dangerous, prompt and violent condensation phenomenon also called CIWH. The decreasing pressure can locally change the flow pattern from stratified to slug flow and thus to prompt steam bubble collapse. The phenomenon of CIWH is most destructive at low and intermediate system pressures, because of the high differences in phase density, resulting in a higher flow acceleration potential during the collapsing phase and the release of a larger latent heat. The resulting violent pressure surge adds a supplementary mechanical

load to the system component in which it appears. If this phenomenon was not considered within the designing phase of that component, a mechanical failure is plausible. Such integrity failures can have serious consequences. There is therefore, a large practical interest in the accurate modeling of DCC both during the design phase of safety equipment, as well as part of the periodic system safety assessments of vital components. A more comprehensive overlook over the phenomenon of CIWH will be provided in chapter 2.4.

Recommended models for the computation of the HTC directly linked with turbulence quantities will be presented in chapter 3.5 and chapter 4.

The influence of the condensation rate on the change in the flow pattern, will be presented within the chapter 6.1, when the results of the Surface Renewal Theory (SRT) based HTC models are presented and when the experimental measurement data of the PMK-2 and the TUHH facility will be discussed. It will be shown that DCC can act as the driving force for the change in the flow pattern using the results of computer simulations, both system code and of CFD tools.

2.4 The Phenomenon of Water Hammer

In general a typical water hammer event is a rapid change in pressure resulting in a propagating pressure wave. It appears in pipes or pipe networks and is caused by a rapid change in fluid velocity. This particular change can be the result, for example, of events such as a pump starting or rapid coast-down, the operation of a valve or as a result of DCC. In the literature water hammers have been grouped in categories based on the different water hammer triggering mechanisms. One of the most analyzed water hammer types is the one with column separation, as it can occur in many industrial applications, with a single-phase working fluid. This sub-group of water hammers is characterized by the direct feedback between a rapidly changing fluid velocity and the pressure changes experienced by the fluid as a result. In the case of the CIWH it is the formation of a large bubble of steam

(*slug*) in a horizontal or nearly horizontal pipe, leading to an entrapment of a vapor pocket by subcooled liquid. The fast condensation of the steam bubble creates a vacuum which is rapidly filled by an accelerating liquid traveling towards it. As the bubble collapses, high velocity liquid surfaces collide and create a compressive local pressure spike that propagates along the system.

The typical sequence of a pressure surge scenario is: a triggering event causes a rapid change in flow velocity (deceleration) which induces a rising pressure peak as the fluid's momentum is transformed in pressure energy. The propagation of the pressure peak creates a traveling pressure wave followed by an equal and opposite reflected wave. This reflection can take place either at a forming two-phase interface or at the piping system's structure. If two reflected waves meet, then higher pressures than the initial surge can arise. Eventually, because of energy losses caused by friction and elastic interaction of the fluid with the solid surfaces, the energy of the pressure wave dissipates and the pressure returns to its initial value. If the maximum pressure reached is high enough, the integrity of the system can be compromised by the appearance of cracks or by the bursting of pipe lines and other system components or increase the material fatigue. This may lead to serious consequences of release of pipe contents to the surroundings due to rupture causing eventually environmental and health hazards. The high pressure wave can damage pipe bridges, the pipe mounting system or components such as foundations pumps or valves. The depressurization wave can lead to pipe collapses or to the suction of air or slope water into the main pipe. In the work presented in this thesis, the reflection of the pressure wave has only been considered at the two-phase interface, since no fluid-structure interaction was modeled. The high compressibility rate of the gaseous phase leads to only a minimal pressure oscillation within this phase and results in a fast damping pressure within a short pipe length away from the point of steam bubble collapse.

A method often used to calculate potential water hammers in piping systems, even if it was one of the first developed models, is based on Joukowsky's model presented in equation (2.3). This model directly correlates the maximum pressure variation with the product of the liquid slug velocity variation, the local speed of

sound in the liquid and the local liquid density. The local speed of sound is to be calculated using equation (2.4) as developed by Korteweg [26]. In the calculation of the speed of sound K represents the bulk fluid elastic modulus, which is the inverse value of its compressibility, ρ_{liq} is the liquid density, E represents Young's modulus of the pipe wall's material, D is the pipe's inner diameter, and e is the pipe's wall thickness.

$$\Delta p_{max} = \Delta U \cdot a \cdot \rho_{liq} \tag{2.3}$$

$$a = \sqrt{\frac{K/\rho_{liq}}{1 + (K/E)(D/e)}} \tag{2.4}$$

Joukowsky's model was developed for sudden valve closures, and it therefore, assumes that the time required for the valve closure is smaller than twice the time required by the pressure wave to travel through the entire pipe length. An important factor determining the pressure change is the small compressibility of the liquid. Once a pressure wave is created, it travels through the piping system and can be damped within the liquid mainly by the wall friction.

After Joukowsky published his theory, more complex models were developed and research work was performed by several groups including Allievi [27], Bergeron [28] and Rich [29]. Reiman set the foundation of the analysis of the pressure propagation using the methods of characteristics, which is still a widespread use in the field of water hammer analysis [30], [31].

Traditional system analysis of such scenarios, even before simplified computer codes where available as tools, fully relied on the experience of the designer or facility operator to identify such scenarios. The safety analysis of simple systems, especially if that equipment is vulnerable or accident-prone to water hammers, included the inspection of the system's layout design characteristics, and the expected operating parameter. Relevant system parameters include the operating pressure, temperature and mass flow rates, and the instrumentation and control of key components such as pumps and valves. More complex systems require a more sophisticated pipe network analysis and must rely on the use of computer programs for the simulations of transient scenarios. The simulation of transient

scenarios gives better insights on the onset and evolution of possible water hammer events.

If two-phase flow is to be present at the onset or during the evolution of the water hammer event, the main requirement for such computer programs is the capability to realistically and reliably predict the two-phase flow in complex geometries for various transient scenarios within reasonable computational time. Key variables such as the phase velocity, phase volume fractions and pressures throughout the analyzed system must be accurately predicted by the employed transient analysis computer code. Otherwise, the formation of the pressure wave, its propagation along the system and the maximum pressure values may not be correctly predicted. Still, the evaluation of the computational results by an experienced user remains vital in order to determine the possibility of water hammer in the analyzed system and its severity so that effective pressure surge protection measures can be taken. The consequences of water hammer events in facilities having operated for a certain time are more severe than in newly built facilities, because if water hammers are large enough, the effect of aging, fatigue and corrosion-erosion of the solid structures can lead to cracks or bursting. In aged installations such events have the potential to aggravate many safety problems [32]. Even if the initial pressure spikes may not be large enough, the interaction of the traveling pressure waves with the system-structure-equipment can result in vibrations and even in resonances, which eventually can also lead to system breaks. A worst case scenario would be when water hammer events appear during abnormal or accident situations, thus aggravating the seriousness of the emergency situation.

The main difference between the two groups of the discussed water hammer phenomena, consists in the initiating mechanism: in the case of the water hammer with column separation it is for instance a fast closure of a valve while in the case of the CIWH it is the slug formation in a horizontal or nearly horizontal pipe, leading to an entrapment of a vapor pocket by subcooled liquid.

2.4.1 A Particular Type of Water Hammer Caused by Condensation Induced Flow Transition

Experimental research designed to address the phenomenon of CIWH in detail was initiated by the USNRC in the 1970s after some incidents having this phenomenon as a precursor occurred in nuclear power plants with potentially serious consequences. The first incident in a NPP took place at Indian Point Unit No. 2 in 1973. A feed-water pipe was damaged due to CIWH when subcooled feed-water was introduced into the steam-generator following a low-water-level reactor trip. Steam exited counter-currently from the steam generator and flowed into the feed-water line mixing with the subcooled water flowing inside. After this event, other similar cases have been reported world wide and the topic has become an area of active experimental, theoretical and developmental research, with applications beyond the nuclear industry. This phenomenon is not only a threat to steam-water systems, but also to any system in which a liquid and its vapor flow in a two-phase regime: if vapor of a fluid comes into contact with its subcooled, liquid phase of that component, a CIWH may result. Examples of relevant investigations for CIWH for working fluids different to water have been done, for example, by Martin et al.[13].

As briefly discussed in the previous section, the phenomenon of CIWH potentially occurs in two-phase flow systems whenever an entrapped steam bubble suddenly collapses due to a very large condensation rate caused by high turbulence and sufficiently high subcooling of the liquid phase. The difference in phase specific volumes results in a large local depressurization as the bubble collapses and in the acceleration of the liquid phase that has to fill in the void left empty by the condensing steam. A sufficiently large liquid velocity leads to a pressure surge when the two water fronts meet. A schematic representation of such an event is shown in figure 2.3. This schematic representation shows a horizontal pipe in which water (*blue*) is injected from the left hand side into a steam (*red*) filled pipe. In this case the flow regime changes locally from horizontal stratified to horizontal wavy (*see*

second figure from top). The instability occurs as steam flows counter-currently due to the large condensation rate in contact with the subcooled liquid. The local liquid waves continue to grow and form a slug which completely isolates the steam pocket at the top of the pipe (*third figure in the same sequence).* A sudden condensation of the entrapped steam pocket causes a significant local depressurization because of the high specific volume of the steam. The local pressure in the steam bubble decreases almost to the saturation pressure corresponding to the temperature of the liquid phase [33]. If the pressure decreases enough, additional vaporization can occur. As the steam condenses, water is sucked in to replace its volume (*fourth and fifth figure*). In some cases, the depressurization can even cause the collapse of pipe segments. The acceleration of the water fronts toward each other can lead to a CIWH event as the fronts collide if the steam bubble condensation is fast enough. A high pressure wave is then created, which can harm or burst pipe sections and add mechanical load onto the pipe bends and their supports. The pressure wave hits the free surface in the flow and is either reflected or dissipated if, for example, it encounters a steam bubble swarm. The duration of the resulting forces applied on pipes is very short, yet it may be sufficient to produce structural damage on the pipe or its supports [33].

The depressurization is more pronounced in systems operating at lower pressures because of the larger difference between steam and liquid water specific volumes, thus making CIWH more dangerous when they appear in low pressure systems. This often corresponds to ab-normal operational regimes in NPPs during or after loss of coolant or other kinds of scenarios, but can also be normal non-full power modes of operation. It is important to notice that locally high condensation rates can alone act as the driving force for local two-phase flow pattern changes that may initiate water hammer events. The DCC effect thus enhances the Kelvin-Helmholtz instability.

Early experimental work on the phenomenon of CIWH in test rigs influenced by the needs of the nuclear industry was conducted by Block et al. [34]. His initial experiments, also known as the "water canon experiments" were carried out on a vertical pipe and resulted in the development of mitigation strategies for such events. It

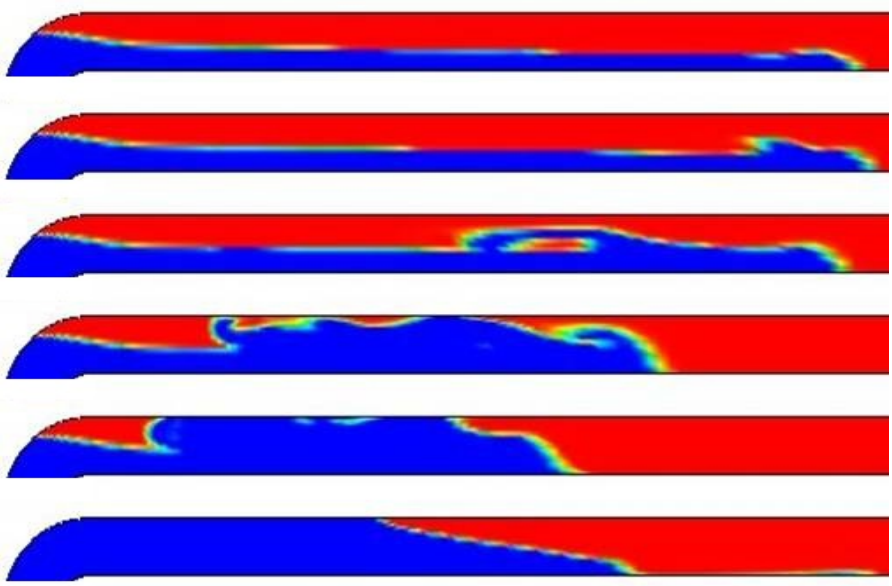

Figure 2.3: Schematic representation of the phase distribution during an CIWH in a horizontal pipe

is a common practice to develop strategies to avoid dangerous events in industrial installations during the early research stage after a new safety-threatening phenomenon is discovered. As a result several models have been developed for the description of CIWH in vertical pipes. This is not the case, however, for horizontal or slightly inclined pipes. The complexity of the flow patterns which can coexist in a horizontal or slightly inclined pipe overcomes that within vertical pipes and thus, limits the number existing models able to capture this phenomenon. Experiments with horizontal test rigs have been conducted by a group of researchers around Griffith [35], [32] and Lee [36] all based in the US, while recent investigations have been carried out in Europe at the PMK-2 facility in Hungary [37], [38], in Germany [39], at UNIBW [40] and at TUHH [11]. The last two facilities have been developed and built as part of the Condensation Induced WAter Hammers (CIWA) research alliance.

Elimination, mitigation or accommodation strategies have been published by Griffith in [33]. These include the adoption of clever designs for the layout of compo-

nents, precise operation procedures or the use of non-condensable gases to decrease the condensation rates, just to enumerate some of them.
The literature offers a set of CIWH mitigation measures, for instance by Chou and Griffith [32]; but no reliable calculation model is yet available. The comprehensive work of Chou and Griffith included CIWH mitigation strategies based on:

- Development of flow stability maps for piping systems, with different orientations, as a function of filling velocities and water subcooling.
- Development of check lists for the designing phase of pipe systems.
- Development of simplified, analytical models.

The initial pressure wave in the case of CIWH, contrary to the water hammer with single-phase column separation, is always negative because it is caused by the condensation of the vapor. This wave later results in an equal and opposite reflected wave. In case of the water hammer initiated by pump or valve operation, the initial pressure wave can be both positive or negative. Another particularity of this kind of water hammer triggered by condensation, compared to the other types, is its stochastic behavior regarding its appearance rate, its location and the maximum amplitude of the pressure spike.
One conservative way to account for the effect of CIWH on the design of components is presented by Joukowski's equation introduced in the previous section, which usually over-predicts the water wave impact intensity [41]. The main drawback of Joukowsky's model is the fact that it highly overestimates the intensity of the water hammer because of the many uncertainties related to the individual variables used. While offering a conservative value for the potential CIWH equation (2.3), it does not consider any influence from the two-phase flow morphology and it is highly sensitive to the liquid slug velocity and its thermo-physical properties all of which have to be estimated based on experience. All these drawbacks make such correlations to be only limitedly applicable in the designing phase of facility equipment. A tool which is capable to correctly model the two-phase flow dynamics including the heat and mass transfer will be more helpful as it can be

used to assess the potential for CIWH of a series of flow scenarios under realistic conditions.
Previous simulations of the DCC or experimental work have both also been performed within the framework of the EU-sponsored NURESIM and NURISP projects [42], Lucas et al. [43], Ruile [44], the Ecora Project [45] and [46]. Different approaches had been used both in single or multi-dimension computational domains. As the DCC acts as the driving force for CIWH, one of the key variables identified, which is the subject of this thesis, is the mechanistic description of the HTC. The description of the new Hybrid SRT based HTC model is introduced in the sub-chapter 4.1. Comprehensive results using this model in either 1D or 3D CFD simulation will be introduced in chapter 6. Additionally, a critical review will be performed in order to ascertain whether such models are suited for the prediction of CIWH in combination with a system code or within a CFD environment.

2.5 Introduction to Dimensionless Numbers

For the sensitivity analysis of the magnitude of CIWH presented in sub-section 6.1.2 the following dimensionless numbers will be used and therefore, need to be introduced in this section. They are the Reynolds number (Re), the Froude number (Fr), the Jakob number (Ja), and the Atwood number (At).
Traditionally dimensionless analysis is an engineering technique developed to analyze complex processes when a direct relationship between significant variables is not well understood or simply unknown. It is a well used approach in fluid dynamics and in the analysis and modeling of heat and mass transfer processes. Dimensionless numbers are used to characterize the most important physical phenomena governing a complex process based on similarities, which include relevant system variables with a clear influence on these phenomena. The relations developed based on such variables, the so-called dimensionless numbers, are expected to define similar behaviors for systems at different scales if the values of such numbers are the same.
First introduced is the dimensionless Reynolds number. It compares by means

of a specially defined ratio of important flow variables the magnitude of the inertial forces to that of the the viscous forces driving a fluid flow. The value of the Reynolds number provides information on whether the viscous forces predominate over the inertial ones. Thanks to its definition, Re can characterize the uniformity of the flow filed, i.e. its turbulence. In the sensitivity study carried out in section 6.1.2 Re is used as an indicator of the degree of turbulence in the horizontally stratified flow in which the CIWH occurs. The mathematical definition of Re for pipe flow is a function of a characteristic velocity, usually the mean value U, a characteristic length scale, usually the hydraulic pipe diameter D_h, and the fluid kinematic viscosity ν in the following form:

$$Re = \frac{U \cdot D_h}{\nu} \tag{2.5}$$

The Froude number, Fr, is also commonly used in hydrodynamics and relates the inertial to the gravitational forces acting on the fluid. This number was identified by Griffith [33] as one key variable to be considered in the CIWH mitigation strategies. The Fr number has been used in subsection 6.1.2 as an indicator of the transition form horizontally stratified to slug flow. The expression defining Fr is shown in equation 2.6 where U represents the mean flow velocity, g is the gravitational acceleration and D_{TS} the inner diameter of the test-section.

$$Fr = \frac{U}{\sqrt{g \cdot D_{TS}}} \tag{2.6}$$

The Jakob number, Ja, is defined by equation 2.7 as the ratio for a given volume of the sensible to the latent heat interchanged during the phase-change between liquid and vapor (condensation or evaporation). In CIWH the Jakobs number is used to quantify the effect of the liquid sub-cooling on the DCC phenomenon.

$$Ja = \frac{\rho_{liq}}{\rho_g} \frac{c_p^{liq} \Delta T}{\Delta h_{liq-g}} \tag{2.7}$$

The dimensionless number proposed by Atwood, At, defined in 2.8 represents, in the case of steam-water flow the ratio between the densities of the phases.

Physically, it tries to characterize the hydrodynamic instabilities in stratified flows. In the sensitivity analysis performed in 6.1.2 this number was used to account for the amount of liquid needed to fill up the collapsed void pocket left empty when the steam has condensed, which acts as the driving force for the liquid water front acceleration towards the location of the collapsing vapor bubble.

$$At = \frac{\rho_{liq} - \rho_g}{\rho_{liq} + \rho_g} \tag{2.8}$$

Chapter 3

Numerical Simulation of Two-Phase Flow

The generic conservation laws and their implementation into *system codes* and *CFD-software* will be presented in this chapter. The emphasis will be on the particularities of the implementation of the conservation equations.

3.1 Introduction to the Numerical Simulation of Two-Phase Flow

The basic equations of two-phase flow dynamics written in different forms are all based on the principles of conservation laws for mass, momentum and energy. Depending on the nature of the analyzed flow, several versions of the conservation equations can be found ranging from simplified models such as the homogeneous equilibrium model, in which both phases are assumed to be in thermodynamic and mechanical equilibrium, to more complex models such as the separated two-fluid model, in which both phases can have different temperatures and velocities.
The description of a given two-phase flow by means of these models can be carried out through the analytical or numerical solution of the conservation equations. Engineering applications limit the applicability of analytical solutions because the

simplifying assumptions that need to be made in such cases would significantly alter the actual physical description of the flow and render solutions that could not reflect the real flow with the needed accuracy. In order to obtain high resolution and acceptable characterization of the results numerical solutions of the two-phase flow conservation equations are required.

The numerical solutions that describe two-phase flows are in general more computationally intensive than those used to simulate single-phase flows due to the complexity added by the presence of two phases that need to be tracked along the flow. It is also fundamental to model their interactions in terms of interchange of mass, momentum and energy across the surface that separates them. Depending on the degree of detail desired, such models can require substantial computer power in order to obtain results that are sufficiently accurate for the application of interest. The introduction of simplifications in the numerical and physical modeling can reduce the computer resources needed but usually at the cost of a significant reduction of accuracy. A description of the most commonly used models for two-phase interface tracking and phase interaction will be presented in chapter 3.4.

The phenomenon of DCC under system conditions that may generate CIWH, the topic of this thesis, is an example of a complex two-phase flow situation in which the physical and numerical quality of the models used have an important impact on the prediction of the onset of CIWH and on the evolution of the generated pressure waves in the system. For this case, two well established numerical simulation methods, both based on the characteristic physical length scales that define the most important physical phenomena, will be used for the simulation and analysis of the DCC and CIWH phenomena in the following chapters. For a system scale analysis in which local effects at scales smaller than the dimensions of the flow channel diameters are averaged, only their influence on the main variables at the system scale is consequently important and coarse numerical spatial discretizations and spatially averaged physical models are therefore used. If the dimensionality of the flow is such that only one main direction is relevant if compared with the other two, the final model treats the system as a one dimensional flow and provides a global system behavior. If the spatially averaged physical models are accurate

enough and the numerical methods solve the volume-averaged conservation equations also in an accurate manner, the solutions of these kinds of analysis may provide results which are acceptably close to the expected physical behavior for the objectives of the analysis of interest.

If highly detailed high resolution results are required, a Reynolds Averaged Navier-Stokes (RANS) based *CFD* simulation should be employed. This approach focuses on smaller spatial scales with physical models that attempt to simulate local aspects of two-phase flow interactions and are averaged at a much smaller scale than the geometrical dimensions of the system being analyzed. Numerical discretizations are also focusing on these small scales and the final result is a much more accurate local description of the two-phase flow dynamics whose effects can then be seen on variables defined at the larger scales of the system. i.e. average temperatures, vapor fractions, heat transfer with the solids, etc. These high resolution approaches are usually three dimensional in their nature, since they try to simulate the evolution of the two-phase flow structure as closely as possible to reality, and also significantly more computationally intensive.

In principle, if both descriptions are well defined and consistent with each other, the results of the more local one, should be of a comparable quality for variables defined at the scales of the less spatially refined approach. Each of these two approaches, based on a technique that solves the conservation equations through a finite volume discretization of the computational domain within an Eulerian framework, will be explained in more detail in the next chapters.

3.2 Introduction to relevant Conservation Equations

In this chapter, the generic conservation equations used for the description of a two-phase flow in typical Eulerian finite-volume based computer codes are presented. This class of codes employs either fixed, time independent computational grids for the flow development, or continuously adapts the mesh. In the following computer simulation, a fixed grid was used, for both the system code and CFD simulations.

One important assumption made in order to describe a flow according to the following conservation laws is the continuum approach of the considered fluid. Under this assumption the molecular structure of the fluid is ignored, due to its very small length scales. Keeping track of these length scales would require both large computational power and computational time.

The analytical solution of the governing equations is impossible in case of unsteady, turbulent flows in complex industrial facilities. Due to this reason, a numerical solution of the conservation equations is required.

The mathematical description of the governing conservation equations of the *transient two-fluid model*, in a finite-volume approach takes the following form for the phase k (liquid or gas):

1. Phase mass conservation

$$\frac{\partial \alpha_k \rho_k}{\partial t} + \nabla \cdot \left(\alpha_k \rho_k \overrightarrow{U_k} \right) = \Gamma_k \tag{3.1}$$

   with the source / sink term Γ_k accounting for phase change.

2. Phase momentum conservation

$$\begin{aligned} \frac{\partial \alpha_k \rho_k \overrightarrow{U_k}}{\partial t} + \nabla \cdot \left(\alpha_k \rho_k \overrightarrow{U_k} \overrightarrow{U_k} \right) = \\ -\alpha_k \nabla p + \nabla \cdot \left[\alpha_k \left(\tau_k + \tau_k^t \right) \right] + \alpha_k \rho_k \overrightarrow{g} + S_M \end{aligned} \tag{3.2}$$

with the interfacial momentum transfer term $S_M = \Gamma_k \overrightarrow{U_{ki}} + M_k$.

3. Phase energy conservation

$$\begin{aligned} \frac{\partial \alpha_k \rho_k h_k^{tot}}{\partial t} + \nabla \cdot \left(\alpha_k \rho_k h_k^{tot} \overrightarrow{U_k} \right) = \\ \alpha_k \frac{\partial p}{\partial t} + \alpha_k \rho_k \overrightarrow{g} \cdot \overrightarrow{U_k} - \nabla \cdot \left[\alpha_k \left(\overrightarrow{q_k} + \overrightarrow{q_k^t} \right) \right] + S_E \end{aligned} \tag{3.3}$$

with the energy transfer term $S_E = \Gamma_k h_k^{tot} + q''_{ki} a_i + q'''_{wk}$ where h_k^{tot} represents the sum of the phase-averaged enthalpy for phase k and its kinetic energy $\frac{U_k^2}{2}$.

The above compact conservation equations represent a system of nonlinear partial differential equations. It is a convention that source terms have a positive sign while sink terms have a negative sign. One has to keep in mind that there is a big difference between the general form of a conservation equation at its implementation in a computer code, which requires additional processing operations.
The variables used for the description of the conservation equations, excepting the source and sink terms due to phase change, are: α_k represents the volumetric phase fraction, ρ_k the density, $\overrightarrow{U_k}$ is the velocity vector, p is the averaged pressure field, τ_k and τ_k^t the molecular stress tensor respectively the Reynolds (turbulent) stress tensor, $\overrightarrow{g}$ represents the gravitational acceleration vector, M_k represents the interfacial momentum exchange, $\overrightarrow{q_k}$ and $\overrightarrow{q_k^t}$ the molecular respectively the turbulent heat fluxes vectors, $q''_{ki} a_i$ and q'''_{wk} are the interfacial heat transfer and the heat transfer from the wall to the fluid, where a_i is the IAD.

It is an often used convention in fluid dynamics that by the *void fraction* the instantaneous volume-averaged void fraction is meant. The expressions for the void fraction α was introduced in equation (2.1) while the interfacial area density a_i is computed according to:

$$a_i = \frac{A_{interface}}{V}. \tag{3.4}$$

The additional variables introduced in these two equations are: V which represents the total volume of the considered geometric entity and A for the interfacial area.

Additional expressions also called closure laws are required for certain variables in the conservation equations. The volumetric interface mass transfer source or sink term Γ_k is computed by performing a heat balance at the two-phase interface:

$$\Gamma_k = \frac{HTC_k \left(T_g - T_{liq}\right)}{h_g - h_{liq}} a_i \tag{3.5}$$

where T is the temperature and h is the enthalpy. In the case of the momentum conservation equation, the relative phase velocity to the interface velocity is calculated as follows:

$$\overrightarrow{U_{ki}} = \overrightarrow{U_k} - \overrightarrow{U_i} \tag{3.6}$$

Special models have to be implemented to calculate IAD or HTC in system codes as well as in CFD tools. Recently special effort has been put into setting up a conservation equation for tracing the IAD in computer codes, both system codes and CFD codes. The initial model was proposed by Kocamustafaogullari and Ishii [47]. Special models have to be considered for the calculation of the interfacial area source and sink terms, S_a. Still no universal model applicable for all types of flow patterns is available. The source term S_a on the Right Hand Side (RHS) of equation 3.7 accounts for different influences that can increase the IAD such as flow pattern changes or interface shearing, resulting in interface break-up or IAD decreasing due to interface coalescence.

$$\frac{\partial a_i}{\partial t} + \nabla \cdot \left(a_i \overrightarrow{U_k}\right) = S_a \tag{3.7}$$

The conservation laws are solved based on a computational grid consisting of finite-volumes. A staggered grid approach can be used in finite-volume system codes in order to avoid the so called 'odd-even decoupling' between the pressure and the velocity with the price of storing variables in different locations of the computational grid. Variables such as the phase fraction, temperature and pressure are stored in the cell center, whereas the velocity is stored at the cell interfaces. If a collocated grid is used, with the advantage in requiring a lower storage memory, special care is required to overcome the occurrence of oscillations in the pressure-velocity

coupling. One solution to this problem is the Rhie and Chow interpolation [48]. Since the development of this method, collocated grids have been widely adopted, especially in CFD codes. The 3D character of CFD computational domains and the relatively high number of computational cells, make a collocated grid approach very attractive, as simulations are already computationally expensive.
The employed system code Analysis of Thermal-Hydraulics and LEaks (ATHLET) uses the staggered grid approach while the used CFD codes, both CFX and OpenFOAM employ collocated grids.

3.3 Introduction to System Codes

Even with the fast increase of computational power in recent years, one dimensional system codes are still extensively used for the simulation of two-phase flow in large thermal-hydraulic systems such as NPPs, chemical engineering facilities, thermal power plants, etc. Particularly the simulation of long lasting and physically complex transients is especially suited for these types of codes when the relevant results are those reflecting the overall system behavior. System codes can provide average values for important system variables with relatively short computational times. Although traditionally one-dimensional in nature, system codes have recently acquired multi-dimensional capabilities in order to be able to successfully deal with a series of applications in the nuclear safety fields related to the LOCA. Complex asymmetric two-phase flow patterns commonly arise in large volume components during the progression of a LOCA. The desire for higher accuracy in the results strongly drives the development of multidimensional system codes with better physical models.
Modern one-dimensional system codes solve the flow conservation laws separately for the steam and liquid phase by making use of the two-fluid six-equation approach (although additional fields are also possible). The two-fluid flow model used by these codes still requires some empirically determined closure laws, due to the description of the flow based on coarse computational cells in which locally occurring physical phenomena must be averaged to the scales of the computational volumes.

The conservation laws of the two-fluid model haven been previously introduced in equations (3.1) to (3.3) of chapter 3.2.
The system code used in this thesis is the German thermal-hydraulic system code ATHLET. It is released by the Gesellschaft für Anlagen- und Reaktorsicherheit (GRS) and is under continuous development and improvement. The code was created for the analysis of anticipated and abnormal nuclear power plant transients, small, intermediate and large loss of coolant accidents [49].
The system code describes the two-phase flow on a finite volume decomposition of the simulation domain. It offers several two-phase flow models available for the user and considering the low computational time in the case of one-dimensional simulations, the two-fluid model was applied for the analysis carried out in this thesis instead of the five conservation equations plus a drift flux model to calculate the relative velocity between the phases also available. ATHLET already includes an IAD transport equation, which follows the form presented in equation (3.7), [50].
A schematic representation of a typical staggered grid as employed in ATHLET is presented in figure 3.1. The variables p, T_L, T_V and X_M stored at the cell center represent the pressure, the temperature of the liquid phase, the temperature of the gaseous phase, and the mass quality. On the cell interfaces, the variables $w_V A$ and $w_L A$ are stored, which represent the product between the individual phase velocity and the total area of the junction.
The numerical methods implemented into the system code ATHLET produce a first order accurate, fully implicit solution of the non-linear system of Partial Differential Equation (PDE). The linearization of the implicit system is done using the Jacobian matrix of the PDE system. By using a fully implicit time discretization scheme, ATHLET overcomes the limitations of the small time steps required by explicit schemes in order to avoid the Courant-Friedrich-Levy Number (CFL) number becoming larger than one. Spatial discretization follows a first-order donor cell approach, which introduces the drawback of numerical diffusion in the solution of the equations and tends to smear sharp interfaces of flow variables as they are transported along the computational volumes. ATHLET can also make use

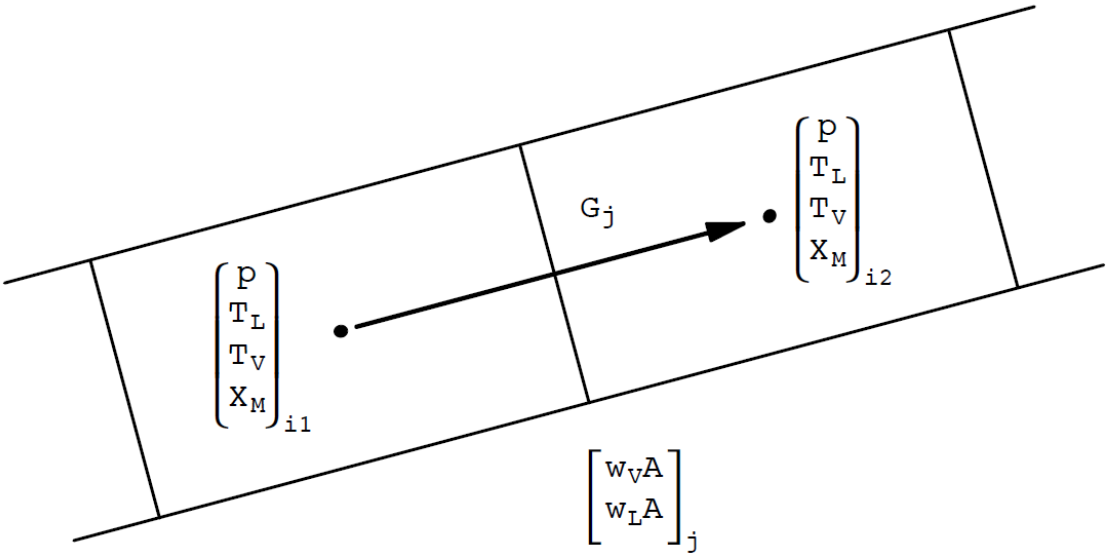

Figure 3.1: Employed staggered grid used by the System Code ATHLET [3]

of special numerical schemes especially implemented for problems involving solute tracking. DCC relevant variables such as void fraction, however, are not dealt with in the same manner. Small cell sizes can help in reducing the effect of numerical diffusion at the price of smaller time step sizes. This is clearly a disadvantage in the case of explicit time discretization techniques, but it is not a problem in ATHLET when the fully implicit solution method is applied, i.e. small cells can be used with large time step sizes without compromising the stability and the accuracy of the results. In all the calculations presented in this thesis, this is the manner in which the simulations have been carried out.

The implementation of the new hybrid HTC model in ATHLET has preserved the main code structure and numerical solution methods. The key term that has been modified in the linearized system of equations is the closure law for the energy balance at the interface of the two-phase flow. The new HTC resulting from merging of two individual SRT based models accounting for different effects of the turbulence on the condensation rate according to the dominant eddy length scales are dynamically combined at the computational cell level to yield an appropriate value for the HTC. This is done based on the flow conditions and its structure predicted

in each cell by the relevant ATHLET flow regime models and calculated values of the system variables. The detailed description of this procedure is presented in chapter 4.

3.4 Introduction to CFD Codes

One of the fundamental problem to address in the modeling of CIWH with CFD is the accurate tracking of the well defined phase interface at which DCC takes place. Several approaches are currently used by different authors for this purpose, e.g. the Level Set Method (LSM), the shallow water equations, and the VOF method. Based on previous experience, the latter method has been selected for the CFD simulations performed in this thesis as discussed later in chapter 6. A presentation of the VOF method is also introduced in chapter 3.4.1.
The main advantage of the VOF model is its ability to conserve mass in contrast to the LSM offering a comparable or sometimes better accuracy in the interface tracking procedure, which makes the VOF method one of most versatile and popular interface tracking methods implemented in current CFD codes.
Comparing the VOF model to the shallow water equations, highlights the fact that the latter represents a model that describes the horizontal structure of the fluid movement based on two simplifying assumptions, namely, the pressure is linearly distributed with depth and the vertical acceleration within the flow is neglected. This latter assumption can be eliminated by some formulations of the shallow water equations by using the Boussinesq equations. The shallow water model is appropriate for inviscid, incompressible fluid flows in which the horizontal dimensions of the surface waves exceed the fluid depth.

3.4.1 The Volume of Fluid Model

The VOF, later used in all performed CFD simulations, is an advection scheme, representing an Eulerian formulation for problems of hydrodynamics involving free boundaries. First introduced by Hirt and Nichols [51], it became a popular method applied in CFD simulations for flows in which the shear stress plays an important

role and both phases are separated by a large, deformable interface, e.g. a two phase flow with a free surface, a well-defined interface, allowing the free surface to undergo large deformations. The free surface is defined as a boundary, where discontinuities exist [51]. A step function is used for the phase identification in this single-field representation of the two-phase flow. The step function is defined according to the equation (3.8).
The original form of the VOF model for a computational volume as presented by Hirt and Nichols, [51], is set up as the fractional volume of the cell occupied by the liquid. In the analyzed two-phase flow between water and steam, the step function takes the value 1 in the liquid phase and 0 in the gaseous phase.

$$\gamma = \frac{\rho - \rho_1}{\rho_1 - \rho_2} \tag{3.8}$$

According to this model, cells with an intermediate value of γ contain both phases and if in addition at least one neighboring cell contains one of the extreme values, the interface is located in the cell in which both phases coexist. A schematic representation of an idealized phase distribution is presented in figure 3.2. The cell volume fraction which is occupied by the liquid is stored in the cell center and a generic interface reconstruction is imposed in this schematic draw.

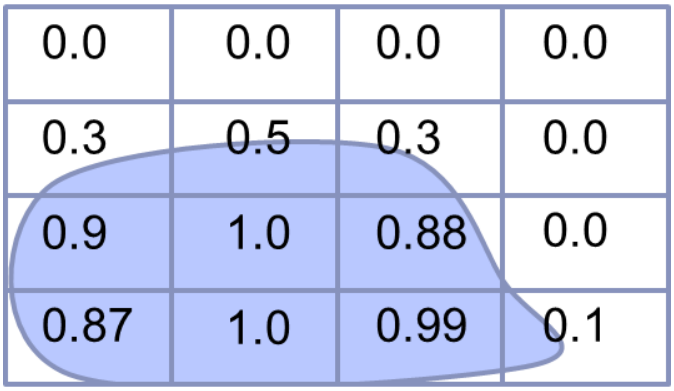

Figure 3.2: Schematic representation of the theoretical phase distribution computed with VOF, [4]

Within the VOF model, a *mixture fluid* is created, where the thermo-physical properties of the new fluid are obtained by linear interpolation using the volume fraction γ as shown in the equation (3.9). Any particular thermo-physical property, ζ_{mix} can be averaged, using the phase indicator in the following way:

$$\zeta_{mix} = \gamma \cdot \zeta_1 + (1 - \gamma) \cdot \zeta_2 \tag{3.9}$$

The transport equation for the phase identifier in the case of the standard VOF model is presented in equation (3.10).

$$\frac{\partial \rho_1 \gamma}{\partial t} + \nabla \cdot (\rho_1 \gamma \overrightarrow{U}) = S_\gamma \tag{3.10}$$

The source and sink term, S_γ, on the RHS of equation (3.10) is accounting for phase change and it is computed as $S_\gamma = \Gamma_k$. For phase change due to DCC it takes the form expressed in equation (3.5). For the computation of the IAD, which per computational cell represents the ratio between the interfacial area within the cell and the cell's volume, the following equation is employed:

$$a_i = |\nabla \gamma| \tag{3.11}$$

The momentum transport equation corresponds to the typical RANS approach, with the additional consideration of a continuous surface tension. A particularity of the VOF model is that it only accounts for a single velocity field which is shared by both phases: equation (3.12). The fact that within this model both phases share a single velocity field makes it inappropriate for the description of polydispersed flows with a large density ratio between the two phases. In the particular case of polydispersed flows, the phase relative velocity becomes important and thus affects the terms representing interfacial friction, drag forces etc.

$$\frac{\partial \rho \overrightarrow{U}}{\partial t} + \nabla \cdot \left(\rho \overrightarrow{U} \overrightarrow{U} \right) = -\nabla p + \nabla \cdot \mu \nabla \overrightarrow{U} + \rho \overrightarrow{g} + f_i \tag{3.12}$$

The last term on the RHS, f_i, represents the momentum source term due to surface tension. It is only active at the interface, i.e. in those cells with $\gamma \in (0,1)$. It depends on the curvature of the surface κ, on the surface tension σ and on the normal vector to the interface $\overrightarrow{n}$. The normal vector to the interface is presented in equation (3.13) and the surface curvature is expressed in equation (3.14).

$$\overrightarrow{n} = \frac{\nabla\gamma}{|\nabla\gamma|} \tag{3.13}$$

$$\kappa = -\nabla \cdot \left(\frac{\nabla\gamma}{|\nabla\gamma|}\right) \tag{3.14}$$

The conservation of energy of an incompressible two-phase flow is presented in equation (3.15).

$$\frac{\partial \rho h^{tot}}{\partial t} + \nabla \cdot (\rho h^{tot} \overrightarrow{U}) = \nabla \cdot (k_{eff} \nabla T) + S_E \tag{3.15}$$

The last term in the equation (3.15), S_E accounts for the heat transfer at the phase interface.

Special attention has been given to the interface in order to avoid the 'smearing' of the step function, in terms of the employed numerics. To conclude: a sharp interface delivers more accurate results, while a more smeared interface enhances the robustness of the simulation as the gradients become less sharp. In order to avoid numerical difficulty where calculating the interface unit normal vector of a very sharp surface, a smoothing method must be implied.
As this model requires the storage of only one additional variable per computational cell and not necessarily requiring a logical interface reconstruction algorithm, makes this method attractive for CFD simulations of large computational domains within a reasonable amount of computational time. In other words it offers an economic way to track free boundaries in multi-dimensional meshes [51].

Particularities of the implementation of the VOF model in OpenFOAM 1.7.1

The general VOF model for an incompressible fluid is already implemented into OpenFOAM version 1.7.1 with some particularities. The relevant particularities and the additional development work carried out for the custom tailored solver will be presented in this chapter. A more detailed description of the standard implemented VOF model as available in OpenFOAM can be found in [52].
In the case of the phase indicator transport equation, special attention has to be given to avoid the smearing of the interface through several computational cells. In OpenFOAM this is handled not by employing a compressive differencing scheme but rather by imposing an additional compression velocity ($\overrightarrow{U}_c$) at the phase interface. The solution procedure as implemented in OpenFOAM developed by Weller is presented in [52]. Considering these particularities, the original VOF conservation equation (3.10) is modified into the form of equation (3.16).

$$\frac{\partial \alpha}{\partial t} + \nabla \cdot (\alpha \overrightarrow{U}) + \nabla \cdot (\alpha(1-\alpha)\overrightarrow{U}_c) = \frac{\Gamma}{\rho_1} \tag{3.16}$$

The additional artificial term is used only in the cells containing intermediate values of α due to the multiplication term $\alpha\,(1-\alpha)$. In the case of the VOF solver implemented in OpenFOAM, the compression velocity $\overrightarrow{U}_c$ is calculated based on an user adjustable amplification factor, the unit normal vector at the interface and the maximum velocity magnitude [52]. The user defined factor is used to artificially enhance the interface sharpness. At the same time the user has to find a compromise between sharpness of the interface and numerically smooth gradients for robustness of the simulation, when the interface curvature is calculated.
In the OpenFOAM built-in VOF solver, the index 1 refers to the liquid or denser phase whereas the index 2 refers to the gaseous, less denser phase. The divergence free condition available in the standard VOF based solver in OpenFOAM does no longer apply for phase change and has to be adapted to:

$$\nabla \cdot \overrightarrow{U} = \Gamma \left(\frac{1}{\rho_2} - \frac{1}{\rho_1} \right) \tag{3.17}$$

The momentum equation is solved by means of a pressure-velocity coupling, Pressure Implicit with Splitting of Operators (PISO). The PISO algorithm is an efficient procedure to solve the Navier-Stokes equations for unsteady problems. A detailed description of the PISO method can be found in [53].
In a nutshell the PISO algorithm for one time step consists of following stages:

- Setting up of the Boundary Condition (BC)
- Solving the momentum equation to compute the intermediate velocity field and the mass fluxes at the cell faces
- Solving the pressure equation
- Updating and correcting the mass fluxes
- Solving and correcting the velocities based on the pressure field to fulfill the mass conservation
- Updating the BC

Due to some numerical problems, resulting in the unboundedness of the solving variables the energy conservation equations have been collapsed into just the liquid side energy conservation equation. This was possible as the DCC of steam into subcooled liquid is assumed to occur at the saturated two-phase interface.

The accompanied turbulence models, used with the VOF model, will be introduced in chapter 3.4.2.

3.4.2 Turbulence Modeling in CFD

Turbulence is a flow regime in which the motion is intrinsically unsteady even with constant boundary conditions, where the velocity, similar to other flow properties, varies in a chaotic and arbitrary way. Turbulence is a phenomenon of great complexity and has puzzled theoreticians for over a hundred years [5]. For a more convenient description of the flow, a decomposition of the flow velocity in

a mean velocity and a three-dimensional fluctuating term is performed as graphically represented in figure 3.3. The fluctuating term enhances the mixture of any transported variable; such as mass, momentum, energy etc.
Even if large eddy simulations are increasingly used in CFD simulations, still RANS turbulence models are widely spread for industrial applications. Large Eddy Simulation (LES) are turbulence models where only small eddies are modeled while the time-dependent conservation equations are solved for the mean flow and the large eddies. This comes with an increase of computational power required, but additional information on the pulsating quantities becomes available. If RANS models are employed, only the statistically averaged turbulent motion is resolved while the turbulent fluctuations are only modeled.

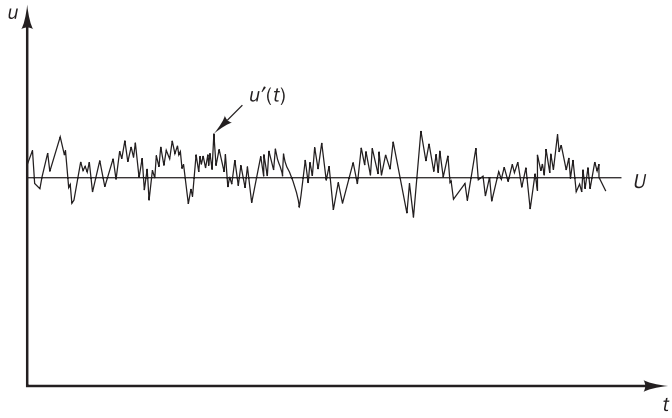

Figure 3.3: Measured velocity in a turbulent flow [5]

This is done by considering the decomposition of each velocity component u into the sum between its time-averaged mean value U, the first term on the RHS, and the fluctuating component, the second term on the RHS of equation (3.18).

$$u = \overline{U} + u' \tag{3.18}$$

Due to the impossibility of accounting for the smallest existing eddy length scales of only a few μm in the computational grids and the smallest eddy time scales of a few ms in engineering applications, a time-averaging process has to be performed. The time averaging is performed exemplarily for the velocity in the equation (3.19).

If the averaging is performed over a time interval, Δt, at least larger than the time scale of the largest eddy, the averaging of the pulsating velocity will result in zero.

$$U = \frac{1}{\Delta t} \int_0^{\Delta t} u(t) dt \tag{3.19}$$

The decomposition of the flow into a part governed by the average property and a pulsating one will introduce additional terms in the conservation equations that account for the influence of the fluctuating terms.
The high resolution of computational grids employed in CFD simulations offers the possibility to use transport equations for the turbulent quantities.
One of the imposed requirements on turbulent models is that these should be able to cover a wide applicability range. Typical turbulence models in order of their complexity are:

- Algebraic models also called zero equation models as they consist of algebraic equations rather than of PDEs. These models consist of algebraic equations for the turbulent viscosity and the turbulent Prandtl number.
- One-equation models consist of a differential equation for the Turbulent Kinetic Energy (TKE).
- Two-equation models consist of a set of two PDE, one for the TKE and one for the dissipation rate, in the case of the $k - \epsilon$ model or the frequency in case of the $k - \omega$ model.
- Reynolds stress models include either algebraic equations or PDE for each of the Reynolds stress tensor components.

A commonly used variable for most RANS based turbulence models is the TKE, generally denoted as k. The TKE is defined as:

$$k = \frac{1}{2}(\overline{u_x'^2} + \overline{u_y'^2} + \overline{u_z'^2}) \tag{3.20}$$

The individual contributions on the RHS of equation (3.20) are the individual components of the fluctuating velocity vector u' in the Cartesian coordinate system.

Another variable used for the characterization of turbulence is the turbulence intensity I. It relates the root mean square of the turbulent velocity fluctuations (u') to the mean velocity of the flow:

$$I = \frac{u\prime}{U} = \frac{\sqrt{\frac{1}{3}({u'_x}^2 + {u'_y}^2 + {u'_z}^2)}}{\sqrt{\overline{U_x}^2 + \overline{U_y}^2 + \overline{U_z}^2}} \tag{3.21}$$

Only the two equations $k-\omega$SST turbulence model was used in the CFD simulations within this work and will thus be covered in detail. This model is employed as it is recommended for two-phase flow without any special tuning. The description of the $k-\omega$SST turbulence model also includes the $k-\epsilon$ model implicitly.

The $k-\epsilon$ Turbulence model

The standard $k-\epsilon$ model is probably the most widespread and popular two-equation turbulence model in today's CFD simulations for engineering applications and was initially developed by Launder and Spalding, [54]. It is best performing at high Reynolds numbers but yields poor results in near-wall regions.
The $k-\epsilon$ model introduces two additional PDE in the system of equations, one for the turbulent kinetic energy k and one for the turbulence dissipation rate ϵ. The effective viscosity that operates with the velocity gradients is defined as

$$\mu_{eff} = \mu + \mu_t \tag{3.22}$$

In equation (3.22), μ_t is the turbulence viscosity. The $k-\epsilon$ assumes the following relation between the turbulence viscosity, k and ϵ:

$$\mu_t = C_\mu \rho \frac{k^2}{\epsilon} \tag{3.23}$$

where $C_\mu = 0.09$ is a constant. The two transport equations for k and ϵ are

$$\frac{\partial \rho k}{\partial t} + \nabla(\rho U k) = \nabla[(\mu + \frac{\mu_t}{\sigma_k})\nabla k] + P_k + P_{kb} - \rho\epsilon \tag{3.24}$$

$$\frac{\partial \rho\epsilon}{\partial t} + \nabla(\rho U\epsilon) = \nabla[(\mu + \frac{\mu_t}{\sigma_\epsilon})\nabla\epsilon] + \frac{\epsilon}{k}(C_{\epsilon 1}(P_k + P_{\epsilon b}) - C_\epsilon \rho\epsilon) \tag{3.25}$$

Where $C_{\epsilon 1}$, $C_{\epsilon 1}$, σ_k and σ_ϵ are constants. P_k is the turbulent generation and is determined by

$$P_k = \mu_t \nabla U \cdot (\nabla U + \nabla U^T) - \frac{2}{3}\nabla \cdot U(3\mu_t \nabla \cdot U + \rho k) \tag{3.26}$$

P_{kb} and $P_{\epsilon b}$ account for the influence of buoyancy forces. If the full buoyancy model is used, P_{kb} takes the following form

$$P_{kb} = -\frac{\mu_t}{\rho\sigma_\rho} g \cdot \nabla\rho \tag{3.27}$$

$P_{\epsilon b}$ is taken proportionally to P_{kb} and must be positive and C_3 is a constant

$$P_{\epsilon b} = C_3 \cdot max(0, P_{kb}) \tag{3.28}$$

The $k-\omega$ Turbulence Model

In the $k-\omega$ turbulence model developed by Wilcox [55] it is assumed that the eddy viscosity is linked to the TKE and the turbulence frequency ω as expressed in equation (3.29).

$$\mu_t = \rho\frac{k}{\omega} \tag{3.29}$$

The two transport equations for k and ω are presented in the equations (3.30) and (3.31).

$$\frac{\partial \rho k}{\partial t} + \nabla(\rho U k) = \nabla[(\mu + \frac{\mu_t}{\sigma_k})\nabla k] + P_k + P_{kb} - \beta'\rho k\omega \tag{3.30}$$

$$\frac{\partial \rho \omega}{\partial t} + \nabla(\rho U \omega) = \nabla[(\mu + \frac{\mu_t}{\sigma_\omega})\nabla\omega] + \alpha\frac{\omega}{k}P_k + P_{\omega b} - \beta\rho k\omega \tag{3.31}$$

The newly introduced variables β', β, α, σ_k and σ_ω are model built-in constants. The source term $P_{\omega b}$, on the RHS of equations (3.32) is calculated as shown in equation (3.32).

$$P_{\omega b} = \frac{\omega}{k}((\alpha + 1)C_3 \cdot max(0, P_{kb}) - P_{kb}) \tag{3.32}$$

The $k-\omega$ model, [55], was developed for low-Reynolds-number applications and delivers good performances especially in the proximity of wall regions thus complementing the flaw in the $k-\epsilon$ model. Similar to the $k-\epsilon$ turbulence model, this model requires two additional conservation equations to be solved; one for the TKE and one for the turbulence frequency ω.

The Shear Stress Transport (SST) Model

The SST model combines the advantages of both the $k-\epsilon$ and the $k-\omega$ model by using the recommended model in the region where it is best performing. The switching between the two models is done based on a transition function. Accordingly the SST model combines the best features of the two models and offers higher reliability and accuracy while maintaining stability and reasonable computing time.

3.5 Introduction to the Surface Renewal Theory

This section contains state-of-the-art information about the SRT as a mechanistic description of heat transfer. The theoretical background will be introduced here, while the implementation in computer codes will be presented in chapter 4.
The original concept of SRT was introduced by Higbie, [56] initially describing the transport of gases into liquids. Phenomenologically it is based on small liquid volumes which are considered to reach the two-phase interface where they interact with the gaseous phase before being removed and transported back into the liquid bulk by turbulent eddies. A continuous scalar exchange is directly controlled by the exposure time of the small liquid volumes at the interface. The exposure time of these 'micro-volumes' also linked with the Surface Renewal Period (SRP) is the ratio between a length and a velocity scale and has to be determined within the model.
Mass transfer occurring at the interface is governed by molecular diffusion during the contact time between the small liquid volumes and the interface. Initially, the contact time was assumed to be uniform for all scales of turbulent eddies.

Once this model became widely accepted and used, new concepts were added to the original theory of SRT in order to improve its accuracy and predictive capability. For example, the modification proposed by Danckwerts [57] considered two new parameters, the variable and random age residence times at the interface. The model developed by Torr and Marchello [58] which added a finite dimension to the region of the surface renewal.

In an analogy with convective mass and heat transfer one can say that the SRT accounts for convective transport of small liquid volumes carrying mass and energy by turbulent eddies which can break through the laminar sub-layer of the liquid in contact with the interface and replace the already saturated small liquid volumes at the interface with fresh, subcooled liquid volumes from the fluid bulk. Through this mechanism heat and mass transfer are controlled by the *contact time* at the surface represented by the interface. Physically the *contact time* reflects the time spent by the eddies interacting on the two-phase interface. It therefore, controls the amount of energy and mass that can be transferred across the surface. The *contact time* SRT is computed as the ratio between the characteristic eddy length scale L_t and the eddy velocity scale V_t as presented in equation 3.33.

$$SRT = \frac{L_t}{V_t} \tag{3.33}$$

In order to include heat transfer in the SRT, an energy balance has to be performed at the interface as indicated by Banerjee [59]. The HTC controlling the heat flux at the gas-liquid interface is given in its general form as:

$$HTC_{liq} = \frac{C}{\sqrt{\pi}} \lambda Pr_{liq}^{1/2} \left(L_t\right)^{n-1} \left(\frac{V_t}{\nu_{liq}}\right)^n \tag{3.34}$$

The variable C is a model-specific constant, λ is thermal conductivity of the liquid, Pr the Prandtl number of the liquid, L_t and V_t are the characteristic eddy length and velocity scales, ν the liquid kinetic viscosity and n a model dependent constant. The assumption that the liquid offers the only resistance to the heat transfer influenced by its thermo-physical properties holds as long as the gaseous phase remains at saturation, which is applicable in the analyzed case of DCC.

Interfacial heat transfer models based on this approach directly correlate the calculation of the HTC to the turbulence character of the flow i.e. to the TKE, the turbulent eddy dissipation rate ϵ and the thermo-physical properties of the liquid. The strong link between turbulence and the HTC transforms SRT based models into mechanistic approaches of the DCC phenomenon. Their theoretical ability of offering a continuous smooth transition of the HTC for different flow regimes makes the SRT based models attractive to be applied for the calculation of the HTC for all transient horizontal flow patterns.
The difficulty in choosing the adequate SRT based model lies in the selection of the proper length and velocity scales of these turbulent eddies driving the interfacial heat and mass transfers, which influences the SRP. Some authors have for example proposed objectively calculated fractions of channel depths, wavelengths of surface oscillations or mean flow dimensions as characteristic eddy sizes.
The applicability of the theory to pipe flow has been demonstrated by Duffey and Hughes in [60]. All individual, stand-alone SRT based models have the following limitation in their present form: these models mainly offer the possibility of interpreting measurement data with some parameter tuning effort, but have difficulties when used as predicting tools [61]. Under these circumstances the quality of eventual simulation results relies on the knowledge and experience of the user and may lead to high uncertainties in the final results. Available individual, stand-alone SRT based models are thus difficult to be used for safety assessment of the operation of industrial systems such as nuclear power plants or chemical installations. In such applications reliable predictive capabilities of the employed modeling approach are fundamental in producing so-called conservative predictions (*worst case scenario*) of the safety of a system's behavior.
One of the two individual models used in chapter 4 for the development of the new hybrid HTC model was developed by Hughes and Duffey, i.e. the Micro Scale Eddies (MiSE) model [62], while the other was developed by Shen et al. [63], i.e. the Macro Scale Eddies (MaSE) model. The model accounting for mirco eddies in the calculation of the HTC will be presented in subsection 3.5.1, the SRT based HTC model considering macroscopic eddies will be introduced in subsection 3.5.2.

3.5.1 Surface Renewal Theory accounting for Microscopic Eddies for Scalar Exchange

The model developed by Hughes and Duffey [62] considers that the smallest scales in a turbulent flow also known as Kolmogorov micro-scales are mainly responsible for the transfer of energy. Considering the small length scale and correspondingly high velocity scale, this model delivers a short SRP, which results in more energy being transferred between the interface and the liquid bulk per unit time, i.e. a higher energy transfer rate. Hughes and Duffey's model is based on the hypothesis set by Kolmogorov for isotropic turbulence, which holds for very small eddies [64]. Such eddies are formed at the interface mainly by shear stresses or by the influence of a nearby wall [62].
The calculation of the heat flux at the gaseous-liquid interface is done as proposed by Banerjee, [59] based on equation (3.34). The general form of the interfacial heat flux has then the form:

$$q^i_{g-liq} = 2\rho_{liquid} c_{p,liq} \left(\frac{\alpha_{liq}}{\pi}\right)^{1/2} \left(\frac{1}{t^{MiSE}_{rp}}\right)^{1/2} (T_{sat} - T_{liq}) \tag{3.35}$$

The variable α_{liq} in (3.35) represents the thermal diffusivity of the liquid phase while $1/t_{rp}$ stands for the SRP which has to be calculated based on the Kolmogorov length and velocity eddy scales according to (3.36) and respectively (3.37).

$$L^{MiSE}_t = \left(\frac{\nu^3_{liq}}{\epsilon}\right)^{1/4} \tag{3.36}$$

$$V^{MiSE}_t = (\nu_{liq}\epsilon)^{1/4} \tag{3.37}$$

Rearranging the terms in equation (3.35) and replacing t_{rp} with the ratio between the eddy length and its velocity scale, leads to the final form of the HTC shown in equation (3.38).

$$HTC^{MiSE}_{liq} = C\rho_{liq} c_{p,liq} \left(\frac{\alpha_{liq}}{\pi}\right)^{1/2} \left(\frac{\epsilon}{\nu_{liq}}\right)^{1/4} \tag{3.38}$$

3.5.2 Surface Renewal Theory accounting for Macroscopic Eddies for Scalar Exchange

The Shen et al. model [63] considers that larger eddies are mainly responsible for the transport energy across the liquid-gas interface.
Even if the validity of computing the large scale eddies based on the $k-\epsilon$ model and using the dissipation rate might by questioned, this is applicable at low Reynolds numbers as the rate at which large eddies remove energy from the mean flow is approximated to the rate of transfer of energy across the energy spectrum to smaller, dissipating eddies [5].
The mathematical form of the MaSE model is based on the general formulation proposed by Hughes and Duffey described in the previous section, differing basically in the definition of the turbulent length and velocity scales L_t and V_t. Shen et al's model uses the length scale of the standard k-ϵ model and a slightly modified Kolmogorov velocity scale as shown in equations (3.39) and (3.40).

$$L_t^{MaSE} = C_\mu \frac{k^{3/2}}{\epsilon} \tag{3.39}$$

$$V_t^{MaSE} = C_\mu^{1/2} \left(\nu_l \epsilon\right)^{1/4} \tag{3.40}$$

$$HTC_{liq}^{MaSE} = \frac{C}{\sqrt{\pi}} \lambda_{liq} Pr_{liq}^{1/2} (L_t)^{-1/3} \left(\frac{V_t}{\nu_{liq}}\right)^{2/3} \tag{3.41}$$

The larger length scale yields larger SRP values which result in lower values for the HTC than if micro-scale eddies are considered for the calculation of the SRP. The final version of the HTC based on macro-scale eddies is taken from [46], and presented in equation (3.41).

Chapter 4

Present Contribution to the Calculation of CIWH

The newly developed hybrid SRT based HTC model, together with its implementation into the system code ATHLET and into the CFD codes, both ANSYS CFX and OpenFOAM, will be presented in this chapter.
The problem of realistically describing the DCC and the implementation of such a model into a computer code requires the mechanistic modeling of the interfacial heat and mass transfer. The main difference between the simulation of such a phenomenon with either system codes or CFD codes lies within the length scales that the two different computer tools can consider. A phenomenon such as the DCC, which is influenced by highly local effects, has to be modeled within a system code, traditionally, by considering only bulk-averaged values of main fluid variables, whereas, in the case of CFD codes, a higher spatial resolution of the flow and the consideration of smaller scales can be achieved. The higher spacial resolution comes at the cost of larger computational times.

Regardless of the length scales used, the phase change occurring at the two-phase interface is computed based on a local energy balance in those cells containing both phases and, implicitly, the interface. The interface and the vapor phase are

considered to be at saturation. Consequently, the liquid film in contact with the interface provides the only heat transfer resistance in the process of DCC. The calculation of the mass transfer rate Γ used as both source and sink term (depending on its sign) in the conservation equations was previously discussed in chapter 3.2. For the calculation of the HTC, one of the fundamental quantities for the calculation of the interfacial mass and energy transfer rates, a hybrid model has been developed which will be presented in the following chapter. The other relevant variables such as the temperature difference between the two phases, the IAD and the latent heat are obtained from the solutions of conservation equations, from the fluid properties, or are explicitly modeled in the code.

4.1 Development of a Hybrid HTC Model accounting for Microscopic and Macroscopic Eddie Scales

In order to overcome the drawbacks of stand-alone SRT based HTC models, an approach of a hybrid model is developed in this section. The stand-alone SRT based models can mainly be used after a parameter tuning based on experimental measurement data has been performed. The main differences between the two individual models consists in the manner in which they consider the length scales of the eddies responsible for the heat transfer from the interface towards the liquid bulk. A summary of the two individual SRT models is presented in the following table.

The hybrid HTC model whose development is shown in this section is based on the assumption proposed in [65] that the energy in a turbulent flow is carried predominantly by micro eddies when the turbulent Reynolds exceeds a threshold value of 500; below this value larger eddies are then mainly responsible for this transport. This assumption was applied to the mechanism of energy transport inherent to the surface renewal process and while assuming that the micro eddies are the

Variable \ Model	MiSE	MaSE
L_t	$\left(\frac{\nu_{liq}^3}{\epsilon}\right)^{1/4}$	$C_\mu \frac{k^{3/2}}{\epsilon}$
V_t	$(\nu_{liq}\epsilon)^{1/4}$	$C_\mu^{1/2}(\nu_l\epsilon)^{1/4}$
C	2	1.407
n	1/2	2/3

Table 4.1: Summary of the employed SRT based HTC models

main driving force for the renewal of the liquid layer in contact with the interface. Below the threshold value of the turbulent Reynolds numbers proposed by [65] of 500, large eddies take the main role for the surface renewal. The calculation of the HTC by the hybrid approach developed in this thesis is based on a relationship that takes into account these main driving forces and combines them to account for the different turbulent states expected during DCC in flow conditions that may lead to the generation of CIWH.

The liquid-side turbulent Reynolds number Re_t is defined in (4.1) where k, ϵ, ν represent the TKE, the turbulent eddy dissipation rate and respectively the kinematic viscosity. This form of the turbulent Reynolds number is proposed by Kolev, [65]. As presented in chapter 3.4.2, at least two transport equations have to be added to the system of PDE solved by a CFD code for the calculation of the required variables.

$$Re_t = \frac{k^2}{\epsilon\nu} \tag{4.1}$$

In this manner, a dynamic link is set up between the conservation equations, presented in chapter 3.2, the turbulent quantities, presented in chapter 3.4.2 and the calculation of the HTC. This system is in principle applicable to different flow regimes and turbulence intensities and does not require further parameter tuning or calibration, as will be discussed in chapter 6.

The selected value for the switch between the two individual models depends on several factors, two of which are particularly important namely, the model used for the simulation of the two-phase flow and on the turbulence model employed. A

higher value of the Reynolds turbulent number than the one proposed in [65] for the switch was found in the course of the work reported in this thesis to produce results closer to the experimental measurements for the solution procedure consisting of the VOF method plus the $k-\omega SST$ turbulence model in the simulations with CFD codes. Still, once the threshold value was determined, no further tuning was performed. Both the CFD and the system code simulations were performed with the same threshold for the turbulent Reynolds number, i.e. 2500.

4.2 Implementation of the new Hybrid HTC Model into the System Code ATHLET

The implementation of the hybrid HTC model was coded in the appropriate subroutines of ATHLET Version 2.2 cycle A. As the model relies on turbulence describing variables, such as the TKE k and the eddy dissipation rate ϵ, variables which are not directly available in one-dimensional flow models, special closure laws must be used to estimate their local effect on the fluid bulk. ATHLET in its Version 2.2 cycle A includes algebraic expressions for the calculation of these variables, which have been developed in such a manner that they can account for the possible flow patterns that can appear in horizontal or vertical flow configurations. For the calculation of the eddy dissipation rate ϵ the formulations presented in table 4.2 are used in ATHLET according to [3].

Expressions for ϵ		
Contribution	**dispersed flow**	**separated flow**
interfacial shear	$\frac{1}{2}\frac{c_d}{D_d}\frac{\rho_c}{\rho_k}w_r^3$	$\frac{1}{2}\frac{c_i}{D_i}\frac{\rho_c}{\rho_k}w_r^3$
wall friction	$\frac{1}{2}\frac{\zeta_w}{D_h}\frac{\rho_c}{\rho_k}j_c^3$	$\frac{1}{2}\frac{\zeta_w}{\delta_F}\frac{\rho_c}{\rho_k}w_r^3$
flow geometry	$\frac{1}{2}\frac{\zeta_{ref}}{D_{ref}}\frac{\rho_c}{\rho_k}j_{ref}^3$	$\frac{1}{2}\frac{\zeta_{ref}}{D_{ref}}\frac{\rho_c}{\rho_k}w_{ref}^3$
mass transfer	$\Gamma\frac{w_r^2}{\rho_k}$	$\Gamma\frac{w_r^2}{\rho_k}$

Table 4.2: Algebraic Expressions for the Calculation of the Eddy Dissipation Rate [3]

In table 4.2 the symbols c, ζ, j, w_r, ρ and D represent the shear coefficient, the friction coefficient, the superficial velocity, the relative velocity, the density and respectively the channel diameter. The indexes c, ref and k are used for the continuous phase respectively the reference value and the phase (*steam or water*). It is assumed that the relative velocity is responsible for the shear stress at the interface and is also used for the determination of the TKE in equation (4.2).

$$k = \frac{3}{2}w'^2 \approx \frac{3}{2}w_{rel}^2 \tag{4.2}$$

For the calculation of the IAD an additional transport equation is solved in ATHLET. The model can deal with both bubble and droplet flow with the appropriate IAD sink and source terms: bubble and droplet break-up and coalescence models, as well as bubble and droplet formation and disappearance models (*evaporation, entrainment and condensation*), while for the intermediate flow patterns an interpolation function is used [50].

4.3 Implementation of the new Hybrid HTC Model into CFD Codes

Two CFD codes were used in the work reported in this thesis, namely the commercial software ANSYS CFX and the open source software OpenFOAM.
In the case of the commercial computer code ANSYS CFX, the implementation of the hybrid HTC model was done by means of the CFX Expression Language (CEL), which is a powerful definition language enabling the user to add new relationships between the ANSYS CFX internal variables. CEL is an interpreted, declarative language developed to enable CFX users to enhance their simulations without the need of writing and linking separate external FORTRAN routines. It can be used to add new physical models, create additional solution variables, define property relationships and set boundary conditions and profiles. CEL includes many predefined functions and operators to allow easy customization of simulations in a number of ways. The user however, cannot control the time point at

which the solver algorithm evaluates the CEL-based addition, as this is managed internally by CFX. Using the CEL both individual SRT based HTC models have been implemented into ANSYS CFX. The code evaluates at each computational point the expressions of each HTC model and chooses based on the threshold value of the turbulent Reynolds number according to a step function which value of the heat transfer coefficient will be used for the evaluation of the source and sink terms influencing the employed conservation equations.

All developments to OpenFOAM have been directly built into the source code because of its open source character. In this way the user has full control on the time point at which specific variables and expressions are evaluated and equations are solved.

Before the hybrid HTC model could be implemented in OpenFOAM Version 1.7.1 an energy conservation equation had to be added to the PDE system that describes the flow. The newly developed OpenFOAM solver employing the VOF method is capable of simulating the DCC phenomenon. The implemented energy equation corresponds to equation to (3.15). Due to numerical problems, only a single mixture based fluid energy conservation equation could be implemented. Since for the phenomenon of DCC modeled in this thesis the steam is assumed at saturation, the lack of an independent vapor energy equation is not vital for the correct prediction of the phenomenon. If the vapor were subcooled or superheated, such an equation would clearly be necessary. Numerical problems arose because of the OpenFOAM's built in PDE solver, which has to process the equations in a segregated way. The matrix solver has to individually process each group of PDEs and cannot, up to OpenFOAM Version 1.$x.y$, simultaneously solve the assembled matrix containing all the linearized terms of the conservation equations. Because of this limitation and considering the strong coupling between the source and sink terms stemming from the explicitly treated interfacial phase-change, only the liquid energy equation was implemented. Even in this case under-relaxation techniques and an additional predictor-corrector iterative step had to be used in order to assure variable boundedness and final convergence. The additional corrector step checks whether the current time step is fully converged, i.e. whether

the iterative solving procedure of the conservation equations has converged. Additionally, a minimum number of *three* internal iteration steps has to be performed to assure that the residuals do not incidentally fall outside the relative convergence limits and will again over-shoot in the next iterative step.

4.4 Calibration of the new Hybrid HTC Model based on Experimental Measurement Data

For the calibration of the newly developed hybrid HTC model, which accounts for both macro scale and micro scale turbulent eddies, for the heat removal from the saturated two-phase interface, high resolution measurement data available from the LAOKOON experimental facility will be used. Only the results obtained with ANSYS CFX, will be presented in section 4.4.2, because the quasi-steady state simulation of this facility, with an imposed liquid level BC, was not successful with OpenFOAM. Even with an imposed hydrostatic outlet pressure, the liquid height continuously decreased within the OpenFOAM simulations. This resulted first of all in a wrong liquid height which again led to higher water temperature. Simulation results of all three SRT models, the two individual and the hybrid model are presented for the selected experiments carried out in this facility, in order to highlight the drawbacks of the stand-alone models for a quasi-steady state DCC situation. The measured data from a quasi-steady state flow are very well suited for the assessment of such a model, as the feedback from the flow dynamics is small in comparison to the main condensation phenomenon.

4.4.1 Description of the LAOKOON Experimental Facility

A series of experiments were performed in the LAOKOON facility at the Technische Universität München (TUM) for the investigation of the DCC phenomenon in horizontal two-phase flow conditions[44],[7], [46],[6]. The experimental set-up of the facility consists of a rectangular channel, $L = 1200mm$ x $H = 106mm$

x $W = 79mm$ with well insulated walls as seen in the schematic representation shown in figure 4.2. This figure shows a flow-wise cut of the facility, while figure 4.1 represents the cross section of the flow channel. The LAOKOON facility was developed for the experimental investigation of DCC with saturated dry steam introduced from an inlet at the upper part of the channel and with subcooled water injected through a second inlet at the lower part of the channel. This special set-up was used in order for the flow to develop a steady quasi-$2D$ pattern with subcooled water flowing along the bottom of the channel and saturated dry steam flowing on top of the liquid with nearly adiabatic wall conditions.
The case selected for the assessment of the hybrid HTC model corresponds to a flow regime with a smooth water surface and no waves.

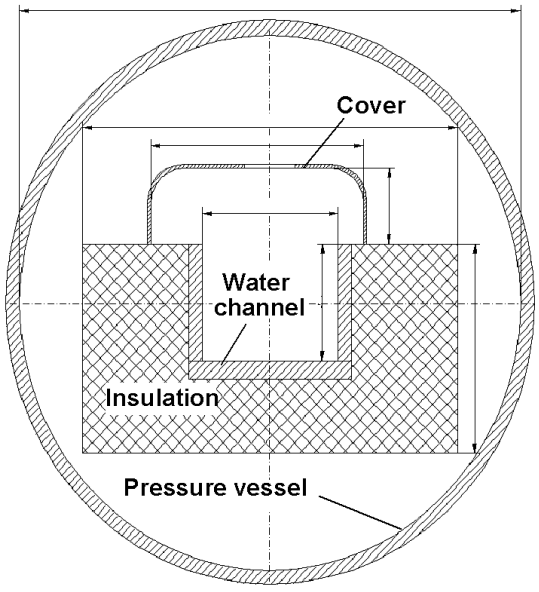

Figure 4.1: Flow-wise cross section of the LAOKOON experimental facility [6]

The data acquisition system recorded the measurements of several variables. For the assessment of the CFD simulations with the SRT based HTC models, the liquid level, the vertical temperature measurements, the system pressure and the inflow rates have been used. The liquid level and system pressure are initial conditions for

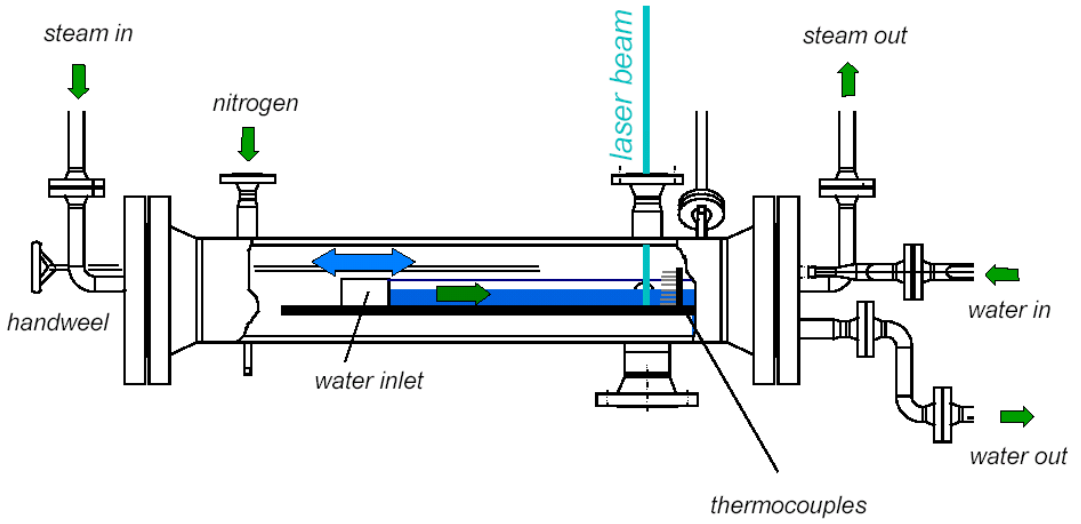

Figure 4.2: Channel cross section of the LAOKOON experimental facility [7]

the simulations, the inflow rates are used as BCs and finally, the available vertical temperature profile is used for benchmarking the different SRT based HTC models. For the measurement of the vertical temperature profile 12 micro, NiCr-Ni PT100 thermocouples with a diameter of $\Phi = 0.5mm$ were employed. The thermocouples were mounted stream-wise in the flow direction and had a length of $10mm$. The relative measuring error of these thermo-couples was 2%. It is important to mention that later in this work, when the computer simulation results are discussed, the location of the thermocouples will be considered at the sensible tip of the sensor. Considering this convention, results located at $790mm$ from the inlets will be compared against experimental data delivered by the sensors mounted into the flow at $800mm$ from the inlets in the real facility.

The relative measurement error of the system pressure was 0.11%, typical of the capacitive pressure sensors used in the case of the steam inflow rate, a device based on vortex measuring was employed, with a relative error of 0.9%. In the case of the liquid phase, a Coriolis based flow meter with a relative error of 0.2% was used.

The water liquid level was not measured directly but rather by the interpretation of:

- the standard deviation of the temperature measurement,
- Laser Doppler Anemometer (LDA),
- water velocity measurement.

By combining the three indirect measurement procedures for the water level a relative measurement error of $\pm 1mm$ was achieved. More insights into the data acquisition system and the employed sensor type can be found in Ruile [44].

4.4.2 Simulation of the LAOKOON Experimental Facility

This chapter contains the ANSYS CFX CFD simulation results, employing the two individual SRT based HTC models as well as the hybrid HTC model, of the LAOKOON experimental facility. First, as part of the calibration phase of the switch used to blend between the individual SRT based models, CFD simulations have been performed for the LAOKOON experimental facility. The calibration process is started with the comparison of computer simulations against quasi-stationary flow condition measurement data, which exclude the feedback of transient flow. For the set-up of the simulation domain of this experimental facility, only a part of the test-section was considered, which includes the central test-section: the horizontal test channel. This was done in order to optimize the computational resources. Owing to the relative small influence of the lateral walls on the bulk flow, only a $2D$ slice of the channel was meshed for the CFD simulations as specially arranged measurements have confirmed that the side walls have a negligible influence on the two-dimensional flow pattern. The third dimension, the channel depth, was simulated with only two nodes and by imposing a symmetry BC. A similar computational domain was used for the simulations of this experiment within the ECORE project, [66]. A schematic representation of the meshed domain, the imposed BCs and the initial values are presented in figure 4.3. The good thermal insulation of the walls allows the use of adiabatic wall conditions.

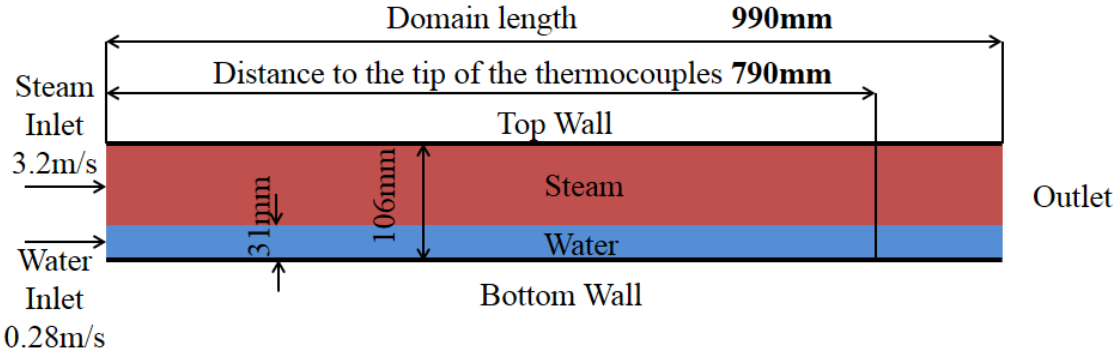

Figure 4.3: Flow-wise cross section of the LAOKOON experimental facility [4]

The three different implemented SRT based HTC models presented in section 3.5 will be benchmarked and validated against experimental results. The benchmark starts with the comparison between the two individual HTC models and later the results of the hybrid model are introduced. As the two individual SRT based HTC models are accounting for different eddy sizes, the comparison is carried out beginning exactly with these quantities, i.e. the eddy velocity and eddy length scales.

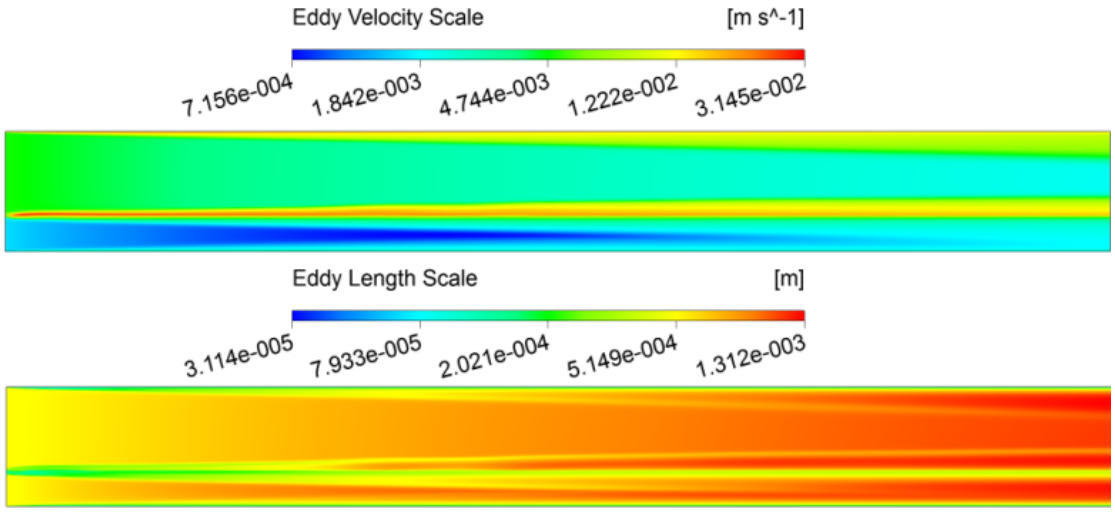

Figure 4.4: Eddy velocity and Length Scale based on the MaSE model for the CFX simulation of LAOKOON [4]

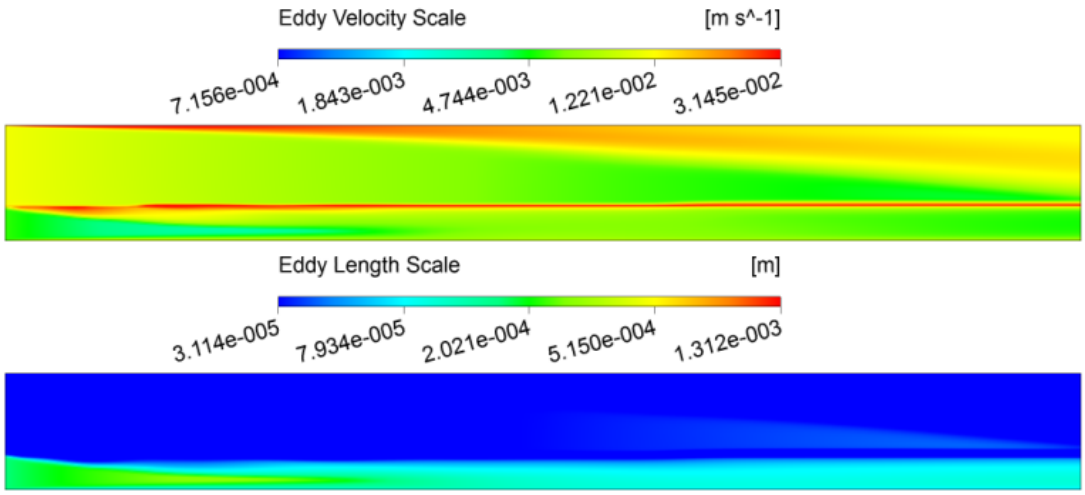

Figure 4.5: Eddy velocity and Length Scale based on the MiSE model in the CFX simulation of LAOKOON[4]

Comparing the eddy length scales computed with the two individual models, it can be noted that the macro eddies have a length scale ranging from $10^{-4}m$ to $10^{-3}m$, while the range of the micro eddies lies between $10^{-5}m$ to $10^{-4}m$. If only micro eddies are considered in the HTC model an important observation is that in the proximity of the interface almost constant length scales appear. In the case of the macro eddies based HTC model, a clear peak can be noticed close to the inlets due to the increased turbulence caused by the joining of the two individual streams, liquid and gas. The cross-sectional profiles of the eddy velocity scale exhibit a maximum close to the interfacial zone, for both individual SRT models. In the case of the large eddies the eddy velocity scales range, from $10^{-5}m/s$ to $10^{-2}m/s$, while the micro eddies have a higher minimum velocity scale of $10^{-3}m/s$ and the same maximum one as the macro scale eddies, namely $10^{-2}m/s$. Still, both models show a decrease in the eddy length scales and an increase in the eddy velocity scale close to the free surface. This leads to an overall decrease in the SRP, figure 4.6, resulting in a peak value of the HTCs in this region. Similar, the condensation rate experiences a maximum in the interface region. It is obvious that the corresponding values of the HTC based on the smaller eddies will have considerably higher values than that based on macro eddies, due to the

considerably smaller eddy length scales computed by the model. The enhanced HTCs of the Hughes and Duffey model will result in a higher water temperature throughout the channel, including at the probe location. This is owed mainly to the heat transport accompanying the condensation and less to the heat conduction between the two phases, figure 4.7.

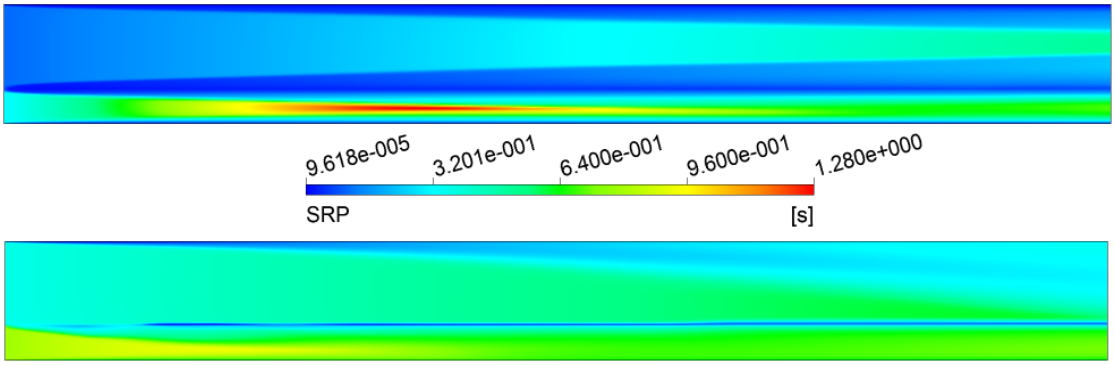

Figure 4.6: Comparison of the SRP computed by means of the MaSE and the MiSE model based on the surface renewal theory SRT predicted by the CFX simulations of LAOKOON

This affects the temperature gradient which is the driving force for CIWH, meaning that from the point of view of the HTC there is a high condensation potential even at lower turbulence. The corresponding channel-wise temperature distribution is depicted in figure 4.8. By analyzing the temperature distribution it can be noticed that the Shen et. al model conserves a sharp profile over the interface area due to the lower condensation rates. When only the Kolmogorov eddies are considered for the calculation of the HTC, the liquid almost reaches the saturation temperature towards the domain outlet. For the simulation of eventual CIWH a sharp temperature profile between the saturated steam and the subcooled water is required as it can enhance the capability of predicting such an event.
The results of the hybrid SRT based HTC model are summarized in the figures 4.9 to 4.10. As the hybrid HTC model considers both small and large scale eddies responsible for the heat removal, based on a critical turbulent Reynolds value of 2500, a maximum in the HTC values can be observed close to the interface. The model chooses the micro eddies for the calculation of the HTC in the area of the

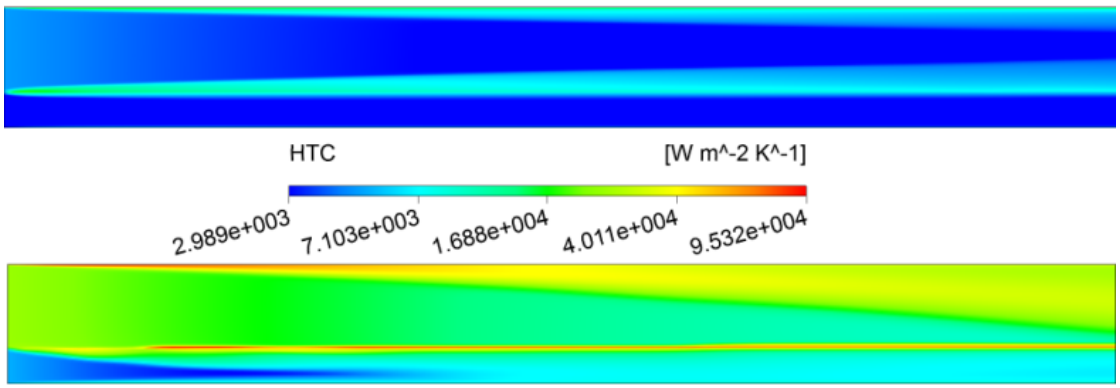

Figure 4.7: Comparison of the HTC by means of the MaSE and the MiSE model in the CFX simulation of LAOKOON [4]

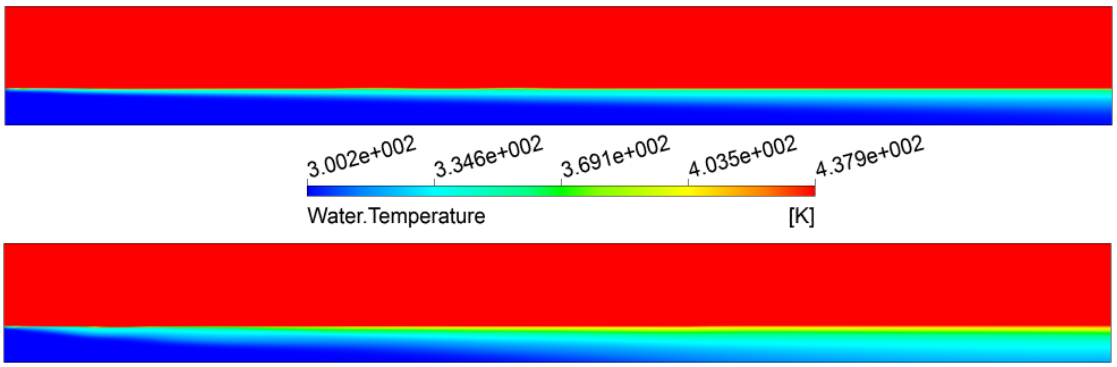

Figure 4.8: Comparison of the channel-wise temperature profile as calculated using the MaSE and the MiSE based HTC model in the CFX simulation of LAOKOON

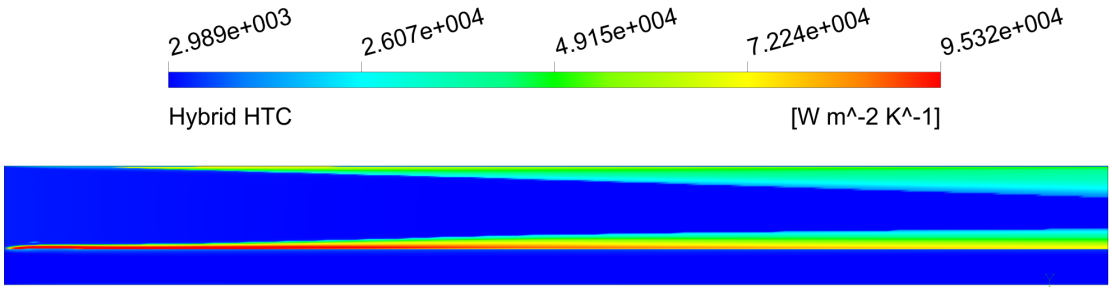

Figure 4.9: Flow-wise HTC distribution by means of the hybrid model in the CFX simulation of LAOKOON

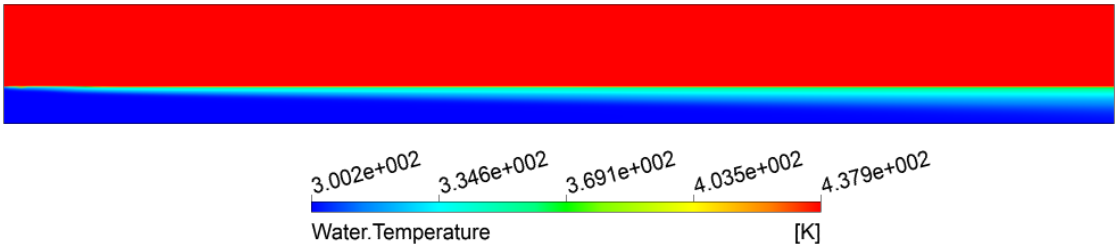

Figure 4.10: Flow-wise temperature distribution by means of the hybrid model in the CFX simulation of LAOKOON

two-phase interface as in that region the turbulent Reynolds number exceeds the critical value of 2500.

The comparison of the CFD simulations against measurements is performed for the cross-sectional temperature profile at the location $790mm$ downstream from the inlets, figure 4.3, where the thermocouples are mounted. The figure contains the temperature profiles as computed by the hybrid model using three different Reynolds threshold values and the two individual SRT based HTC models alongside with the experimental data. By varying the critical Reynolds number, a small sensitivity study was intended. The threshold was varied and set to the values 100, 500 and 2500.

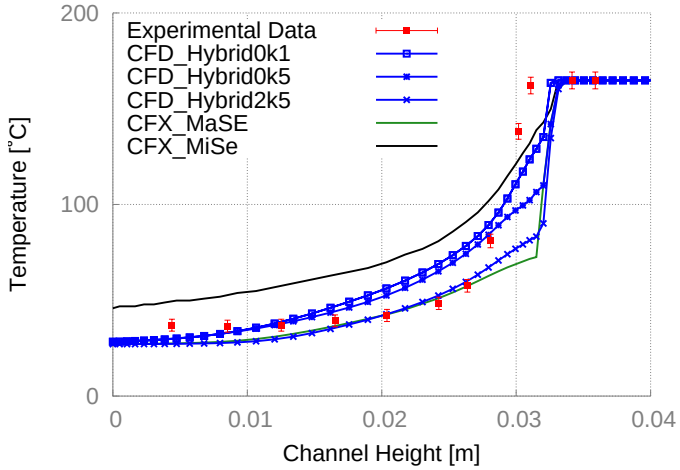

Figure 4.11: Temperature profile at the measurement plane of the LAOKOON facility

Only the bottom part of the transverse temperature profile was used in figure 4.11 because the upper part of the channel has a void fraction of unity, thus not being relevant for the validation process. The measured data including the corresponding error-bars was represented using red squares. The black, green and blue curves represent the CFX simulation using the MiSE model, the MaSE model and the parameter study for the turbulent Reynolds threshold of the hybrid HTC model. The evaluation of the transverse field representation of the HTC, computed based on micro scale eddies, concludes that this model overestimates the HTC, thus resulting in a higher water temperature. The high water temperature is caused by the high local condensation rates. Also, the sharpness of the temperature profile, which acts as one of the driving forces for CIWH, is lowered when only the micro eddies are accounted for heat removal. The other individual SRT based model employed, i.e. Shen et al. model, underestimates the HTC but it keeps a sharp temperature profile conserving the high condensation potential. The slope of the temperature gradient over the channel height is well predicted by the hybrid model using the value of $Re_t = 2500$ as the threshold between the two stand-alone SRT models. The temperature profile as computed by the hybrid models, using the two higher values of the threshold, lies close to the region of the measurement data for almost the entire channel height except at the bottom of the flow channel and close to the interface. Here the computed temperature is lower for the hybrid SRT model than in the experiment due to the following reasons:

- The first difference is caused by the wall computational BC that imposes a zero gradient on the computed variable toward the wall and neglects the Fluid-Structure Interaction (FSI) and the corresponding heat transfer,
- All simulations show a lower temperature than the saturated steam at the interface, which could indicate the fact that the imposed water height was set too low. Even the overestimation of the HTC results in too low temperature at the interface in the simulations employing the MiSE model. The channel height is not directly measured during the experiment, but derived and has a maximum absolute measurement error of approx. $1mm$, as presented in chapter 4.4.1.

These three simulations with different turbulent Reynolds threshold values indicate that the temperature profile is clearly sensitive to this parameter. Figure 4.11 shows that if the Reynolds turbulent threshold value is selected too low, then the hybrid HTC model delivers values close to the micro eddies based stand-alone model and thus overestimates the condensation rates and consequently the temperature. If the values for the critical Reynolds number are chosen higher the hybrid model converges towards the results of the stand alone model considering only large eddies for the heat removal from the interface. Even if it appears that other threshold values would eventually deliver better results for this particular case of quasi-steady state horizontal two-phase flow, one has to bear in mind that this model will be applied for the more complex cases of transient horizontal flows. The higher value for the switch is recommended for the system consisting of VOF and the $k-\omega$ SST turbulence model and will also be used in the system code ATHLET.

The conclusion that can be drawn from the first validation step of the newly developed hybrid HTC model is that the simulations employing only the individual SRT based HTCs justify the need of a hybrid model for the realistic simulation of DCC. When only micro eddies are accountable for the heat removal from the interface, the liquid can quickly become saturated, hence damping the condensation as the HTC is overestimated. If only macro eddies are considered in the HTC model, an underestimation of this variable is performed; still a steep temperature gradient is preserved, similar to the experimental measurement data. The hybrid model together with a suitable threshold value for the turbulent Reynolds number preserves the advantages of both models and clearly improves the predictive qualities of the computational simulations.

Chapter 5

Description of the Experiments used for the Assessment of the New Hybrid HTC Model

The design of the different experimental facilities and the description of the experiments will be presented within this chapter. The hybrid model was calibrated and together with the individual SRT models it was bench-marked against measurement data of a horizontal two-phase flow. This chapter contains the simulation results of the hybrid HTC model as it was implemented in the computer codes to accurately simulate heavy DCC as the precursor of water hammers. The analyzed facilities have the geometrical characteristics required for the appearance of CIWH as presented by Griffith [33]. The PMK-2 has a horizontal test-section while the slope of the TUHH facility is less than 2.4°. The ratio between the length of the test-section and its inner diameter is in the case of the PMK-2 facility approximately 39, while in the case of the TUHH experimental facility it is approximately 50. The water subcooling was always larger than $20°C$ and the injection rate was always smaller than the one corresponding to a Fr of unity. All experiments were initiated with the test-section full of vapor. These initial conditions and BCs correspond to a set-up which is prone to CIWH as presented by Griffith in [33].

5.1 Description of the PMK-2 Experimental Facility

The horizontal PMK-2 experimental facility built at the KFKI Institute, Budapest Hungary, has a complex set up and flow characteristics. A schematic representation of the PMK-2 facility is represented in the figure 5.1. Several experiments were performed at this facility, in which different phenomena have been analyzed. One of the experimental series in the WAHALoads project included the analysis of the CIWH phenomenon. The WAHALoads project took place within the $5th$ EU framework and studied transients involving two-phase flow water hammers and the induced loads on materials and structures of NPP components. A total of 35 experiments have been performed within the frame of the four year WAHALoads project, whereby a CIWH event occurred in 26 cases, [37] and [38]. The initial conditions of these experiments together with the observation whether a CIWH effect occurred, are summarized in the Appendix A. The need for the experimental analysis of accident scenarios in the Russian type Pressurized Water Reactor (PWR) Water-Water Power Reactor (VVER) Series 440 NPP led to the creation of this experimental facility consisting of an integral thermal-hydraulic model of a down-scaled steam line. The goal of this experimental series was to deliver system code and CFD validation grade measurement data. The insights at the phenomenological level gained at this facility can be extrapolated to other reactor types while the measurement data is a highly valuable database for horizontal two-phase flow, including DCC and for the two-phase flow dynamics during CIWH events.

All 33 experiments were initiated by opening the valve labelled number (6) in figure 5.1 isolating the pressurized feed-water tank containing pressurized subcooled water from the experimental facility. A nitrogen gas cushion pressurized the subcooled water, which after the opening of the valve, entered the test-section through the elbow (3). Subcooled water would then interact with the stagnant steam which initially filled up the test-section. The test rig had an internal pipe diameter of $73mm$. From an instrumentation point of view, the test-section was equipped with

four void-temperature sensors marked as number (8), three pressure transducers marked as number (3) and a wire mesh sensor labelled with number (9) in the figure 5.1. The elbow on the left hand side marked with number (2) connects the steam generator with the test-section. The sensors number (8) and (3) deliver highly local values, while the wire mesh sensors yields area averaged void fractions for the entire pipe cross-section. The measurement data recorded by the Wire Mesh Sensor (WMS) are valuable for the reconstruction of the flow pattern and thus, for the assessments of CFD codes. This local information is only of limited value for the validation of 1D system codes.

The particularity of the instrumentation available on this experimental facility compared to that mounted in the other analyzed facilities described later is the WMS. This measuring device consists of two parallel planes each including a number of 12 electrodes with a $2mm$ vertical pitch between the planes. By measuring the distribution of the instantaneous conductivity and with prior calibration based on the conductivity of the liquid phase, the void distribution can be reconstructed with a resolution equal to the wire horizontal pitch of $5.9mm$ and a time resolution of $1kHz$. The WMS is designed to be used under system pressures up to $7MPa$ and temperatures up to $285°C$ [67]. More detailed information about the instrumentation installed in the test facility and especially about the WMS can be found in [8]. System codes yield only coarse volume averaged values, for instance for the void fraction and thus can be compared only to some extent against highly local measurement data as those of the void-temperature probes. On the other hand, the area averaged results of the void fraction distribution give a hint on the two-phase flow dynamics and can be compared with interpreted system code results.

A very efficient thermal insulation of the test-section's walls was required in order to reach a void fraction close to unity at the beginning of the experiments, while also simplifying the BCs for the latter validation process. Still, at the beginning of the experiments a thin liquid film is recorded by the WMS, which is very difficult to initialize in the computer simulations, as no detailed information is available from experiment logs performed at the PMK-2 facility. This liquid film has an in-

fluence on the overall water temperature since the subcooled water injected from the water tank mixes with this thin film probably available along all horizontal sections, resulting in an increase of the (mixture) water temperature. Acquired data from the WMS will also experience an earlier change in their values when the injected water together with the thin liquid film both reach the sensor sooner. The influence of the stored energy within the pipe walls is difficult to model during the computer simulations. Its neglection leads to lower global water temperatures in the simulations compared to the experiment. For instance, a lower water temperature is observed in the simulation as the water travels through the pipe system to reach the test-section because it does not receive the energy stored in the actual pipe walls.

The PMK-2 experiment simulated with the CFD codes is number 05 A. In this experiment subcooled water at 298 K and a mass flow rate of 1.01 kg/s was supplied to the test-section which contained saturated steam at an initial system pressure of 1.45 MPa. Considering the smaller computing times required by a system code analysis, the full PMK-2 experimental series consisting of 33 experiments was simulated with ATHLET.

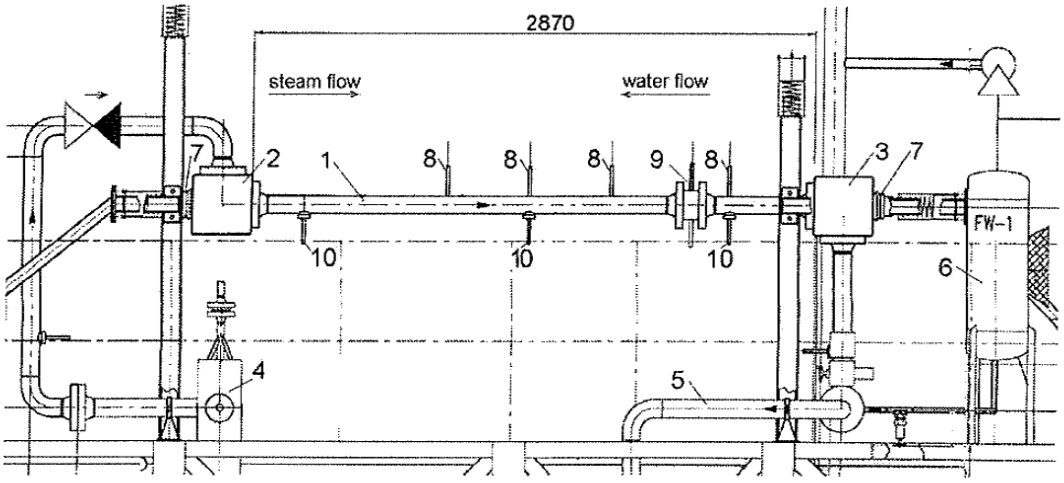

Figure 5.1: Schematic representation of the PMK-2 experimental facility [8]

An interpretation of the experiments based on the initial conditions such as water subcooling and system pressure shows a high scattering of the resulting CIWH. Swidersky et al. [9] presented a 3D map of pressure peaks as a function of the initial feed-water subcooling and system pressure in figure 5.2. This plot shows that even under well defined initial and boundary conditions, the condensation phenomenon is highly stochastic. A more detailed analysis based on key dimensionless numbers will be presented in the subsection 6.1.2.

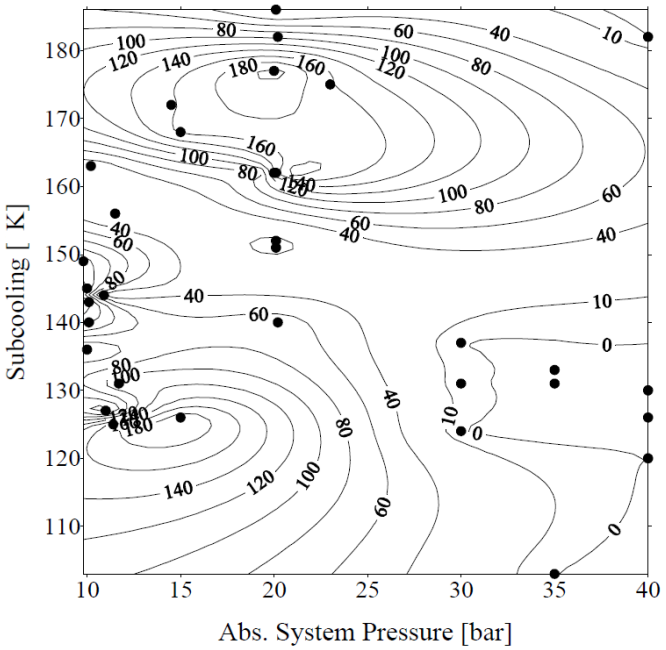

Figure 5.2: Interpolated isobars of measured pressure peaks (dots) at the PMK-2 test facility [9]

5.2 Description of the TUHH Experimental Facility

The experimental facility built at the TUHH in Germany consists of a central test-section with an inner diameter corresponding to DN50 and an approximate length of $2.5m$. The ratio of the overall test-section length to its inner diameter is approximately 50. Separators are connected on both ends with the test-section, the one on the left hand side is connected to the Steam Generator (SG) labeled separator (1) in figure 5.3. The maximum mass flow rate of the connected SG with a thermal output of $9kW$ is $8kg/h$ of saturated steam.

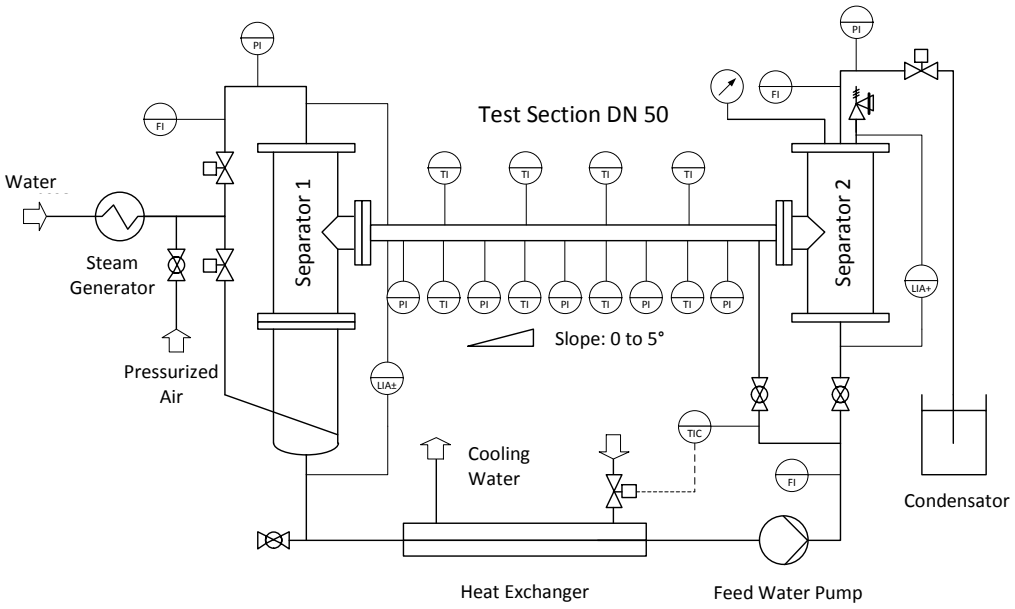

Figure 5.3: Schematic representation of the TUHH experimental facility [10]

Subcooled water is provided over a T-junction vertically to the test-section, close to the right hand side separator. The installed feed-water pump delivers a maximum volumetric flow rate of $6m^3/h$. This flow rate can either be injected vertically, through the T-junction into the test-section or be added through the separator (2). By adding water to the test-section through the separator (2), counter-current

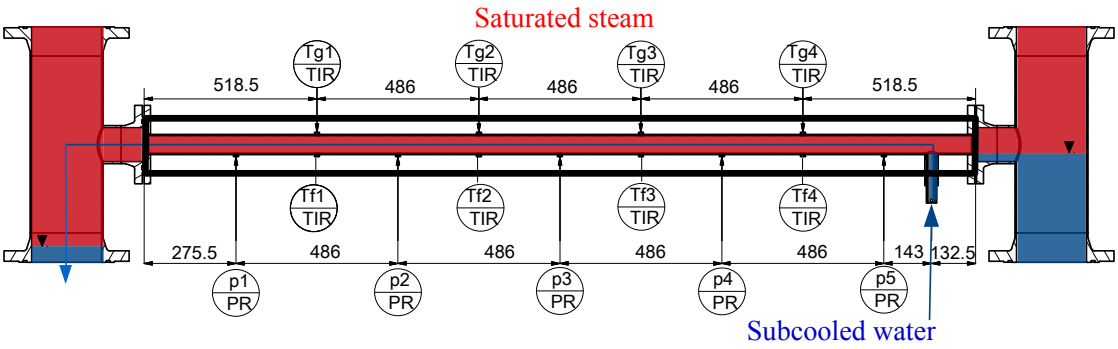

Figure 5.4: Schematic representation of the test-section of the TUHH experimental facility, adapted from [11]

two-phase flow can be investigated. Proper thermal insulation is added to the entire section of the experimental facility carrying both steam and water, as the considered experiments are to be initiated from a steam filled test-section. In the case of the CFD simulations, this is translated to idealized adiabatic BCs for the pipe walls. The data acquisition system set up in the test-section marked by the black region in figure 5.4 includes five pressure transducers and eight thermo-couples. The pressure transducers are mounted at the bottom of the pipe labeled from *p1* to *p5*, while the eight thermo-couples are mounted diametrically opposing each other at the top of the pipe, labeled *Tg*, and bottom of the pipe, labeled *Tf*. Very high sampling rates are required for the accurate recording of pressure surges such as the CIWH. Thus the data is acquired with $50kHz$, while the sensors' lag is smaller than $5\mu s$, [10]. These fast pressure transducers are mounted equidistantly, with a pitch of $486mm$. The volumetric flow rate of subcooled water is measured using a vortex-based measurement device, corrected with a Coriolis-based measurement device. This correction step had to be performed as vortex-based measurement devices are not suited for the highly transient phase of pump start-up. Typical measurement errors for the employed Coriolis-based measurement devices are around 0.15%. The facility was built with the possibility of flexibly changing the inclination to the horizontal of up to 5°. A more detailed presentation of the TUHH experimental facility can be found in [10] and [11].

The facility was designed bearing in mind the following objectives: the measurement of pressure, temperature in the test-section and liquid level in the two separators. The test-section was designed with a length to its inner diameter fraction which is typical for power plants. Additionally the special feature of adding a transparent pipe section for the visual investigation of the CIWH phenomena was pursued [10]. Creating a database for the validation of computer codes as well as for the development of the hybrid HTC model were typical goals considered in the design phase of this experimental facility.

Chapter 6

Assessment of the New Hybrid HTC Model for the Simulation of Transient Two-Phase Flow with Finite Volume Computer Codes

This chapter includes the computational results of the different computer codes used for the simulation of DCC as the driving force for CIWH together with the benchmark of the SRT based HTC models employed.
As computer codes that consider a different number of dimensions were used to analyze the flow, additional post processing is needed to fully validate the employed models; for the calculation of the HTC. This is required when the results of the system code simulations are discussed. For the validation of the hybrid HTC model, measurement data from different experimental facilities are used. The results of the simulations will be progressively presented. The results of the computer simulation of a horizontal quasi-steady state two-phase flow, at the LAOKOON facility, have been used for the calibration of the newly developed SRT based HTC model in chapter 4.4.2. The hybrid HTC model will now be assessed based on the results of the simulations of fully transient horizontal two-phase flow experiments.

The data is provided from the facilities PMK-2, chapter 6.1 and TUHH, chapter 6.2.
In the case of the two fully transient flow facilities, the overall behavior of the system consisting of VOF and SRT based HTC models will be validated against measurement data. The system code will be used only to simulate experiments of the transient two-phase flow because a comparison of 1D simulation results with high resolution measurement data from the LAOKOON facility would be inconclusive.
The simulation results of the PMK-2 experimental facility include both the results obtained with the system code ATHLET and ANSYS CFX. The system code simulations include the typical 1D approach and an approach with a quasi-2D computational grid. In the case of the CFD analysis, the results of all three HTC models will be presented and discussed in order to underline the necessity of a hybrid model for the calculation of the HTC for the flow patterns spanning from horizontal stratified to slug and plug flow. These flow patterns have characteristic turbulence intensities reflected by turbulent quantities such as the TKE and the turbulent eddy dissipation rate.
The TUHH experimental facility, which was developed and build within the framework of the CIWA project, will be simulated only with the open-source CFD toolbox OpenFOAM. The results of this analysis will be presented in chapter 6.2.
The CFD simulations have been performed on structured grids, i.e. o-grids. In order to minimize the computational time, only one half of the axis-symmetrical computational domain has been meshed and a symmetry BC was used for this patch to account for the other pipe half. A grid independent study however has not been performed due to the relatively long problem times and consequently long computational times of each experiment.

6.1 Simulations of the PMK-2 Experimental Facility

The PMK-2 facility in this set-up was used for a total of 33 experiments of horizontal two-phase flow, where subcooled water was injected into a steam filled test-section. The complete matrix of the experiment series is presented in appendix A. The experiments are described in various papers or journal articles in the literature; the most comprehensive sources have been published within the framework of the WAHALOADS project: [37] and [38] etc. Out of the 33 documented experiments conducted at this facility, 26 recorded a CIWH event.
Chapter 6.1.1 presents the ANSYS CFX simulation results, including runs with the individual SRT based models, the MiSE and MaSE models.
The assessment of the newly developed HTC within the system code ATHLET will be presented in chapter 6.1.2.

6.1.1 Simulations of the PMK-2 Experimental Facility with ANSYS CFX

In order to justify the need of an hybrid HTC model for the reliable simulation of CIWH in horizontal two-phase flow with free surface, the ANSYS CFX results of each of the individual SRT models will be discussed.
During the design of the computational grid employed in the simulations, the influence of the measurement sensors on the flow was not taken into account. Even if intrusive measurement techniques such as the WMS are implemented into the test section, the effort of considering such sensors in the computational grid is considerably high and has thus been neglected. It also results in a correspondingly higher computational time because of a very detailed mesh refinement needed near the sensors. It is however believed that the effect of the grid on the development of the CIWH away from the sensor is not important enough to require explicit modeling.

The flow patterns observed in the CFD simulation with the Shen et al. model are reported at key points in time in figure 6.1. As already explained, this model takes into account the influence of large turbulent eddies in the condensation process through the structure of the HTC correlation.

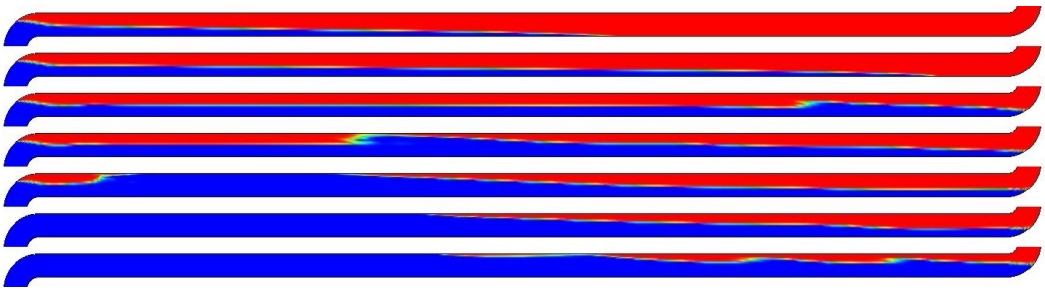

Figure 6.1: Flow pattern predicted with Shen's model in the PMK-2 facility at key points in time (7.5 s, 9.0 s, 11.5 s, 12.5 s, 13.5 s, 15.0 s, 16.5 s), represented by the void fraction (red: steam, blue: water) [4]

The summary of the key flow patterns observed in the simulation using the Shen's HTC model is the following: the water reaches the horizontal test-section and flows from the left to the right elbow; first and second figure in the sequence 6.1. A roll-wave is formed when the water reaches the right elbow; third figure in the same sequence. This wave grows and is accelerated towards the left elbow due to a pressure decrease in the left part of the test-section as a result of DCC on the surface of the subcooled water. This allows the flow to evolve from stratified to slug; forth picture in the sequence. The liquid bulk entraps a steam pocket when the water wave reaches the top of the horizontal pipe, fourth picture in the sequence. The steam bubble condensates slowly, in approximately 1.5 s allowing the water to replace it. At the same time the flow pattern changes locally in the pipe from horizontal stratified flow first to wavy flow and after that, the waves grow to form a slug. The whole process is influenced by the high local condensation rates close to the right elbow in the computational domain, sixth and seventh picture in sequence 6.1. The simulation ends when the horizontal test-section is completely filled with water. The effect of high local condensation rates can be ascertained by analyzing the relative pressure field as shown in figure in 6.3. At this moment, when the steam pocket is completely isolated due to the flow pattern change from wavy

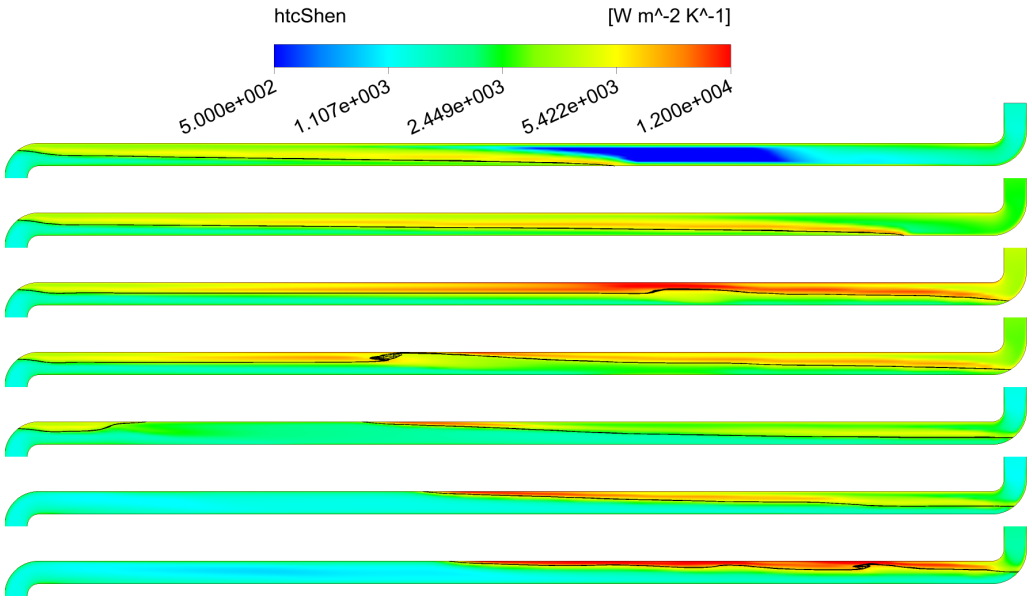

Figure 6.2: Computed HTC using Shen's model in the PMK-2 facility at key points in time (7.5 s, 9.0 s, 11.5 s, 12.5 s, 13.5 s, 15.0 s, 16.5 s). Black lines represent the contour for a volume fraction of 0.5, corresponding to the location of a two-phase interface [4]

to slug flow, a local decrease in pressure is observed; frame four in figure 6.3. High values of the HTC have been computed immediately before the entrapment, as the steam creates additional shear at the interface while it is drawn into the pocket. The additionally drawn steam tries to compensate for the DCC, figure three in 6.2. No special increase in the IAD is observed as the turbulence increases. The fact that within the VOF modeling approach the turbulence has no direct feedback on the IAD is remarked as a potential limitation of this methodology to simulate the CIWH phenomena through all stages, from the wave pattern formation to the bubble collapsing and subsequent pressure peaks. As already noticed in the case of the horizontal quasi-steady state flow in section 4.4.2, the Shen et al. model under-predicts the HTC values. The resulting condensation rates cannot accelerate the liquid slug to the required velocity, as it is the case in the typical sequence leading to a CIWH event, and thus the pressure increase is not correctly predicted.

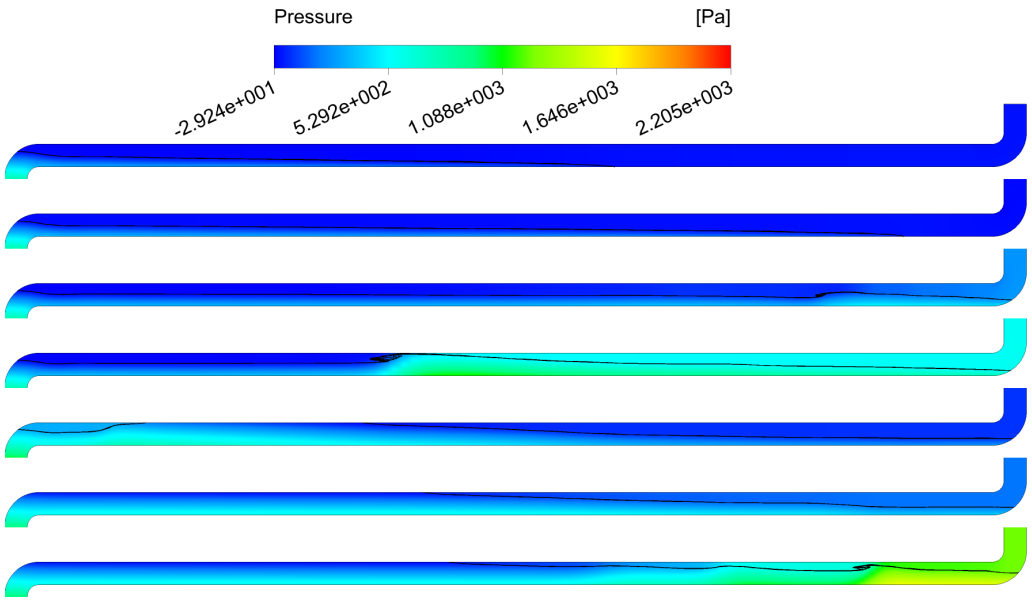

Figure 6.3: Computed pressure using Shen's model in the PMK-2 facility at key points in time (7.5 s, 9.0 s, 11.5 s, 12.5 s, 13.5 s, 15.0 s, 16.5 s). Black lines represent the contour for a volume fraction of 0.5, corresponding to the location of a two-phase interface

The results of the CFD simulation using the Hughes and Duffey's HTC model accounting for the micro eddies, show in comparison to the Shen et al. model, a sudden change in the flow regime from stratified to slug flow, figure 6.6.
Key points in the simulation show the strong coupling between the condensation rate and the flow regime. The first and second pictures in figure 6.6 show a stratified horizontal flow, which changes locally to wavy flow at the tip of the water film, second picture in figure 6.6. The water wave is accelerated towards the left-hand side bend by the steam condensation, quickly evolving into a slug; pictures three and four in figure 6.6. Picture four in figure 6.6 shows the collapsed steam pocket. The HTC is so large that the enhanced condensation rate accelerates the slug resulting in a CIWH event. As the flow in this simulation clearly differs from that in the experiment, no results will be further discussed in the HTC assessment process. Yet, this model is valuable as it shows that high HTC values are required to induce a CIWH. A pressure surge of approximately 2 *bar* of over-pressure was calculated, which is clearly lower than the measured value shown in figure 6.7. It

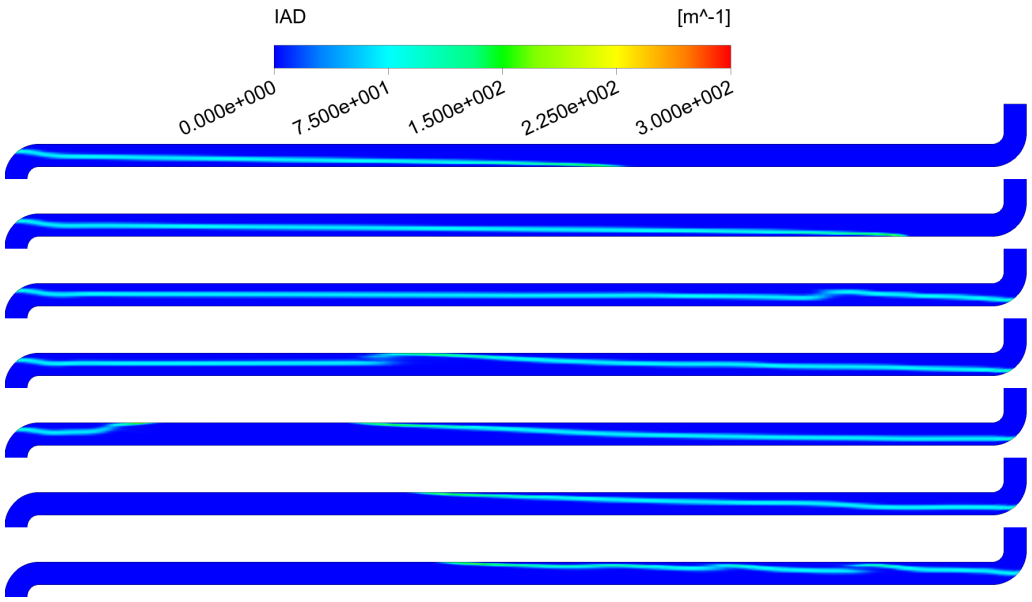

Figure 6.4: Computed IAD using Shen's model in the PMK-2 facility at key points in time (7.5 s, 9.0 s, 11.5 s, 12.5 s, 13.5 s, 15.0 s, 16.5 s). Black lines represent the contour for a volume fraction of 0.5, corresponding to the location of a two-phase interface

has to be mentioned that the highest pressure peak in the entire computational domain in the simulation using the MiSE was approximately 4.7 *bar* over-pressure. In the case of the CFD results with the hybrid HTC model, the flow pattern differs from the one where the individual SRT models are employed. The strong feedback between flow pattern and condensation rate can be observed when the hybrid model is applied, similar to the simulation when the Hughes and Duffey model was used. In the first moments of the simulation, first picture in figure 6.8, both the SRT model based on large eddies, the Shen et al. model and the hybrid model show a similar flow behavior but as soon as the water reaches the horizontal test-section turbulence is enhanced due to the pipe bend, thus increasing the condensation rates, second picture in figure 6.8. As a result, the flow changes locally from horizontally stratified to wavy flow, due to the local decrease in pressure; figure 6.9. The flow pattern evolves locally into slug flow when the water wave reaches the top of the pipe, pictures three, four and five in figure 6.8. The entrapped steam bubble collapses due to DCC, accelerating the water wave towards the left

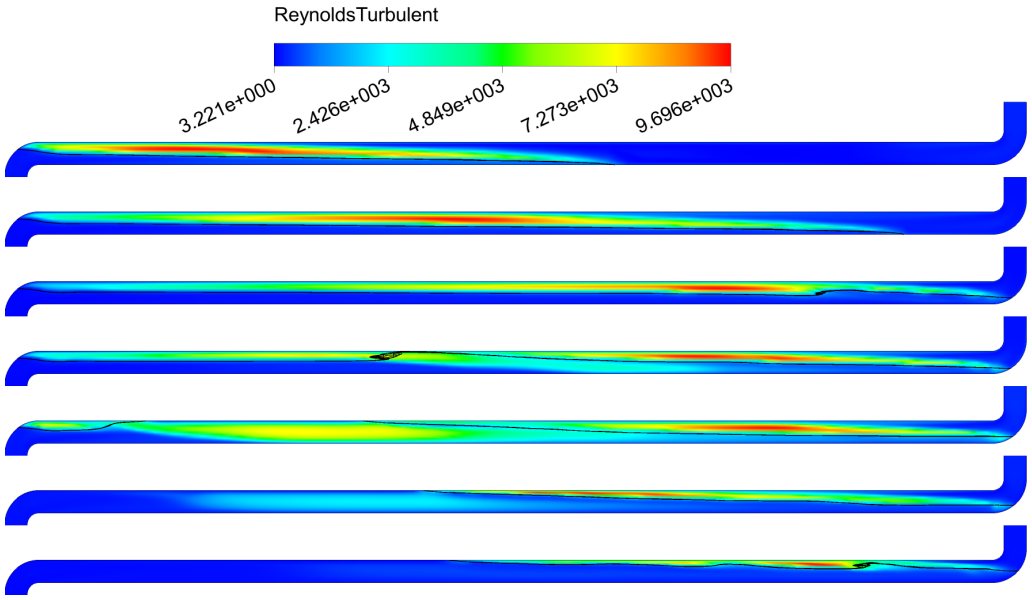

Figure 6.5: Computed turbulent Reynolds number using Shen's model in the PMK-2 facility at key points in time (7.5 s, 9.0 s, 11.5 s, 12.5 s, 13.5 s, 15.0 s, 16.5 s). Black lines represent the contour at volume fraction at 0.5 corresponding to the location of the two-phase interface

bend. The flow continues from left to right with several other local changes in the flow pattern until the water finally fills up the entire test-section and exits the computational domain. This acceleration of the water due to steam bubble collapse can act as the driving force of CIWH.

After the presentation of the flow patterns developed in the three different CFD simulations, the assessment of the results will be based on the comparison against experimental measured data. The available data include four locally measured temperature values plus four locally measured void fraction values. These values were recorded at the location of the VT1 to VT4 sensors, as shown in figure 5.1. The plots displaying the computer simulation results against experimental data are presented in a matrix form: the first column contains the temperature values while the second column contains the void fraction values. Both show the values at the probes' location in an increasing order starting from VT1 at the top, to VT4 at the bottom. Additionally, the WMS located at the position number 9 in the PMK-2 schematic draw 5.1 yields an area averaged void distribution.

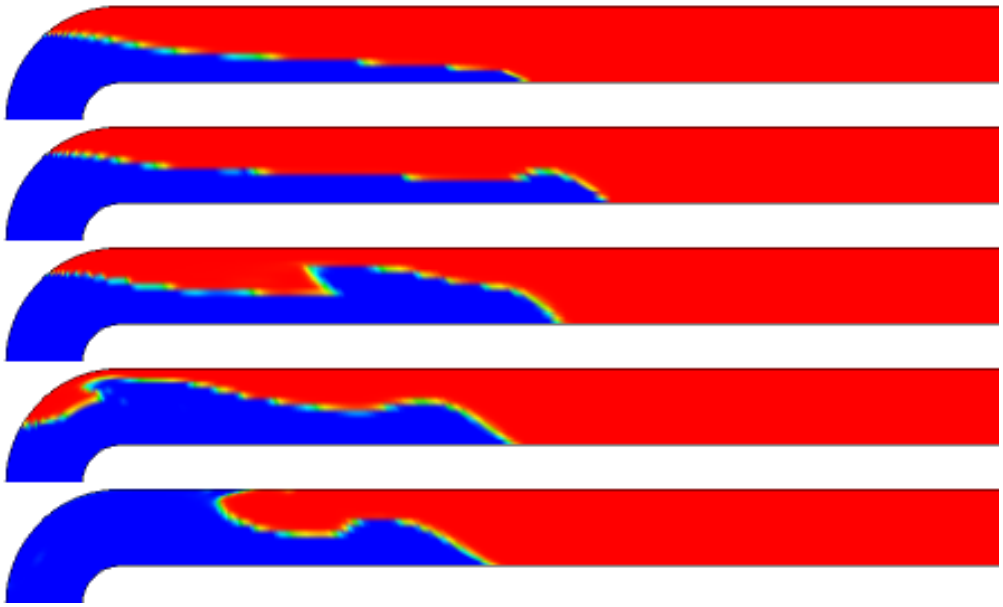

Figure 6.6: Flow pattern in the simulation of the PMK-2 facility with the SRT model based on micro eddies, close to the left bend, at key points in time (5.0 s, 5.5 s, 5.85 s, 5.87 s, 5.88 s, 5.89 s) represented by the void fraction (red: steam, blue: water) [12]

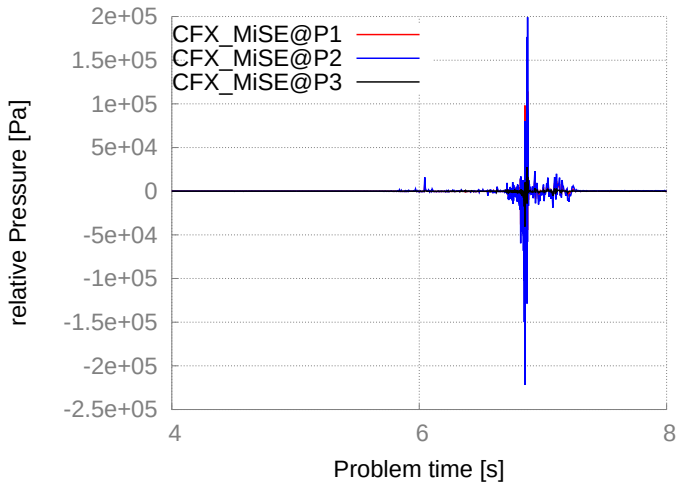

Figure 6.7: Relative System Pressure for the CFD simulation of the PMK-2 facility with HTC model employing micro eddies

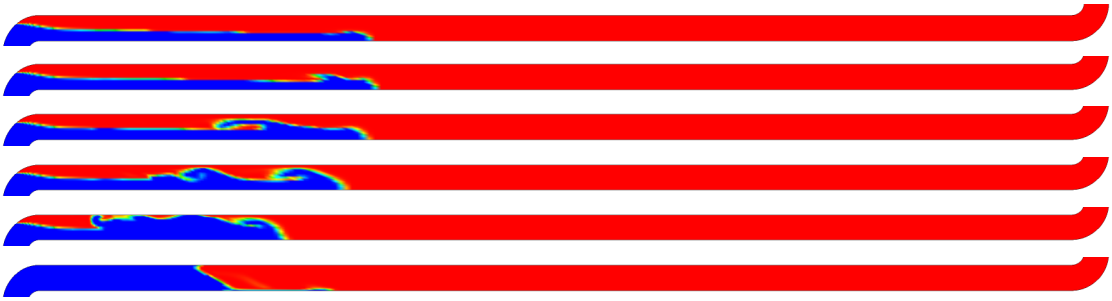

Figure 6.8: Flow pattern in the simulation of the PMK-2 facility with the hybrid SRT model, at key points in time (6.8 s, 7.0 s, 7.2 s, 7.25 s, 7.3 s, 7.5 s) (red: steam, blue: water)

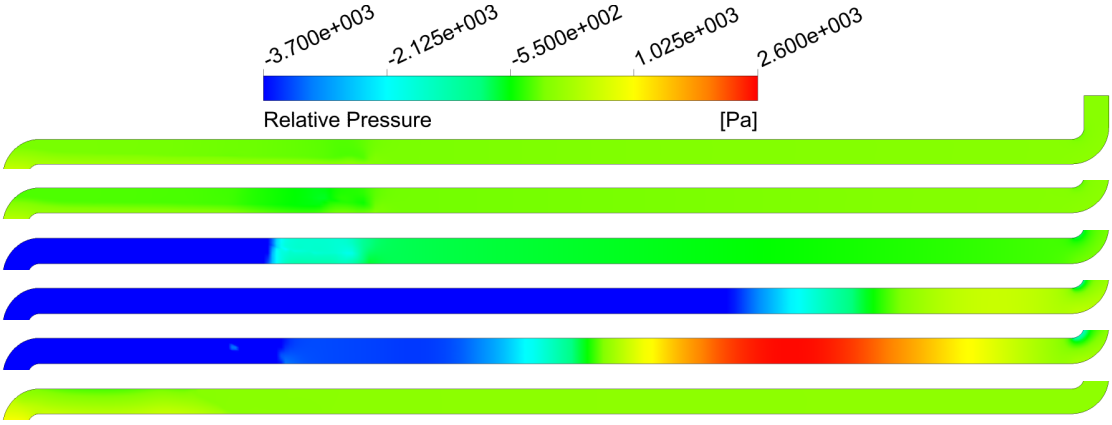

Figure 6.9: Pressure field in the simulation of the PMK-2 facility with the hybrid SRT model, at key points in time (6.8 s, 7.0 s, 7.2 s, 7.25 s, 7.3 s, 7.5 s)

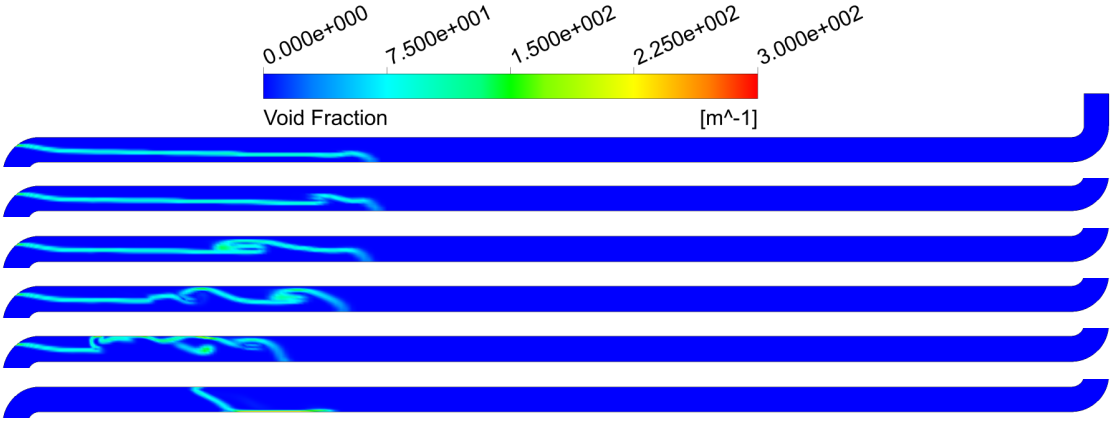

Figure 6.10: IAD field in the simulation of the PMK-2 facility with the hybrid SRT model, at key points in time (6.8 s, 7.0 s, 7.2 s, 7.25 s, 7.3 s, 7.5 s)

When considering the flow patterns of the CFD simulation using the SRT based model which accounts only for the effect of large eddies (the Shen et al. model), it can be observed that both the temperature and void fraction values differ from those measured in the experiment. Nevertheless the flow behavior seems physically reasonable. It can be noticed that there is a certain lag in the decrease of the temperature and void fraction near the point where the measurement probes are located. This is due to the fact that the calculated values for HTC do not lead to the change in the flow pattern from stratified to wavy/slug flow which is required for a fast temperature drop near the measurement probes VT1 to VT4 in figure 6.11. The liquid needs first to reach the bend on the right-hand side of the computational domain before a wavy flow and eventually, a slug is created thus decreasing the temperature and void fraction at the top of the pipe. When only the Shen model is used in the CFD simulation, a smooth decrease of the void fraction can be observed, which leads to the conclusion that the water wave/slug velocity is too small to either condense the steam or to push it away resulting in a sudden void drop as indicated in figure 6.11. The lack of slug acceleration yields a flow without a CIWH event. Analyzing the measured area averaged void fraction as measured by the wire mesh sensor at approximately 9 s, a spike of void is observed. Considering the filling process of the pipe, this increase in the void fraction has to be the cause of a flow reversal triggered by DCC. This effect is not captured in the CFD simulation where the HTC accounts only for macroscopic eddies that can only account for the effect of the larger turbulent eddies on the condensation process.

On the other hand the hybrid model represents the experimental data better than the two individual SRT based HTC models. The timing of the first major slug is predicted reasonably well, as can be observed in the comparison with the measurement data from the WMS shown in figure 6.12 and from the measurement data from all four void fraction probes presented in figure 6.11. The shape of the decrease of the computed void fraction with the hybrid model in the area of the WMS is very similar to the actual measured trend. Even the sudden void fraction increase measured by the WMS around the time point 9 s is predicted by the

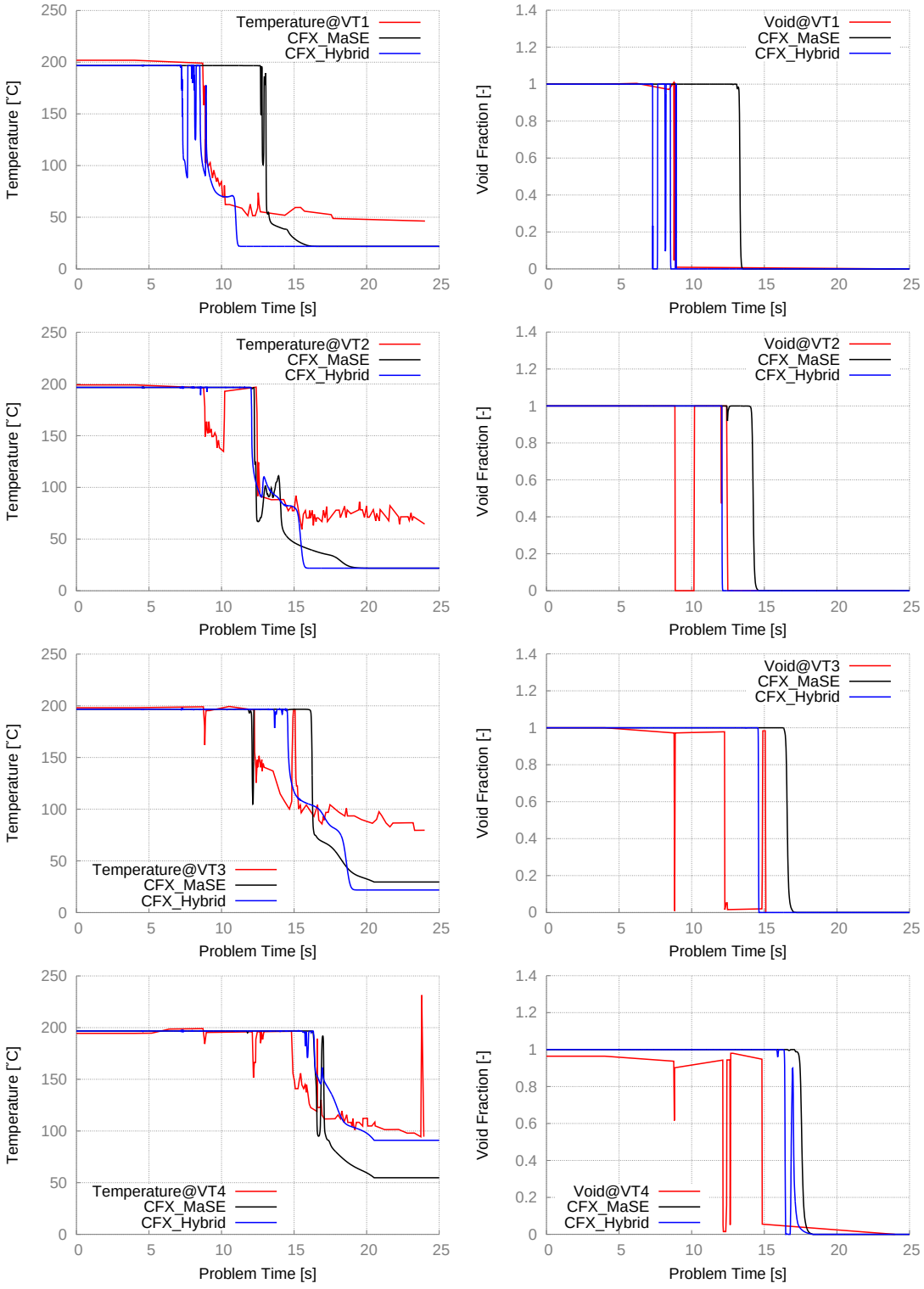

Figure 6.11: Temperature and void at VT1, VT2, VT3 and VT4 of the PMK-2 facility [12]

simulation with the hybrid model. This sudden increase in the void fraction can be explained as a flow reversal, which occurs due to a pressure decrease caused by the increasing condensation rate calculated in the area close to the left-hand bend. This effect is well captured by the CFX simulation with the hybrid HTC model, figure 6.9. The other smaller slugs observed in the experimental data are not entirely captured by the CFD simulation though.

The temperature and void trends of the simulation are similar to those of the probes in the experimental facility for all four void-temperature trends shown in figure 6.11. The lower water temperature predicted at the end of all the CFD simulations compared to the measured values is caused by the imposed adiabatic wall boundary conditions and by the fact that the simulation started with the entire pipe filled with saturated steam, which apparently was not the case in the experiment if judged based on the WMS data shown in figure 6.12. This could be caused by some condensed liquid close to its saturation conditions accumulated at the bottom of the pipe. No information is available about the thin liquid film. The temperature peak seen in VT4 in figure 6.11 is perhaps an overshoot of the temperature probe as the void fraction probe indicates values smaller than 0.1; this high temperature would correspond to superheated steam.

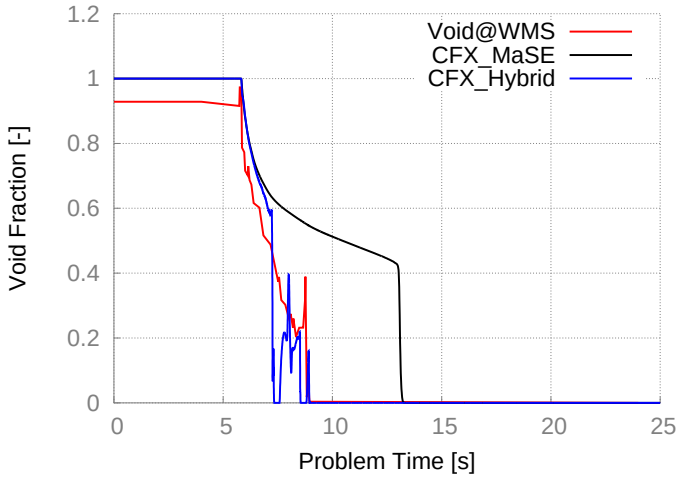

Figure 6.12: Void Fraction at WMS of the PMK-2 facility [12]

Even if the hybrid HTC model could not simulate the pressure increase expected in a CIWH event, it could qualitatively predict well the overall flow behavior and

even local measured quantities such as void fractions and temperatures, proving that the flow behavior was correctly captured by within the simulation. The simulation with the HTC based only on the influence of micro eddies (Hughes and Duffey's model) could predict the formation of a CIWH, still the magnitude of the pressure increase was well below the experimental results. Considering the relatively high local values of the calculated HTC we can conclude that this model can realistically simulate phenomena such as the pressure surges triggered by DCC only if additional effort is spent on the modeling of the IAD, as this quantity appears to be under-predicted by the VOF approach for complex two-phase flows. The value of the condensation rate proportional to the product of the HTC and the IAD strongly depends on the values calculated for these two variables. Even with a large HTC, if the IAD is not accurately computed, the resulting condensation rate will be less than the actual value. Correlations for the HTC such as the one developed in this thesis, can compensate to a certain extent for low IAD values but as the flow becomes more complex and the interface is highly turbulent, they cannot compensate for the large discrepancy between the calculated and the real IAD. For this reason, and based on the analysis of the physical processes that create the CIWH, it has been found that a better prediction of the IAD is necessary to accelerate the vapor bubble collapse and to create the subsequent pressure increase. Another problem observed is the stability of the numerical solution in the CFD codes when large pressure variations take place within very short time intervals, which the current numerical solution methods used by both ANSY-CFX and OpenFOAM appear not to be able to handle in a robust manner.

6.1.2 Simulations of the PMK-2 Experiments with the System Code ATHLET

As system code simulations are still indispensable for the safety assessment of large, complex systems especially over large problem times, continuous development and improvement of such codes is fundamental to achieve better simulation results. Following this work, the hybrid HTC model has been included in the system

code ATHLET, as reported in section 4.2. The objective of this section is to assess the overall performance of the modified system code together with the new DCC module. The results of several ATHLET simulations will be compared in detail with measurements of experiment 05 of the PMK-2 series. Because of the relatively small computation time of the simulation of such an experiment, the entire CIWH experiment-series performed at the PMK-2 facility has been run. A global overview on the experimental matrix is also included in the summary presented in the appendix A. As the system code in its original state was not validated for CIWH events, the following plots will include its results but without any special comments.

The sequence of events in experiment 05 has been introduced in the presentation of the CFD simulations results. A comparison between the standard ATHLET and the modified version will be discussed. The key flow regimes, which appear just before the CIWH, are presented in figure 6.13. Subcooled water enters the test-section forming a stratified flow pattern up to simulation time $7.51s$. After this point, the flow changes in the modified system code computer simulations to wavy and locally a wave evolves to form a slug entrapping a steam bubble. This causes a flow reversal as the steam pocket condenses and accelerates the liquid from right to left towards the location of the injection. After the entrapped steam bubble has completely collapsed, water continues to flow from left to right while other slugs are formed until the test-section is full of water. This flow development was also recognized in the corresponding CFD simulations. In general the time points at which key changes in the flow appear in the simulation with the modified ATHLET do not coincide with those of the CFD simulations.

In order to assess the performance of the newly developed HTC model, the plots showing the temperature, void fraction and pressure will be presented. As only 1-D ATHLET components were available for simulation, only coarse volume-averaged values are computed by the modified system code. When these averaged results are directly compared with local variables as those provided by the void-temperature sensors, some problems arise. The results of the CFX simulations have been post-processed and mapped onto a computational grid similar with that used for the

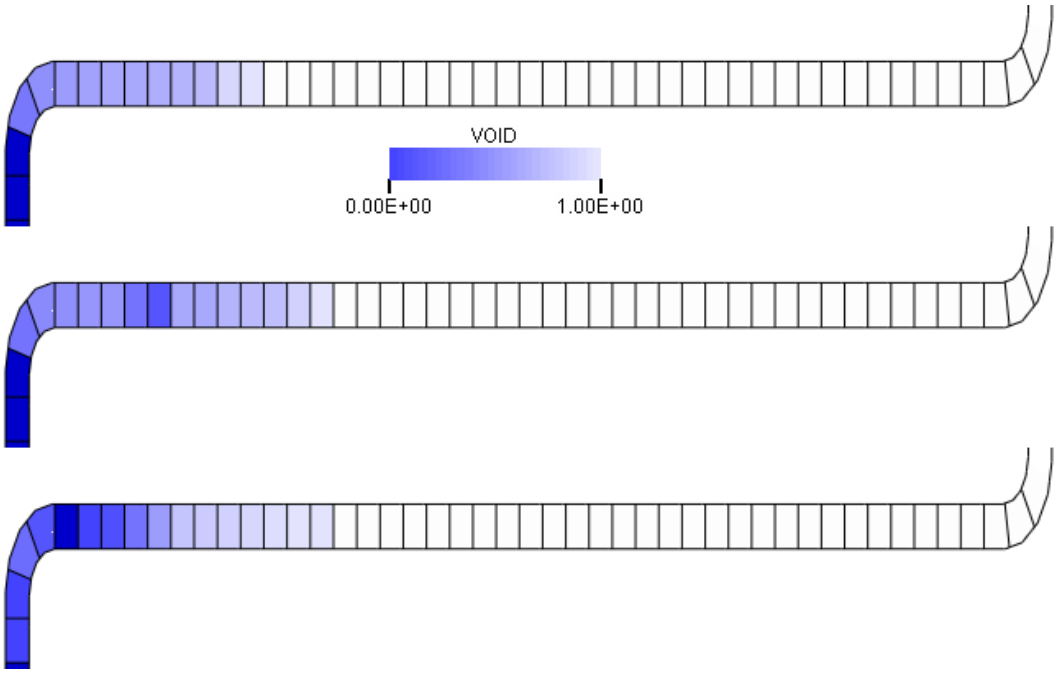

Figure 6.13: Simulated flow patterns in the PMK-2 facility shortly before the CIWH, at 7.0 s, 7.51 s, 7,55 s

ATHLET simulations. This step was performed to better understand the discrepancies between the computed values and the measurement data. The following color convention will be used: *red* will be used to represent the measurement data, the color *blue* for the post-processed CFD results and *black* for those of the modified system code ATHLET, while purple colored curve represents the results of the standard system code (without the new hybrid HTC model). The plots are presented in flow-wise order of the subcooled water traveling through the test-section: first the temperature and void fraction values and at the end those delivered by the pressure transducers. The measurement data obtained with the WMS will also be presented within this section. It has to be considered that a very fine nodalization required to have a fully comparable results with the measurement data of the WMS would violate the nodalization recommendation of system code computational cells. The width to height ratio of a cell is recommended to be greater or at least equal to unity. For a better comparison of the simulation results with the measurement data, a computational cell would be required with a very small ratio

of its width to its height. The effect of additional pressure drop caused by the WMS was not considered. The pipe walls have been modeled as adiabatic BCs; on the one hand to have comparable results with the CFD analysis and on the other hand because no specifications were available about the thermal insulation on the pipe walls, and on the pipe walls themselves. Therefore, the influence of the pipe acting as a heat source was neglected.

Figure 6.14 presents the calculated and simulated temperature and the void fraction trends. Even if it appears to be a systematic error as the temperature and void curves decrease faster than in the experiment, considering the properties of 1D simulations and using the post-processed CFD results, the reason for it is explainable. Bearing in mind the following three factors: *(i)* the location of the sensors, i.e. at the top of the pipe, *(ii)* the system code's variable storing location for temperature, void fraction and pressure, i.e at the cell center and *(iii)* the one-dimensional flow description, a faster temperature decrease is more than logically predicted in a Control Volume (CV) by the system code. As soon as subcooled water enters a CV, the volume averaged value of the void fraction in that cell decreases unlike in the experiment where water has to first reach the exact location of the void probe before a decrease is recorded. Considering that the computational grid only offers a single dimension for the flow to develop, it is expected that a local complex interface morphology mainly caused by rapid turbulence induced condensation, will not be captured by the system code. This leads to a smoother transition in the system code simulated curve trends than those resulting from the post-processing of CFD results and those measured.

A detailed analysis of the results displayed in figure 6.14 at location VT1 where both temperature and void fraction are simultaneously measured, shows that the temperature computed by the modified ATHLET is similar to the post-processed value offered by the ANSYS CFX simulation and both are in good agreement with the experimental data. The 2-D effect caused by the different temperature layers is not captured by ATHLET as expected. The evolution of the void fraction close to the first sensor is almost identical between the modified system code and ANSYS CFX. It is expected that in the vicinity of the first sensor, both the modified

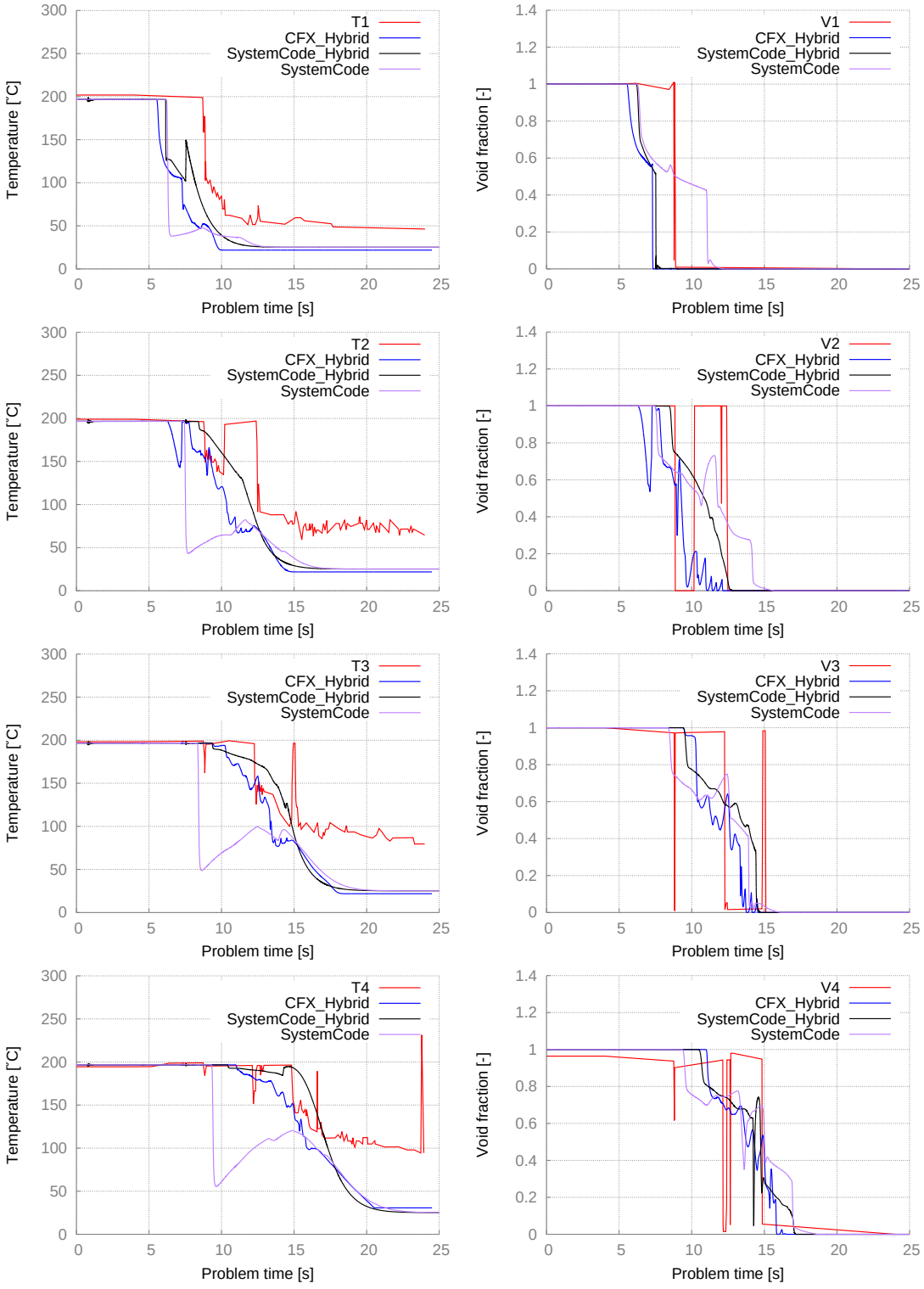

Figure 6.14: Temperature and void fraction at VT1, VT2, VT3 and VT4 of the PMK-2 facility [12]

system code and CFX predictions display a similar behavior. Thus, in the pipe segments *before* the left elbow a stratified vertical flow appears, whereas in the horizontal test-section, as the IAD increases with the inflow of subcooled water, a multidimensional flow pattern develops.
With the data provided by the sensor VT2, some differences are noticed between the results of the computer codes used. The modified system code predicts very well the onset of the slug flow, which is recorded by the sensor at around 9 s and by ANSYS CFX at around 6 s. A rather smooth transition from steam to subcooled water is predicted close to VT2 and VT3. The two-phase flow dynamics close to VT4 is again well predicted if compared with the post-processed CFD results. Slugs traveling through the pipe can be observed following the interpretation of the void fraction computed at this location. In general both codes capture a similar dynamic behavior of the two-phase flow in the test-section. In both cases a slug travels through the pipe, which is accelerated toward the left bend as a result of the high steam condensation rate. According to the experimental data, the slug travels past VT4 at approximately 13 s problem time whereas in both simulations this slug is predicted to reach that sensor between the time-points 14 s and 15 s. The relatively lower temperatures observed towards the end of the computer simulations are caused by the simplifications of assuming adiabatic pipe walls and by the location of the temperature sensors mounted at the top of the pipe, while the results are presented as volume averaged values over the entire pipe cross section. During the analyzed experiment 05, a CIWH phenomenon was recorded by the pressure transducers. The highest recorded pressure peak was at around 150 bar, corresponding to a tenfold increase in nominal pressure considering the initial 14.5 bar. Comparing the predicted void fraction at the location of the WMS, it can be noticed that even if the overall flow patterns are simulated correctly, the time predictions do not overlap between the modified system code results and the measurement data. In the experiment a slug is recorded to travel past the WMS at approximately 9 s, while the modified system code predicts this slug earlier. This over-anticipation of the time-point of the slugging onset, affects the evolution of the pressure in the test-section. The pressure predicted at the locations of the

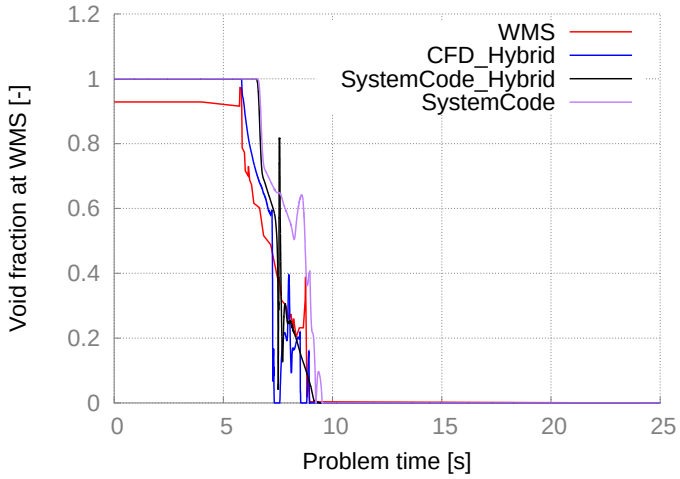

Figure 6.15: Void Fraction at WMS of the PMK-2 facility [12]

three transducers was lower than in the experiment. Still if the stochastic effect of the occurrence of CIWH is considered, a prediction of the highest peak close to that of the measurement data for one single run of the experiment is satisfactory. The predicted value is around 112 *bar* compared to the measured 156 *bar*. The highly stochastic nature of CIWH was confirmed at the PMK-2 experimental facility by performing the same experiment twice. In the first run, a 100 *bar* pressure peak was measured while in the second run a 210 *bar* peak was recorded [68]. An additional cause that can explain this discrepancy is the value of the time points at which this event occurs in the simulation and in the experiment. As discussed in section 2.4.1, the sequence of the phenomenon of CIWH includes a flow pattern change from horizontal to slug flow, with a large steam bubble entrapment. The sudden condensation of this large steam pocket accelerates the water surfaces that delimitate the steam pocket against each other or toward the pipe wall and a pressure surge emerges as momentum energy is transformed into pressure energy. In the case of the modified system code simulations, in which the pressure peak occurs some 1.5 *s* earlier than in the experiment, a smaller liquid inventory is available in the horizontal test-section. Considering the massflow rate of approx. 1 kg/s, as measured in the experiment, this would lead to approx. 1.5 kg *less* of subcooled water injected into the test-section if compared to the experiment. Consequently, a smaller steam pocket can be entrapped by the available subcooled

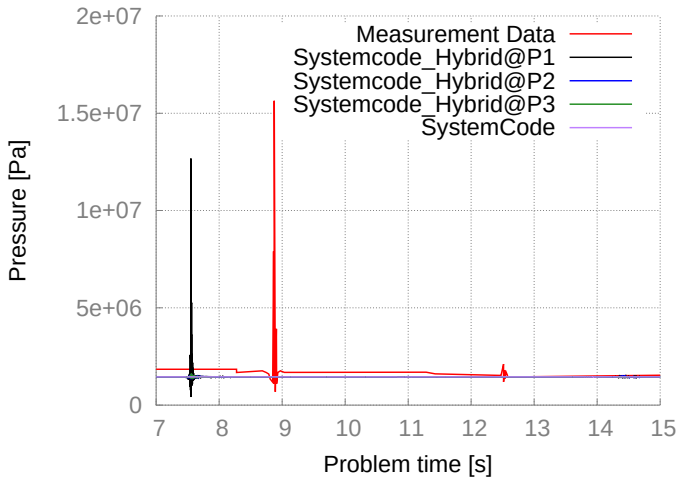

Figure 6.16: System Pressure of the PMK-2 facility

liquid because the resulting *tongue* of liquid is shorter in the simulation than in the experiment. The steam bubble collapse is explicitly the driving force for the water front acceleration leading to the CIWH; smaller bubbles deliver less acceleration and less momentum to the liquid thus resulting in lower pressure peaks.
A summary of the sensitivity study of the height of the pressure peak in the resulting CIWH is presented in figure 6.17. The study considers the influence of the turbulence, the flow regime, the condensation potential and the density differences between the two phases. The plots contain the measured data of the entire PMK-2 experimental series and the simulation results of the modified ATHLET. Additional simulations with Re $\approx 20,000$ have also been performed in order to have a better result resolution for the flows around this value of the Reynolds number. Because of the transient character of all experiments, the evaluation of the non-dimensional numbers used in the analysis has been performed for the initial conditions and used in the horizontal axis of the plots; the vertical axis is always the pressure increase ratio, i.e. the ratio of maximum pressure to the initial system pressure.

At first the influence of turbulence is analyzed, expressed based on the liquid side Re number. The highest pressure increase ratios are clustered in the interval 20,000 $<$ Re $<$ 40,000. Considering the relationship between the Re and the Fr

Effect	**Dimensionless Number**	**Implications in the flow dynamics**
Turbulence	Re	Enhances the heat and mass transfer
Flow regime	Fr	Subcritical liquid flow enhances the chances of slugging onset
Condensation potential	Ja	High condensation potentials can act as the onset to slugging
Density differences	At	High density ratio between the phases amplifies the magnitude of CIWH

Table 6.1: Considered dimensionless numbers used in the interpretation of the experimental results

number, the given geometry and the thermo-physical properties of water for the given system conditions, the maximum pressure increase ratios correspond to a Fr number around the value of 0.3. This can also be noticed from the plot presenting the maximum amplitude of CIWH as a function of the Fr number, figure 6.17. As a conclusion it can be remarked that an optimum value of turbulence and a specific flow pattern have to coexist in order to generate CIWH events. As expected the condensation potential given by the Ja number, directly influences both the occurrence probability of CIWH and the pressure increase ratio. This is due to its direct link with the condensation rate, which by itself has been proven to be able to change the flow pattern from stratified to slug flow, based on the interpretation of CFD simulations of this facility, chapter 6.1.1. The high density ratio between the two phases is also an important factor influencing the CIWH magnitude as water has to fill the space of the condensed vapor. For low system pressure, the At number tends to unity, resulting in very high density ratio and correspondingly in high pressure values of the CIWH. The fact that for lower At numbers, simultaneously both the number of CIWH events and their magnitude abruptly drop to zero, underlines the prediction that facilities operating at low system pressures are more prone to CIWH incidents than facilities operating at high system pressure,

where the densities of the phases tend to the similar order of magnitude. This is a logical consequence of the fact that at low system pressure, the higher differences between the densities leads to higher acceleration of the liquid side in the case of DCC. It has to be considered that even a high increase rate of a low initial pressure might not be as dangerous for a plant equipment as a smaller increase rate of a high initial pressure. Nevertheless, a low initial system pressure increases the probability of CIWH events.

The intensity plots depicted in figure 6.18 represents the combined effects of the turbulence and the condensation potential as the driving forces for CIWH events. It can be highlighted that the plots, showing both experimental data and the simulations' results with the modified ATHLET exhibit a maximum pressure increase ratio around Re $\approx 20,000$, with a clear influence from the Ja number. For smaller values of Re, almost no CIWH events are measured or simulated. Around Re $\approx 90,000$, both in the simulations and the measurement data, no CIWH were recorded. The region in the interval 90,000 $<$ Re $<$ 120,000, is again prone to CIWH. A consistent behavior is observed between the simulation results and the experimental data based on the concomitant influence of the turbulence and the flow character on both the occurrence of CIWH and the pressure surge magnitude, figure 6.19.

This sensitivity study shows that the simulations are influenced in the same manner by the key parameters responsible for the magnitude of CIWH and their occurrence as the experiments. As a result it can be concluded that the newly implemented hybrid, mechanistic, HTC model clearly improves the overall prediction capabilities of CIWH events, with the system code ATHLET without the need of any parameter tuning.
To remove the limitations of a typical $1D$ simulation in ATHLET, a more detailed modeling network has been set up in such a way that the development of 2D flow patterns can be simulated using only 1D components. The standard ATHLET in its Version 2.2 Cycle A offers the possibility to use cross connection objects, which

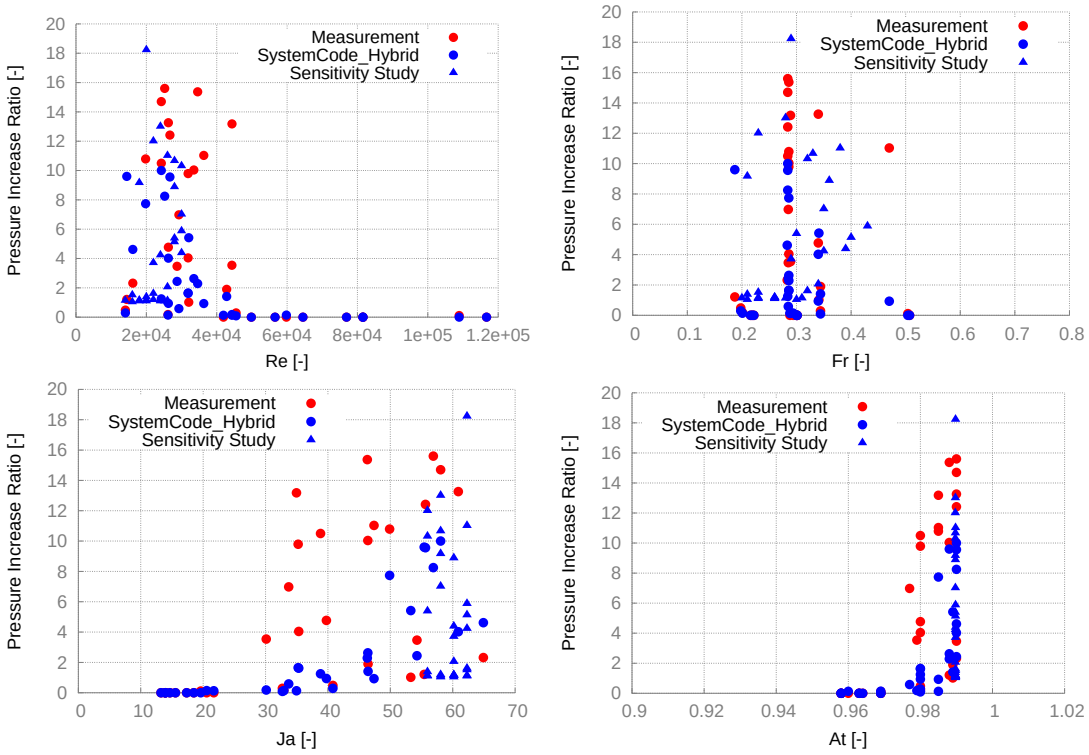

Figure 6.17: Pressure Increase Ratio as a function of the Re, Fr, Ja and At numbers

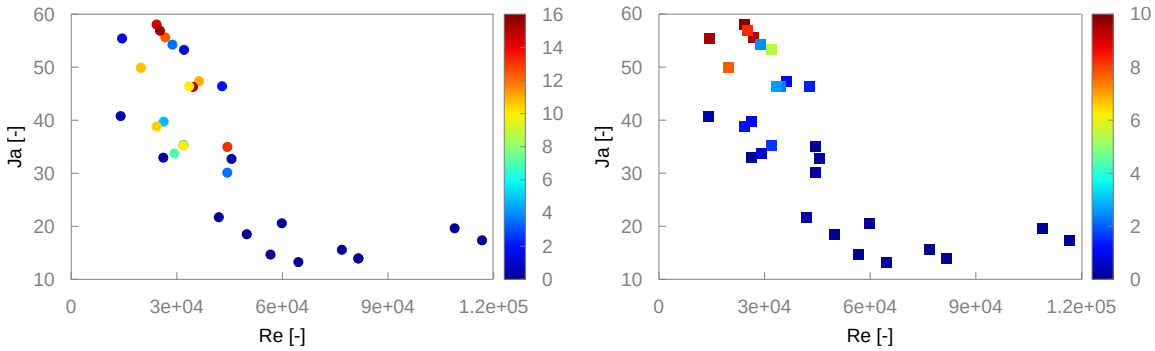

Figure 6.18: Pressure Increase Ratio as a function of the Re and Ja numbers

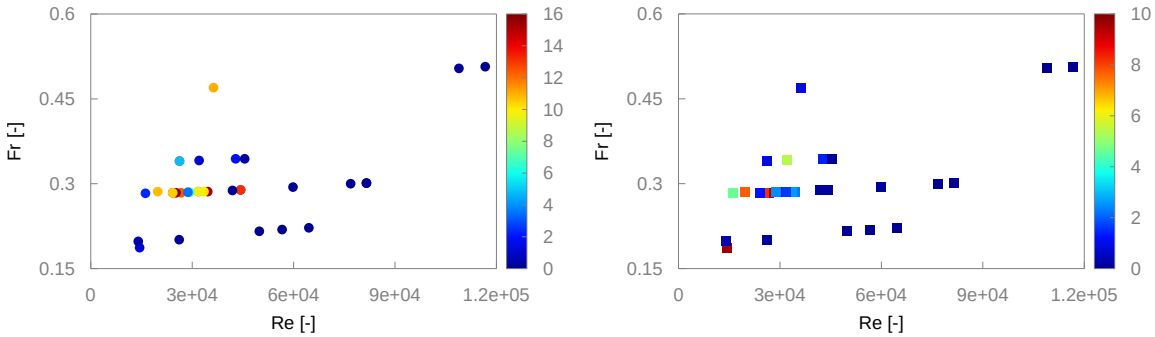

Figure 6.19: Pressure Increase Ratio as a function of the Re and Fr numbers

represent a series of parallel junctions between the modeled pipes segments. Using this feature originally developed for the simulation of the vertical parallel flow channels in components of a nuclear Reactor Pressure Vessel (RPV) together with a proper arrangement of the pipe segments, allows for the simulation of quasi-$2D$ flow regimes. The cross connection objects in ATHLET include so-called single junctions which, unlike standard CV, do not contain an inventory of energy or mass [49]. As a second dimension is offered for the flow development, a complex flow pattern can appear due to a local pressure decrease caused by high condensation rates.

A schematic representation of a horizontal pipe segment using this approach is presented in figure 6.20. This figure shows an exploded view of the three pipe segments and the adjacent branch needed for the representation of the original pipe. The horizontal test-section has been divided in the three individual pipes placed one on top of the others. This arrangement was chosen in order to have a relatively good spacial resolution of the results and still keep computational power low. Special attention was given to the design phase of this model to preserve the hydraulic properties of the initial flow channel. The three pipes called: *TESTSECTO*, *TESTSECTM*, *TESTSECTU* represent the upper, the middle and the lower parts of the pipe section. The middle pipe is interconnected with the upper segment by the cross-connection object *CCOMO* and with the lower one by *CCOUM*.

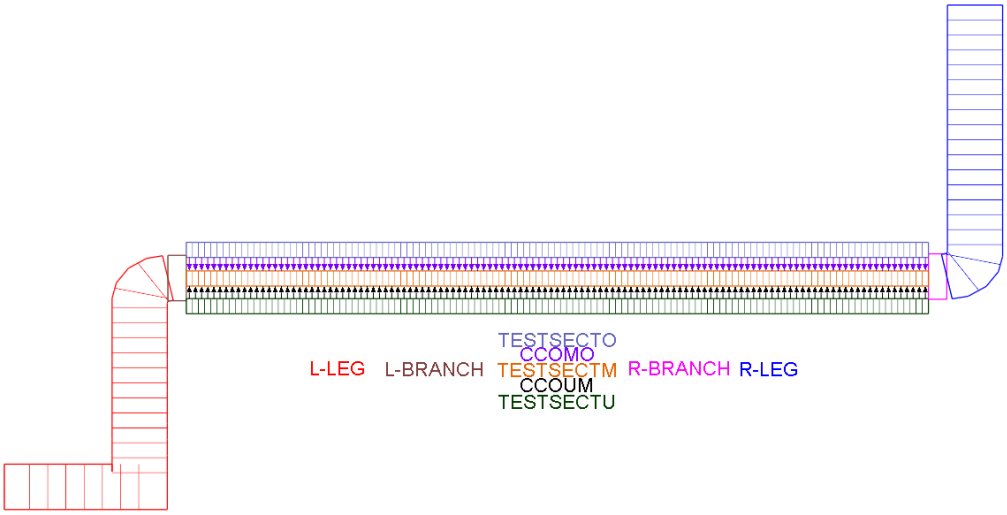

Figure 6.20: Pipe network of the PMK-2 model for the simulation of quasi-2D flow regimes with ATHLET [12]

This simulation technique could however not be entirely successfully used because the flow regime maps, currently implemented in ATHLET-2.2 Cycle A do not consider such a configuration of pipe-components. Additional code development is required to successfully use such a configuration for complex flow patterns in horizontal or nearly horizontal flow configurations. Still the potential of improving the results thanks to a pseudo-two-dimensional description of the computational domain for the simulation of complex flow patterns such as wavy and slug flow is high.

6.2 CFD Simulations of the TUHH Experimental Facility

For the validation of the newly developed HTC model, three characteristic experiments performed at the facility constructed and operated at TUHH have been chosen. The volumetric flow rate of the injected subcooled water was implemented as a BC into the CFD simulations carried out with the OpenFOAM code. No ANSYS CFX simulations have been performed because of license limitations, limitations which do not apply to OpenFOAM.
Three of the TUHH experimental series were selected for the assessment of the hybrid HTC model implemented into a VOF based CFD code. Experiment Fr03T40 corresponds to a maximum Froude number of approximately 0.3 and a water subcooling of 40 K; experiment Fr06T40 corresponds to a maximum Fr number of approximately 0.6 and a subcooling of 40 K; and experiment Fr06T60 corresponds to a maximum Froude number of approximately 0.6 and a water subcooling of 60 K. These particular experiments were selected for the assessment of the new HTC model because different flow characteristics emerge based on the imposed BCs. In the first experiment the flow is controlled by a small volumetric flow rate of the subcooled water. In the second experiment the corresponding Fr number is doubled compared to the first experiment, while the water subcooling is kept constant. This second experiment should underline the effect of the flow rate on the two-phase flow dynamics. The last experiment should highlight the influence of high water subcooling and high turbulence induced by the high water flow rate. The three different curves corresponding to the pump starting process for each of the experiments considered are presented in figure 6.21 and used as BC for the simulations.

The selected experiments were conducted with the facility having a slope of 1.4° with respect to the horizontal axis. This means that the right separator was situated slightly higher than the left one, thus favoring the flow of subcooled water from the injection location towards the left separator.

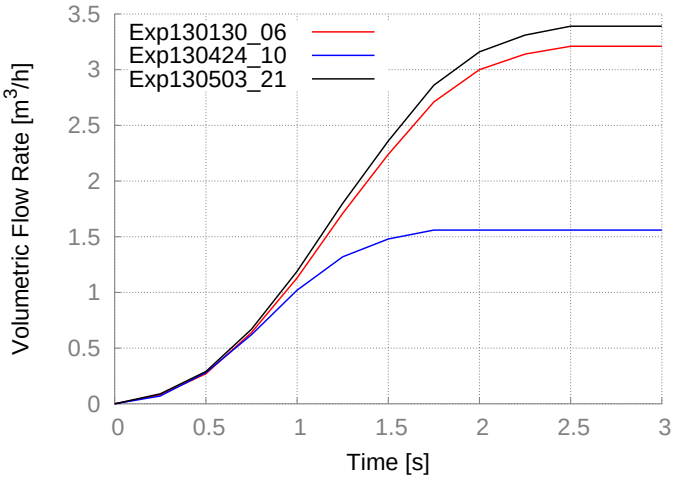

Figure 6.21: Volumetric flow rates of three characteristic experiments conducted at the TUHH experimental facility

The assessment procedure is as follows: first the influence of the volumetric flow rate on the flow pattern evolution is analyzed then the influence of the subcooling is analyzed. This particular sequence for the presentation of the CFD results was chosen, in order to study the sensitivity of the horizontal or nearly horizontal two-phase flow dynamics to the heat and mass transfer driven by the flow turbulence and the water subcooling.

In all cases, the flow patterns are identified in the CFD simulations first followed by a direct comparison of flow variables against the measured data. In order to better understand the simulation results and to interpret the comparison, one has to keep in mind the stochastic character of the onset of CIWH and the deterministic results of a computer simulation.

6.2.1 CFD Simulation of the TUHH Experiment Fr03T40

The presentation of the TUHH simulation results begins with the experiment Fr03T40, in which the lowest volumetric rate of subcooled water was injected into the test-section. During this experiment a maximum volumetric flow rate corresponding to a maximum Fr number of approximately 0.3 was reached. The liquid has the lowest subcooling of all experiments, namely 40 K.

Because of the low flow rate injected, a low turbulence intensity in the flow is expected which, together with the low subcooling of the liquid, leads to relatively low condensation rates. From the evaluation of the developed flow patterns shown in figures 6.22 to 6.25, the scenario of this simulation can be summarized as follows: the injected subcooled liquid rises vertically in the T-junction and hits the upper part of the test-section pipe by the time the maximum flow rate corresponding to Fr=0.3 is reached. The water then flows around the pipe wall towards its bottom predominantly to the left end of the injection point. The test-section has a 1.4° slope and the mass flow rate is not enough for the liquid to flow towards the separator located to the right of the injection.
A liquid layer forms at the bottom of the pipe as water in continuously injected into the test-section. This can be seen in the void fraction values at the pipe's cross-sections where the thermo-couples are mounted as displayed in figure 6.23. At approximately 4.10 s, a wave builds up almost halfway between the thermo-couples T4 and T3 due to locally increasing condensation rates caused by an increasing local HTC. Figure 6.31 and the associated local decrease in the local pressure shown in figure 6.27 reflect this behavior. The water wave continues to grow driven by direct contact condensation and a steam pocket starts being isolated as can be seen in figure 6.24 showing the void fraction close to the location of T4. The complex interface morphology of a breaking water wave can also be observed in figure 6.24. It is obvious how the crest of the wave rolls back into the liquid bulk, by regarding the evolution of void fraction field. This can be observed by focusing on the region close to the pipe's central axis, where a light blue colored region is noticed above the dark blue region of the bulk of subcooled water.

The region above the bulk, the transition from blue to red colors, is the 'smeared' interfacial area between the entrapped steam bubbles and the subcooled water. In the steam region the void fraction does not correspond to pure steam but to steam with small entrapped droplets of water. A significant water drop is even expelled from the wave and projected against the top of the pipe, the light blue region close to the pipe wall in the same picture.
A later decrease in the local HTC coefficients reduces the counter-flow water wave acceleration as shown in figure 6.33 and also noticed from the observation of the relative pressure field in figure 6.29. After the water wave gradually disappears, stratified flow formation is observed from the T-junction towards the left-side separator with a continuous generation and decay of small water waves due to an increased local direct contact condensation phenomenon. Still the flow never fully transforms into slug flow in the more than 10 s of experiment simulated.

The analysis of the results above reinforces the conclusion reached in the simulations of the PMK-2 experiment in section 6.1.1, where it was noticed that the high condensation rates can act independently as the driving force for flow pattern changes.

The IAD shows higher values especially in the regions where water splashes against the pipe wall close to the T-junction injection, or where a very thin liquid layer exists. This is the case of the water front flowing towards the left side of the test-section. The combined influence of the increased IAD and HTC trigger the flow pattern change. The comparison of the eight measured temperature trends against the simulated ones reveals a good overall prediction of the temperature distribution by the CFD simulation as shown in figure 6.38. The subcooled water flows past the four instrumented locations from T4 to T1. The constant pressure boundary condition and the *idealized* concept of open boundaries at the left and right extremes of the computational domain offer an *'unlimited'* steam inventory to be sucked by the reduction in pressure caused by the condensation. In the experiment the steam inventory is certainly limited. As continuous steam condensation

causes a pressure decrease, a continuous decrease of the saturation temperature is observed. Therefore, this effect could not be considered in the CFD simulations and the saturation temperature is kept constant and linked to the constant boundary pressure.

Comparing the trends of the curves Tf4 and Tg4, it can be concluded that the flow pattern produced by the computer simulations represents the experimentally observed two-phase flow dynamics satisfactorily. The time points at which the temperatures decrease marking the passing of subcooled water coincide well in the simulation and the experiment. The flow pattern close to T3 however, differs between the simulation and the experiment. The time at which the first temperature decrease occurs is predicted well by the simulation at this location but afterward because of the high condensation rates, the direction of the advancing liquid film is reversed towards the injection point. An increase of the temperature is then predicted, as saturated steam replaces subcooled water. The discrepancy between simulation results and measured data close to the left boundary of the computational domain is partially influenced by the open boundary condition employed. Nevertheless the simulations show a similar behavior to that inferred from the analyzed experimental data. The converging curves for Tf and Tg near the end of the simulation suggest that the test section is filled with water at this time. However the analysis of the measured temperature evolution leads to the conclusion that the test section was never completely filled with subcooled water.

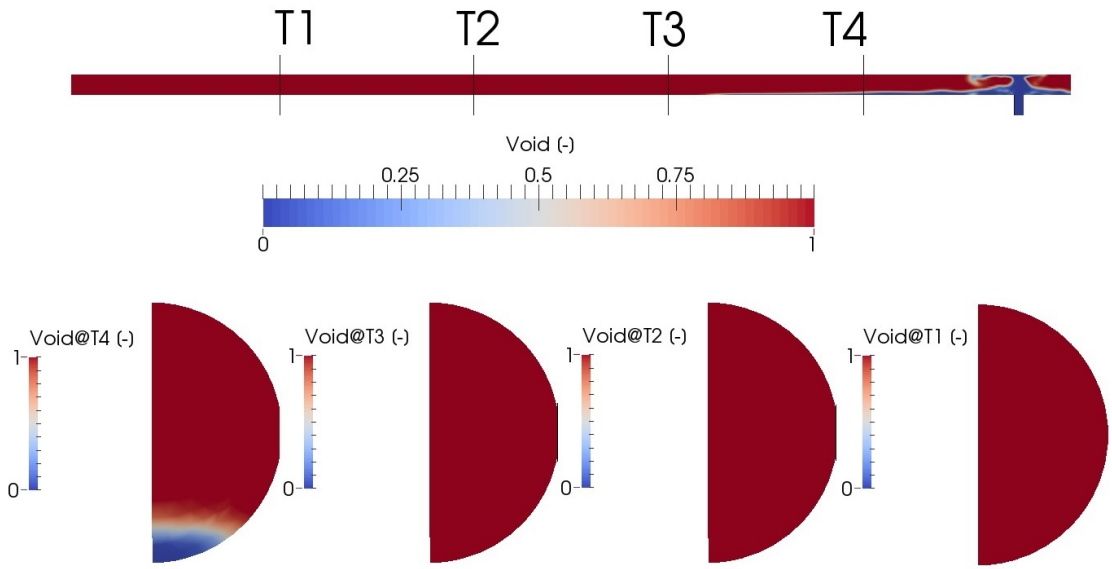

Figure 6.22: CFD results of the fully developed 'water fountain' at problem time 1.70 s, TUHH experiment Fr03T40

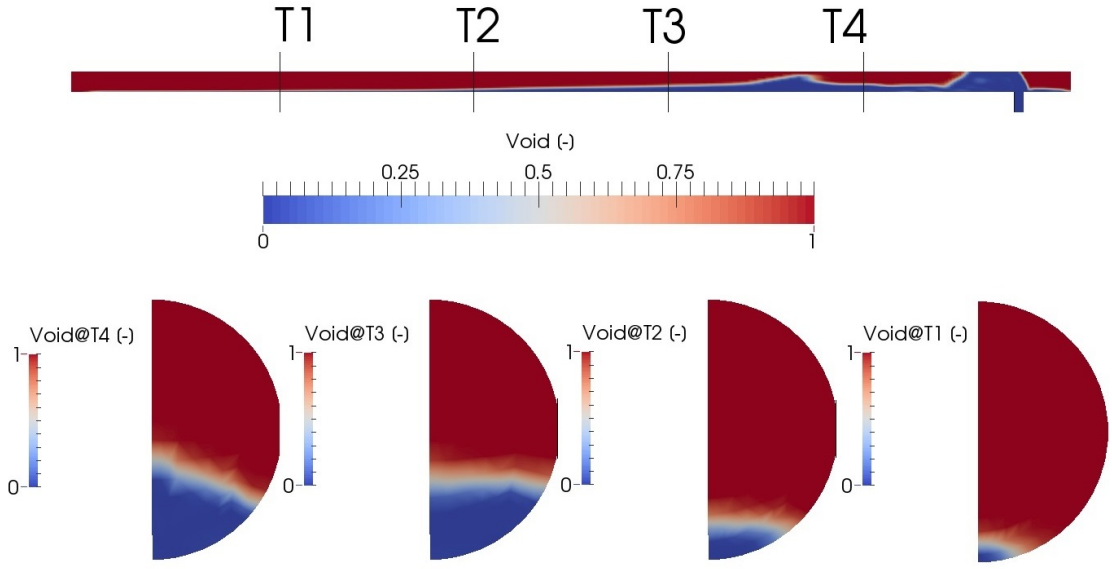

Figure 6.23: CFD results of the transition from horizontal to wavy flow at problem time 4.10 s, TUHH experiment Fr03T40

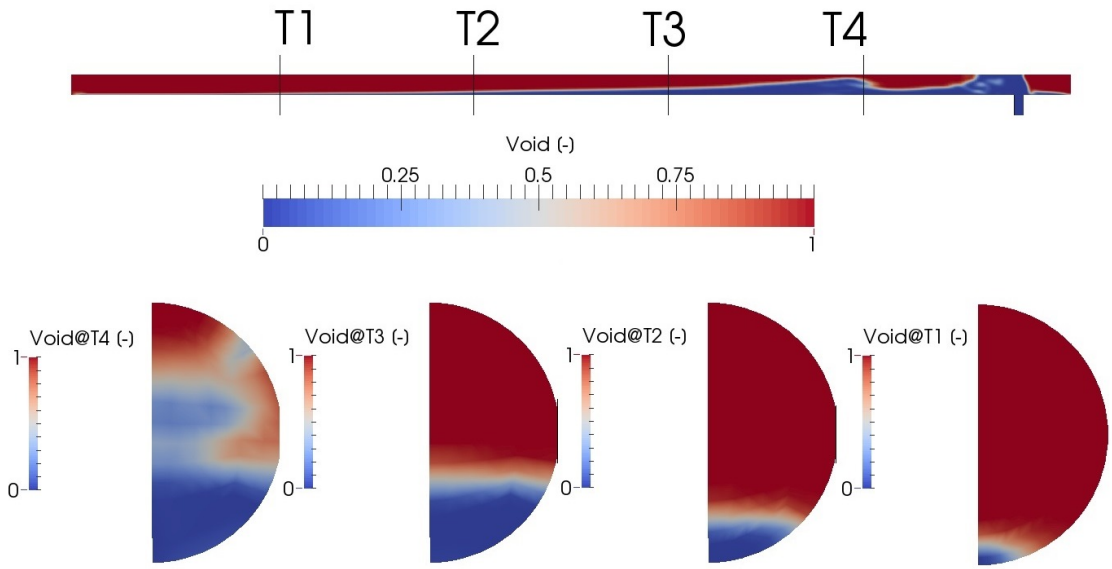

Figure 6.24: CFD results of the water wave growing to form a slug at problem time 4.45 s, TUHH experiment Fr03T40

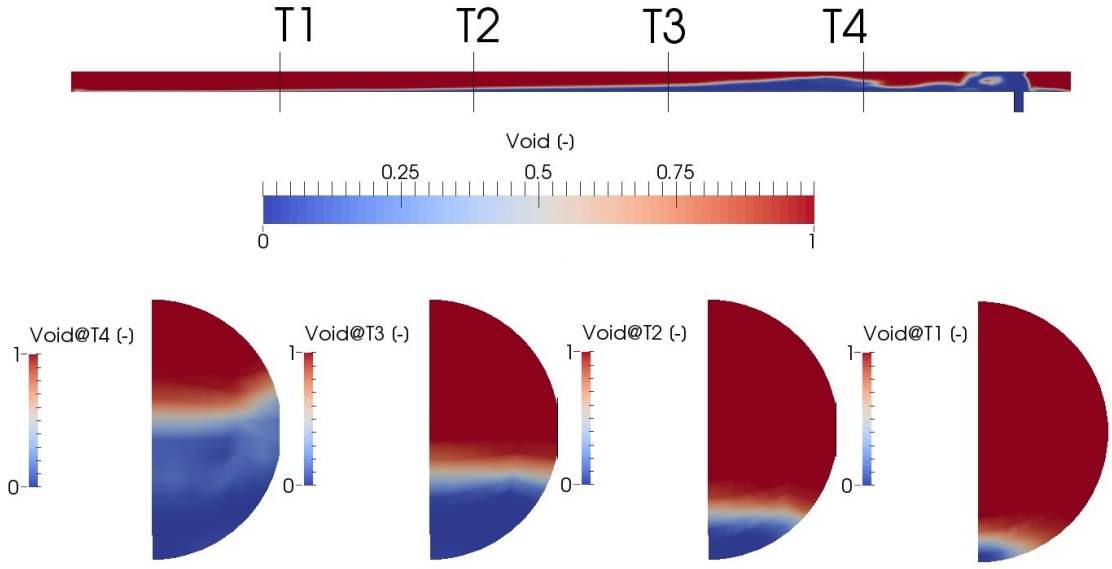

Figure 6.25: CFD results of the decay of the water wave at problem time 4.55 s, TUHH experiment Fr03T40

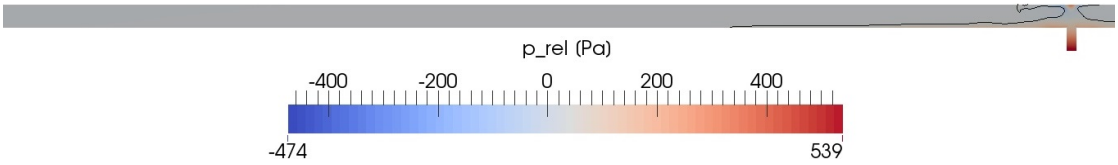

Figure 6.26: CFD results of the relative pressure field with 0.5 void fraction contour line at problem time 1,70 s, TUHH experiment Fr03T40

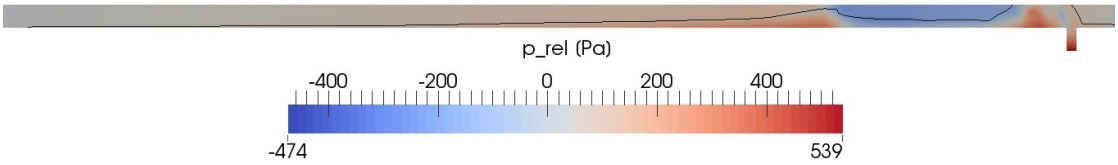

Figure 6.27: CFD results of the relative pressure field with 0.5 void fraction contour line at problem time 4.10 s, TUHH experiment Fr03T40

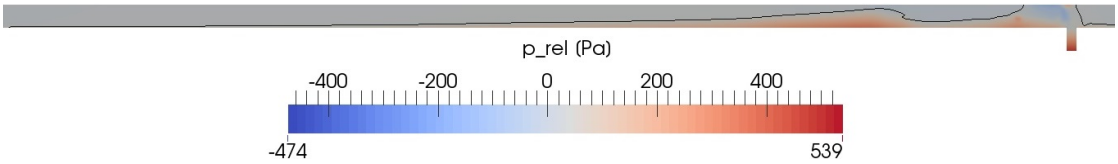

Figure 6.28: CFD results of the relative pressure field with 0.5 void fraction contour line at problem time 4.45 s, TUHH experiment Fr03T40

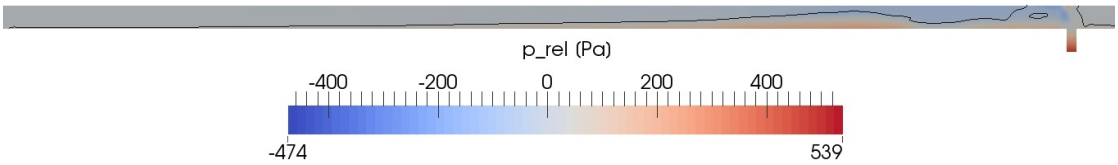

Figure 6.29: CFD results of the relative pressure field with 0.5 void fraction contour line at problem time 4.55 s, TUHH experiment Fr03T40

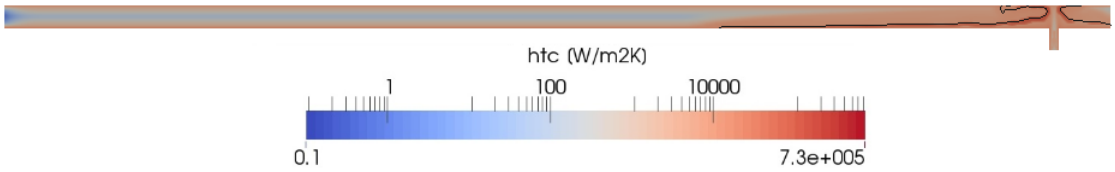

Figure 6.30: CFD results of the HTC field with 0.5 void fraction contour line at problem time 1.70 s, TUHH experiment Fr03T40

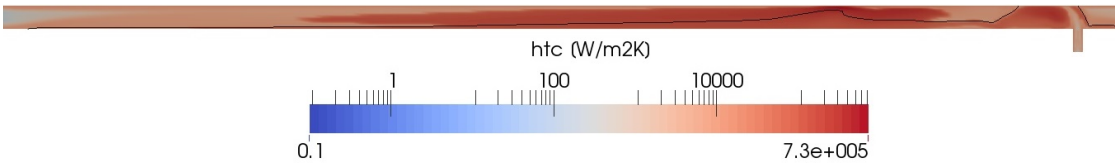

Figure 6.31: CFD results of the HTC field with 0.5 void fraction contour line at problem time 4.10 s, TUHH experiment Fr03T40

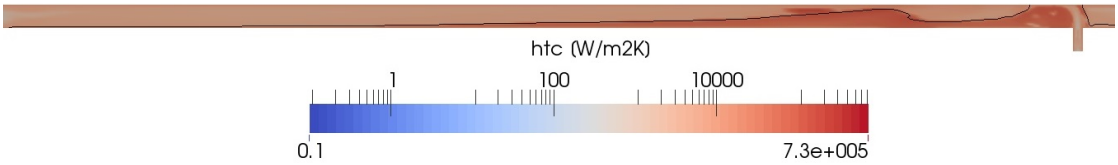

Figure 6.32: CFD results of the HTC field with 0.5 void fraction contour line at problem time 4.45 s, TUHH experiment Fr03T40

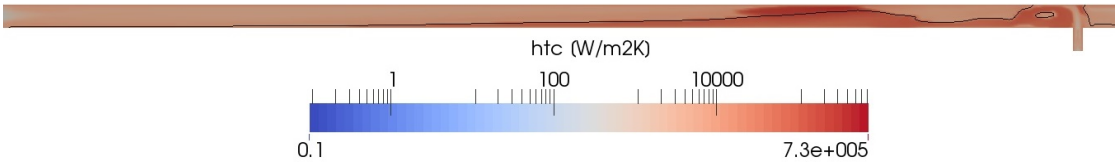

Figure 6.33: CFD results of the HTC field with 0.5 void fraction contour line at problem time 4.55 s, TUHH experiment Fr03T40

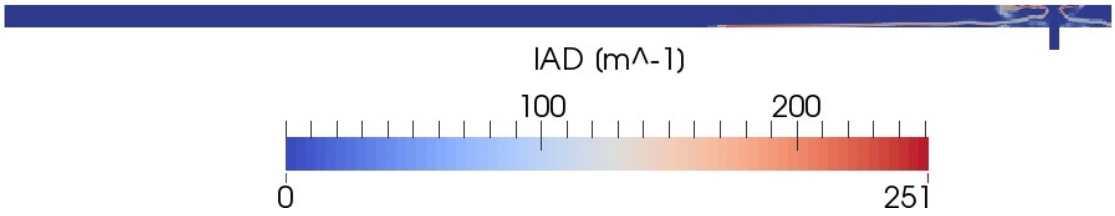

Figure 6.34: CFD results of the fully developed 'water fountain' at problem time 1.70 s, TUHH experiment Fr03T40

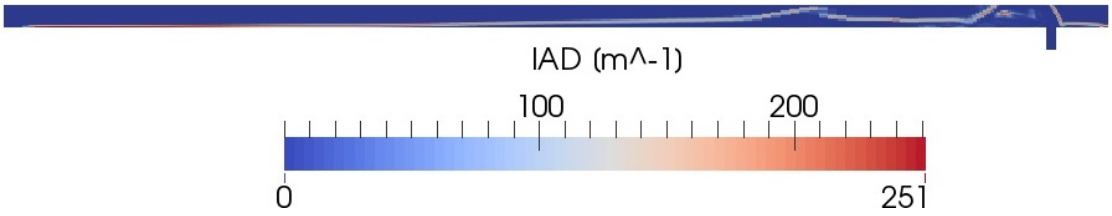

Figure 6.35: CFD results of the transition from horizontal to wavy flow at problem time 4.10 s, TUHH experiment Fr03T40

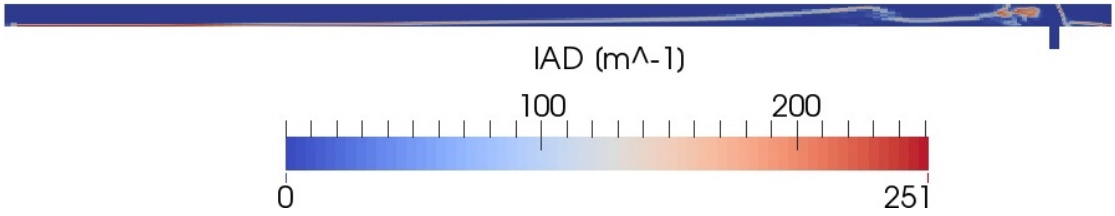

Figure 6.36: CFD results of the water wave growing to form a slug at problem time 4.45 s, TUHH experiment Fr03T40

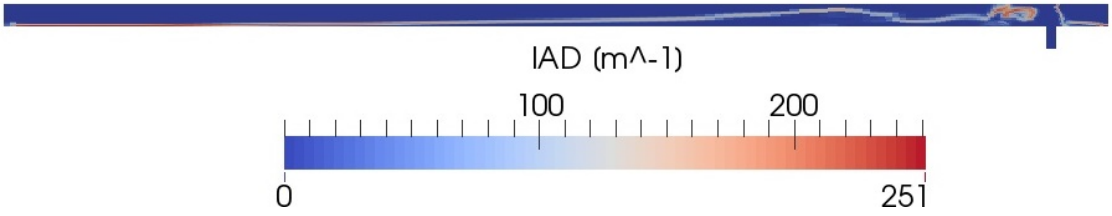

Figure 6.37: CFD results of the decay of the water wave at problem time 4.55 s, TUHH experiment Fr03T40

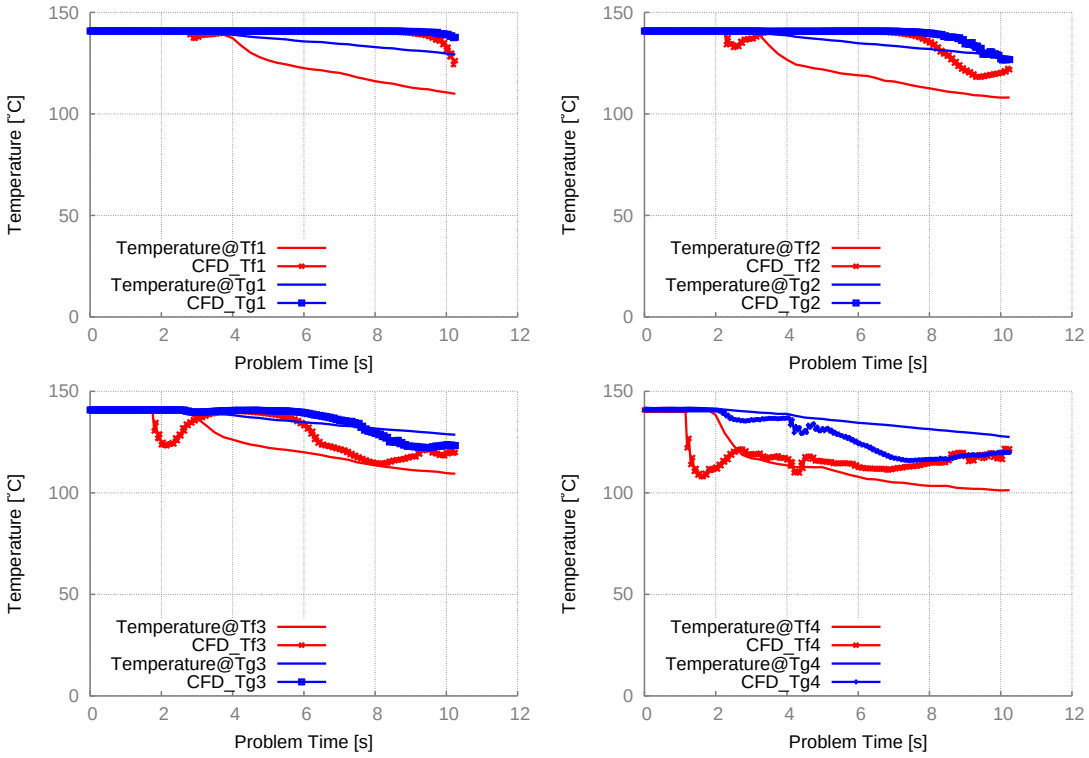

Figure 6.38: CFD results of the temperature at the thermo-couples Tf and Tg, TUHH experiment Fr03T40

6.2.2 CFD Simulation of the TUHH Experiment Fr06T40

During this experiment a maximum Fr number of 0.6 was reached while keeping the water subcooling at the low value of 40 K. The increase in the maximum flow rate delivered by the pump with the same subcooling as in the previously analyzed experiment Fr03T40, should only highlight the influence of a larger turbulence on the direct contact condensation phenomenon and on the two-phase flow dynamics. The simulation results allow for an explanation of the sequence of events during this experiment as follows: As the pump delivers twice the volumetric flow rate as in the experiment Fr03T40, a longer time period is needed for the pump to reach its maximum flow rate. At the beginning of the injection, subcooled water reaches the top of the pipe and flows along the pipe walls downwards to form a liquid film at the bottom of the pipe similar to the Fr03T40 experiment; see figure 6.39. As the subcooled water flows downwards, it entraps a steam pocket which condensates in contact with the cold liquid surface; see figure 6.40. During this experiment, the volumetric flow rate of the subcooled water is continuously increasing until the time reaches 3.0 s. Figure 6.41 shows the flow at 3.05 s, when the maximum flow rate has already been reached and a water wave is growing to become a slug; see figure 6.42.

The transition from stratified to slug flow is mainly driven by the high turbulence of the flow and only minimally influenced by the relatively low subcooling. This effect can be noticed if the distribution of the HTC is analyzed at 3.55 s. The maximum HTC values for the entire simulation domain are located in the cells very close to the free surface, as figure 6.55 shows. The condensation of the entrapped steam pocket causes a local depressurization as seen in figure 6.49 and accelerates the water to fill the void. In figure 6.57 at 4.05 s, a detailed representation of the wave breaking process can be identified in the cross section at location T4. The region in the center of the test pipe shows how the wave rolls back into the liquid bulk, while the transition region between steam and liquid shows a two-phase mixture of entrapped steam bubbles in liquid and water droplets in steam. As no interface reconstruction or special modeling of the disperse phase is made, no sudden increase in the value of the interfacial area density is to observe for the cells

corresponding to the high HTC values shown in figure 6.64 due to the increased turbulence.

The comparison of the simulation results against the measured values for the data recorded by the thermo-couples is presented in figure 6.67. The overall flow behavior in the simulation corresponds well with that observed in the experiment. However, the influence of the boundary conditions to the left- and the right-hand side of the computational domain (modeled as openings), influence the temperature development before the liquid water reaches the location of the thermo-couples. In the experiment a decrease in temperature is recorded due to the decrease in pressure caused by the DCC of steam on the surface of the injected subcooled water. This effect was neglected in the simulation because a constant pressure BC was used for the left and right-hand side separator. The time points at which the temperature significantly decreases when the subcooled water comes into contact with the temperature probes are predicted very well for the locations T3, T2 and T1. In the case of T4, the predicted time point does not match the experiment compared with the other locations but still the flow behavior in the simulation is similar to the one in the experiment. At the location of T4, in both the simulation and the experiment, some temperature oscillations are observed between problem time 2.0 s and 8.0 s. Considering the flow pattern presented in figures 6.41 to 6.45 and the temperature oscillations, it can be concluded that the temperature distribution is not yet fully homogenized in the liquid resulting in stratified fluid layers at different temperatures. Such temperature oscillations can be observed in both simulation results and measured data at the location of the other thermo-couples. The time accuracy of the numerical predictions is even better at locations T1 to T3. The fact that this effect is caught by the CFD simulation is of potential interest if the implications of the formation of a Pressurized Thermal Shock are analyzed. It proves that with a similar set-up as the one used in this thesis consisting of the VOF approach with a SRT based HTC model, the phenomenon of Pressurized Thermal Shock could also be accurately analyzed.

Another important similarity between the simulation and the experimental results can be appreciated from the point of view of the time at which both Tg and Tf converge to the same value. At an early stage in the experiment, both temperature probes are in contact with saturated steam but at a certain point subcooled water comes into contact with them, first with the Tf thermo-couple and then with Tg. The coincidence of these time points would be an additional indicator that the local flow pattern at the location where the sensors are mounted is predicted correctly within the simulation. A sudden decrease of both measured temperatures indicates that the entire cross-section is probably filled with water. However, it could also be a result of an annular flow regime where only a liquid film is in contact with the pipe walls. These time points are predicted with very good temporal accuracy by the CFD simulation employing the hybrid HTC model. Therefore it can be concluded that the flow pattern predicted by the simulation based on the SRT model for direct contact condensation and the VOF approach is consistent with the measurements in the case of high turbulence intensity and low liquid subcooling.

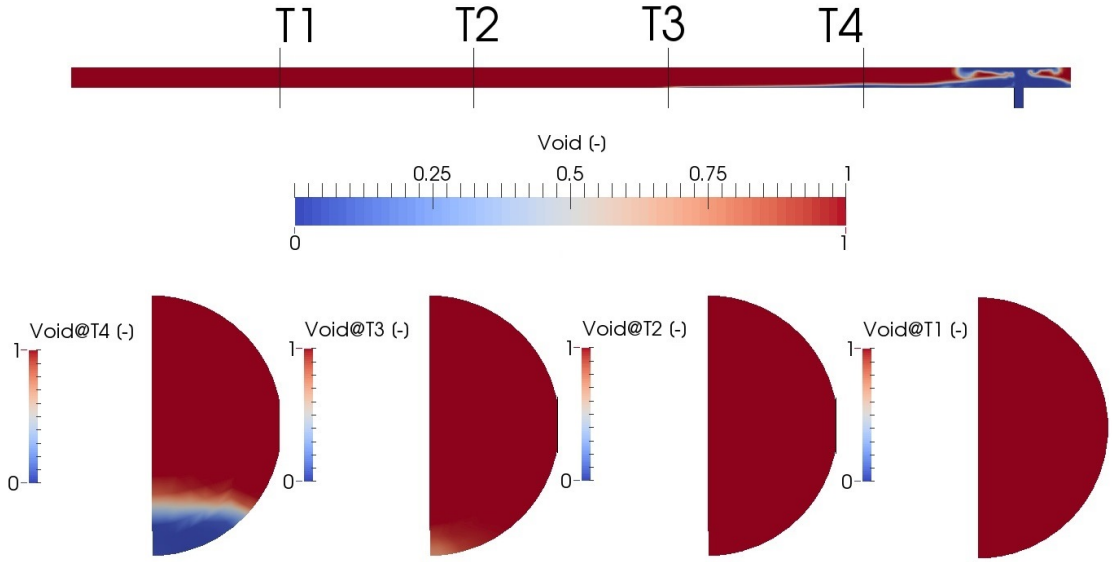

Figure 6.39: CFD results of the fully developed 'water fountain' with built up water film at problem time 1.80 s, TUHH experiment Fr06T40

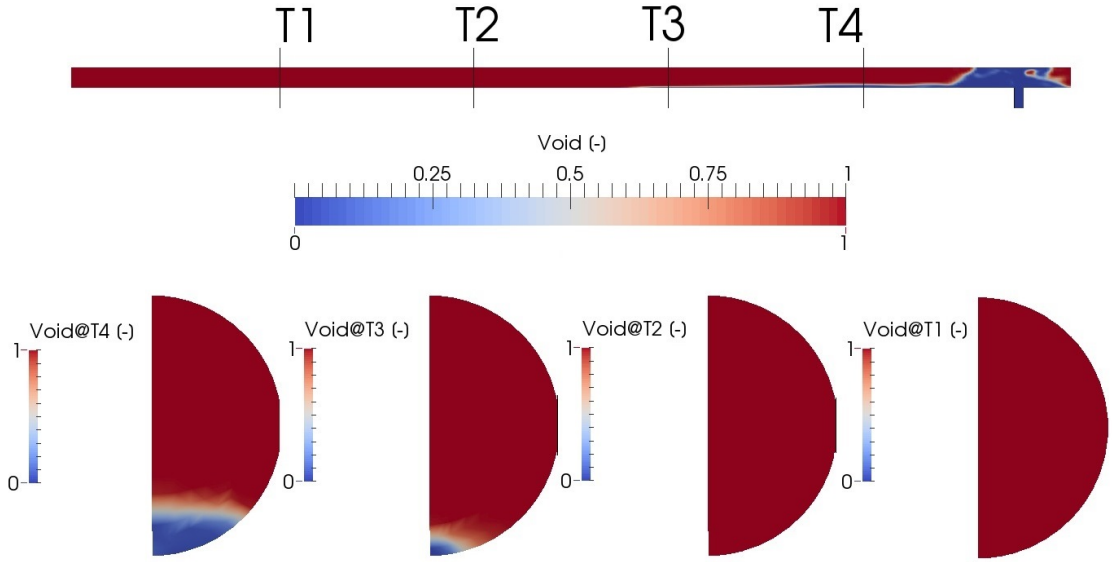

Figure 6.40: CFD results of the transition from horizontal to wavy flow at problem time 1.90 s, TUHH experiment Fr06T40

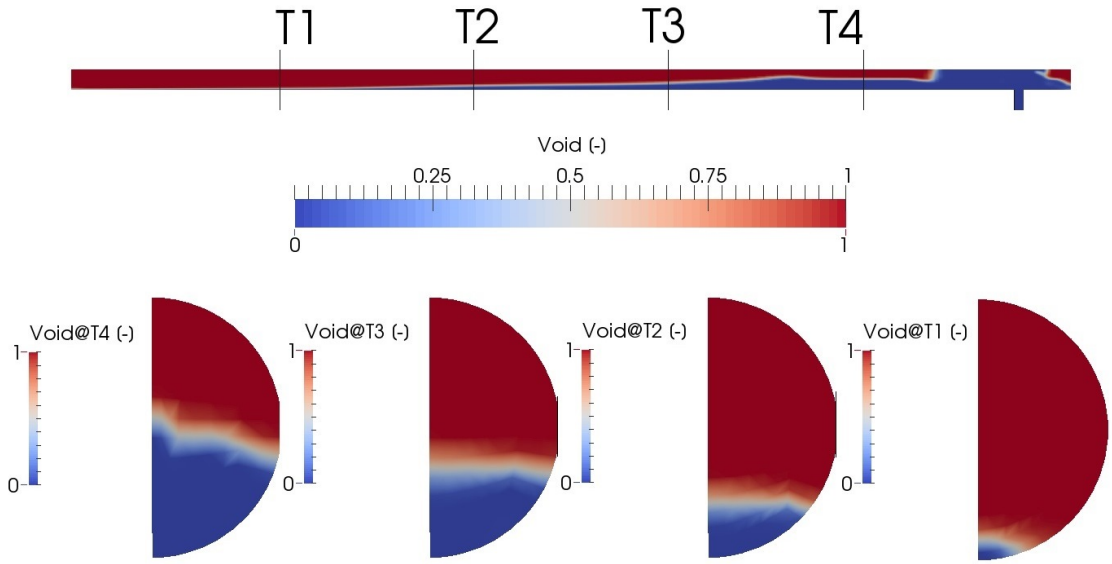

Figure 6.41: CFD results of the water wave growing to form a slug at problem time 3.55 s, TUHH experiment Fr06T40

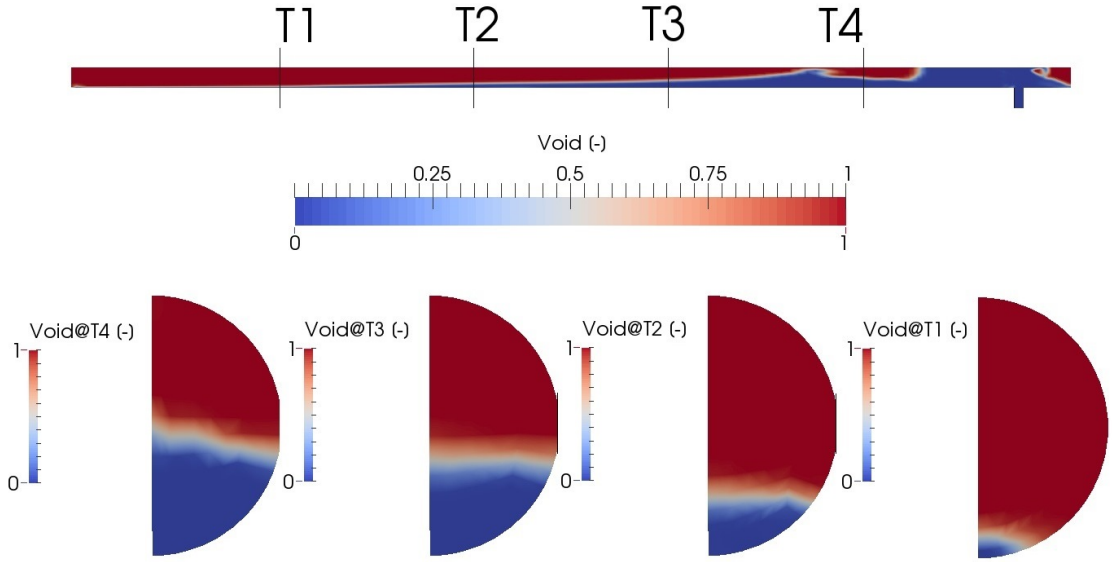

Figure 6.42: CFD results of the decay of the water wave at problem time 3.70 s, TUHH experiment Fr06T40

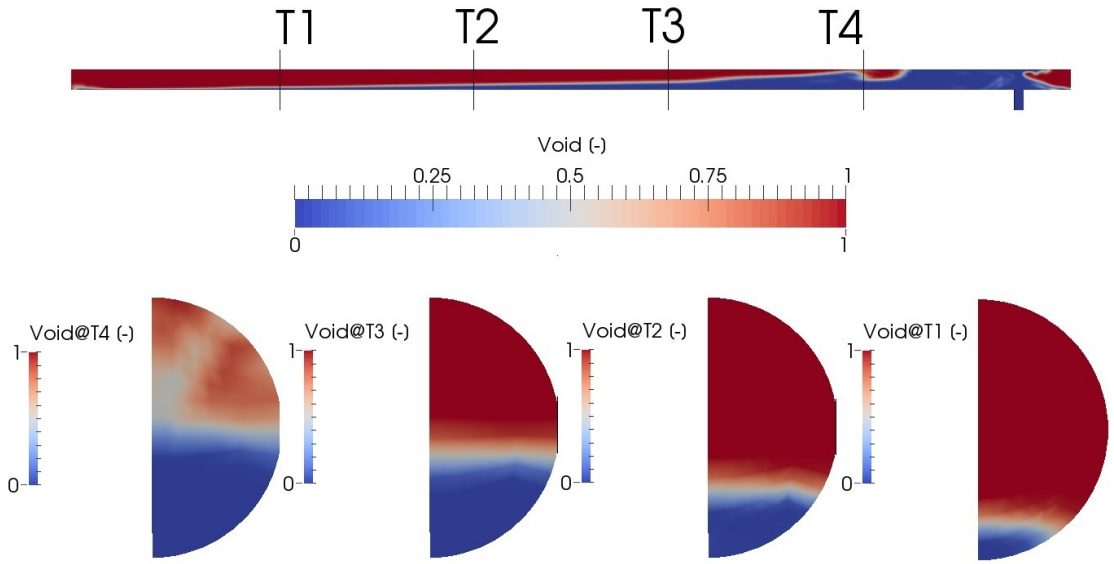

Figure 6.43: CFD results of the second water wave growing to form a slug at problem time 4.05 s, TUHH experiment Fr06T40

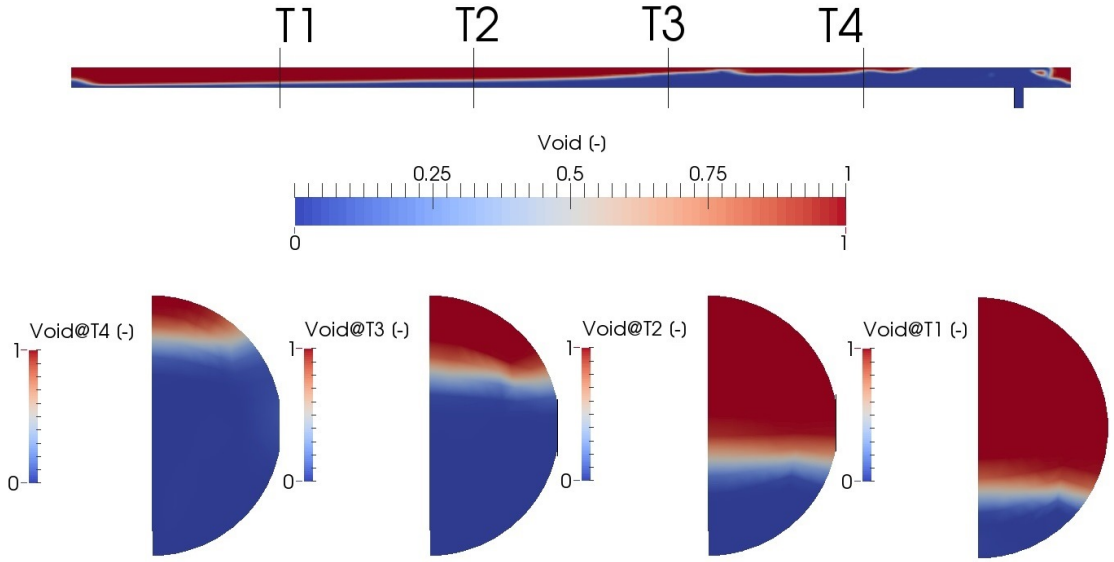

Figure 6.44: CFD results of the third water wave growing to form a slug at problem time 4.90 s, TUHH experiment Fr06T40

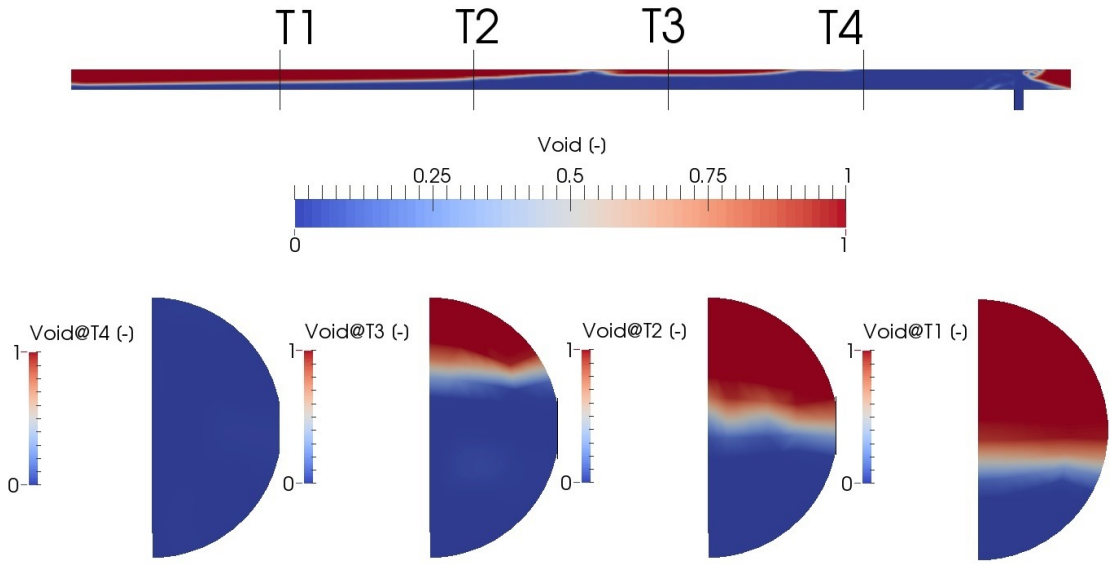

Figure 6.45: CFD results of the fourth water wave growing to form a slug at problem time 6.05 s, TUHH experiment Fr06T40

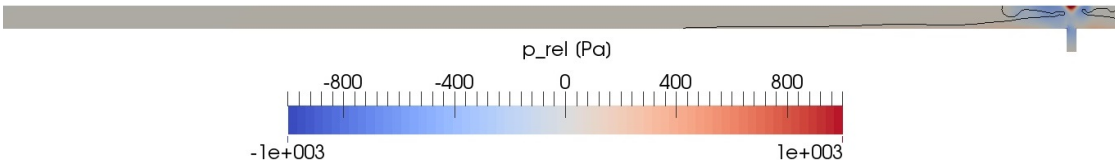

Figure 6.46: CFD results of the relative pressure field with 0.5 void fraction contour line at problem time 1.80 s, TUHH experiment Fr06T40

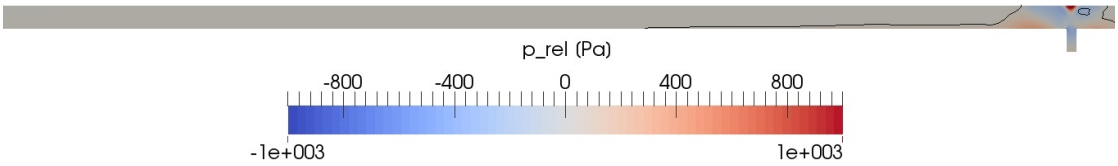

Figure 6.47: CFD results of the relative pressure field with 0.5 void fraction contour line at problem time 1.90 s, TUHH experiment Fr06T40

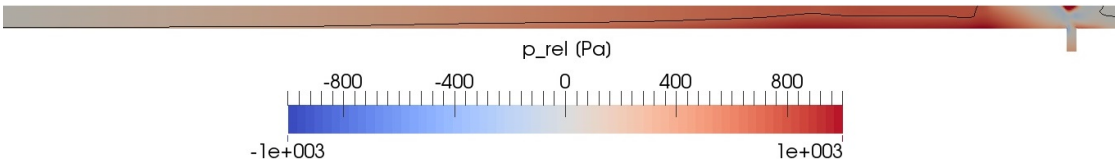

Figure 6.48: CFD results of the relative pressure field with 0.5 void fraction contour line at problem time 3.55 s, TUHH experiment Fr06T40

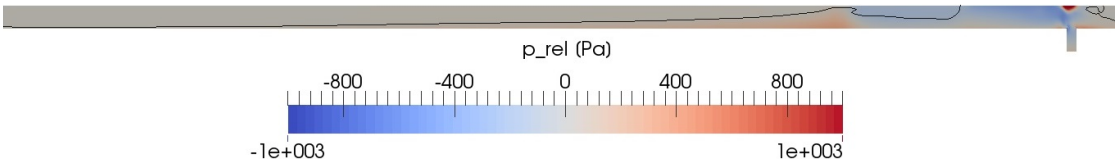

Figure 6.49: CFD results of the relative pressure field with 0.5 void fraction contour line at problem time 3.70 s, TUHH experiment Fr06T40

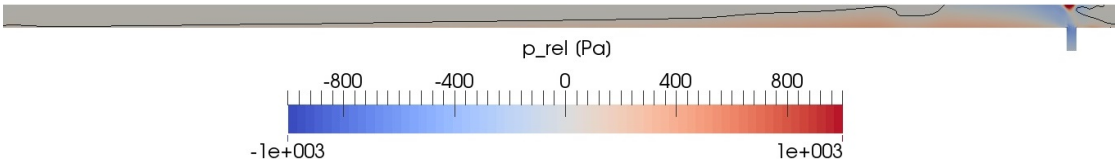

Figure 6.50: CFD results of the relative pressure field with 0.5 void fraction contour line at problem time 4.05 s, TUHH experiment Fr06T40

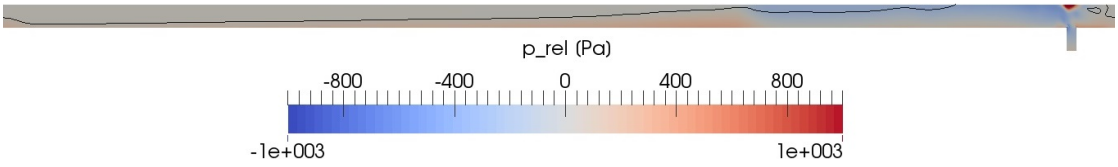

Figure 6.51: CFD results of the relative pressure field with 0.5 void fraction contour line at problem time 4.90 s, TUHH experiment Fr06T40

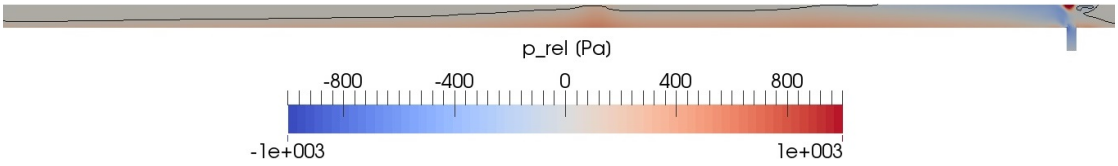

Figure 6.52: CFD results of the relative pressure field with 0.5 void fraction contour line at problem time 6.05 s, TUHH experiment Fr06T40

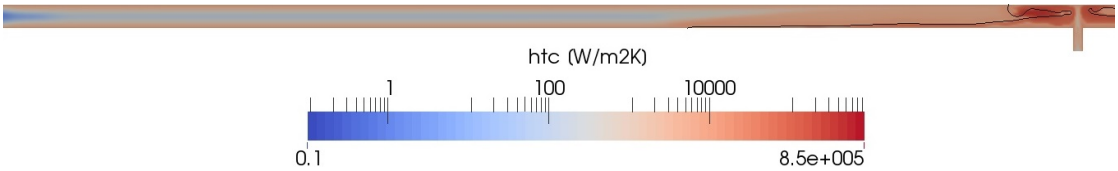

Figure 6.53: CFD results of the HTC field with 0.5 void fraction contour line at problem time 1.80 s, TUHH experiment Fr06T40

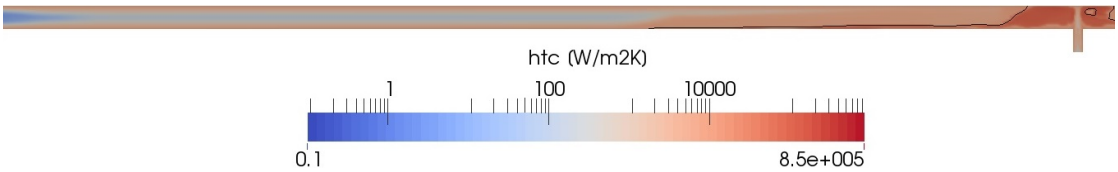

Figure 6.54: CFD results of the HTC field with 0.5 void fraction contour line at problem time 1.90 s, TUHH experiment Fr06T40

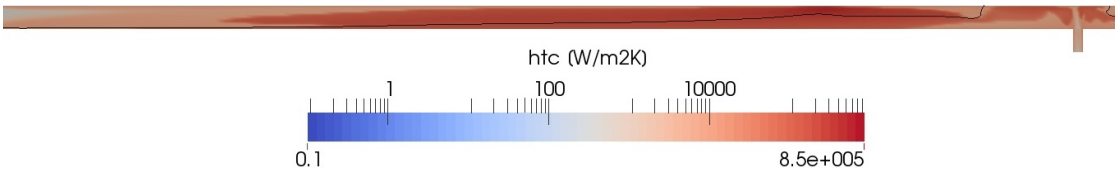

Figure 6.55: CFD results of the HTC field with 0.5 void fraction contour line at problem time 3.55 s, TUHH experiment Fr06T40

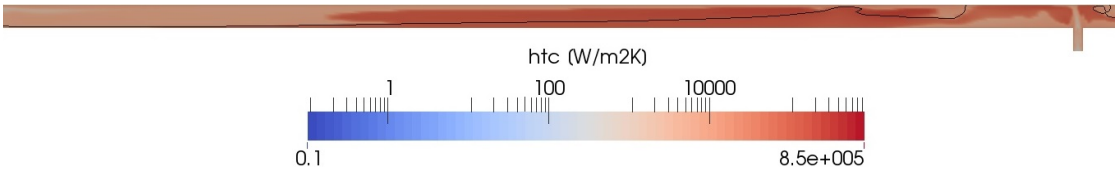

Figure 6.56: CFD results of the HTC field with 0.5 void fraction contour line at problem time 3.70 s, TUHH experiment Fr06T40

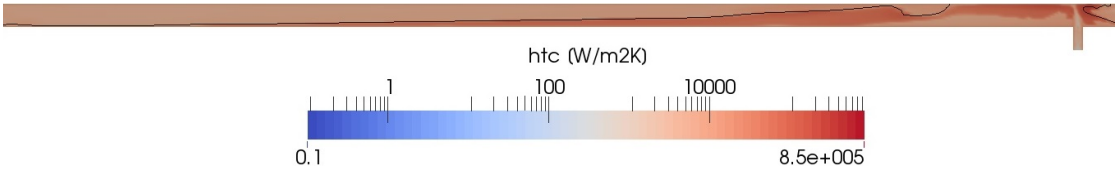

Figure 6.57: CFD results of the HTC field with 0.5 void fraction contour line at problem time 4.05 s, TUHH experiment Fr06T40

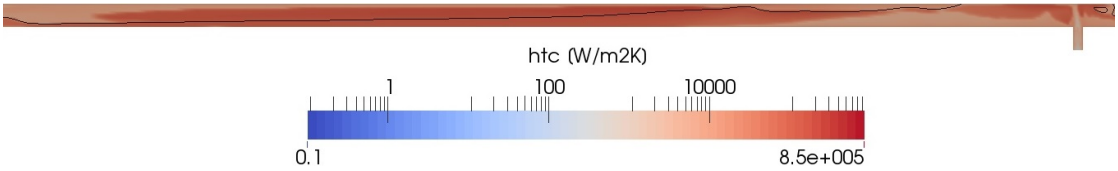

Figure 6.58: CFD results of the HTC field with 0.5 void fraction contour line at problem time 4.90 s, TUHH experiment Fr06T40

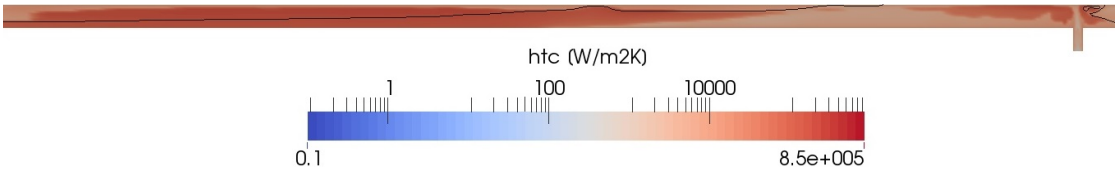

Figure 6.59: CFD results of the HTC field with 0.5 void fraction contour line at problem time 6.05 s, TUHH experiment Fr06T40

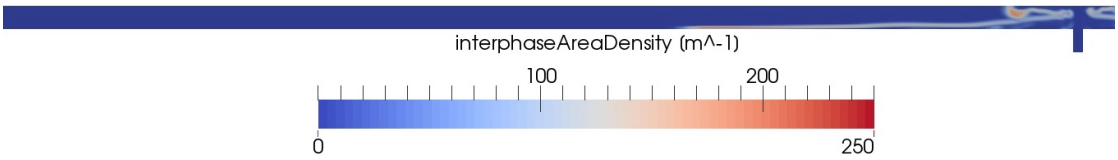

Figure 6.60: CFD results of the fully developed 'water fountain' with a liquid film at the bottom of the pipe at problem time 1.80s, TUHH experiment Fr06T40

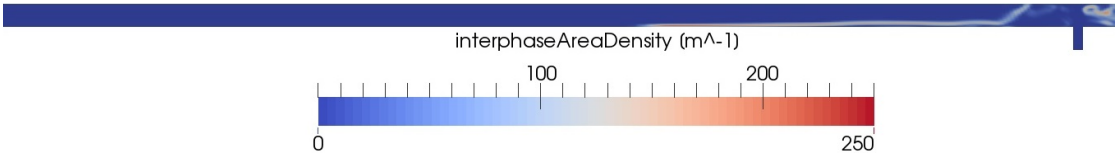

Figure 6.61: CFD results of the transition from horizontal to wavy flow at problem time 1.90 s, TUHH experiment Fr06T40

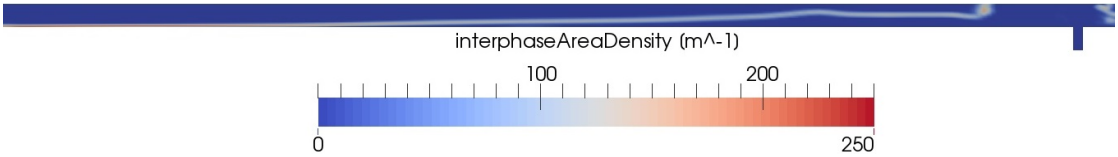

Figure 6.62: CFD results of the water wave growth to become a slug problem time 3.55 s, TUHH experiment Fr06T40

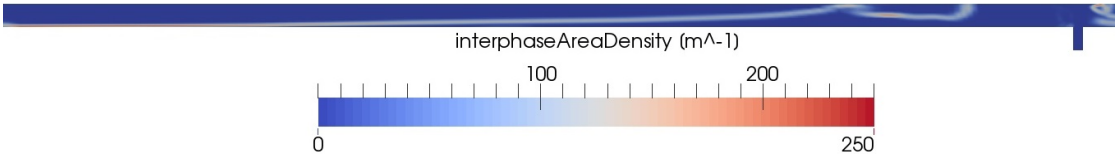

Figure 6.63: CFD results of the collapse of entrapped steam pocket at problem time 3.70 s, TUHH experiment Fr06T40

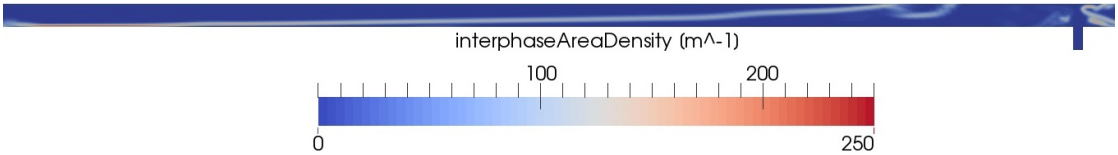

Figure 6.64: CFD results of the second water wave growing to form a slug at problem time 4.05 s, TUHH experiment Fr06T40

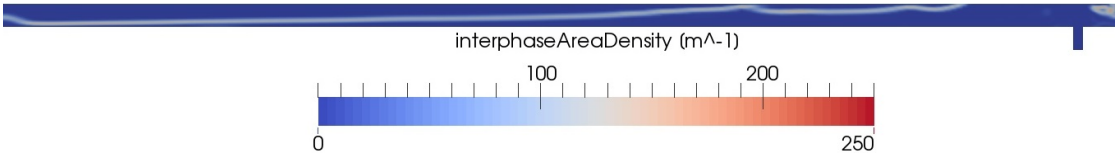

Figure 6.65: CFD results of the third water wave growing to form a slug at problem time 4.90 s, TUHH experiment Fr06T40

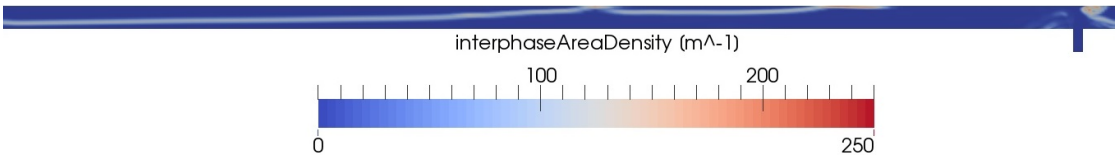

Figure 6.66: CFD results of the third water wave growing to form a slug at problem time 6.05 s, TUHH experiment Fr06T40

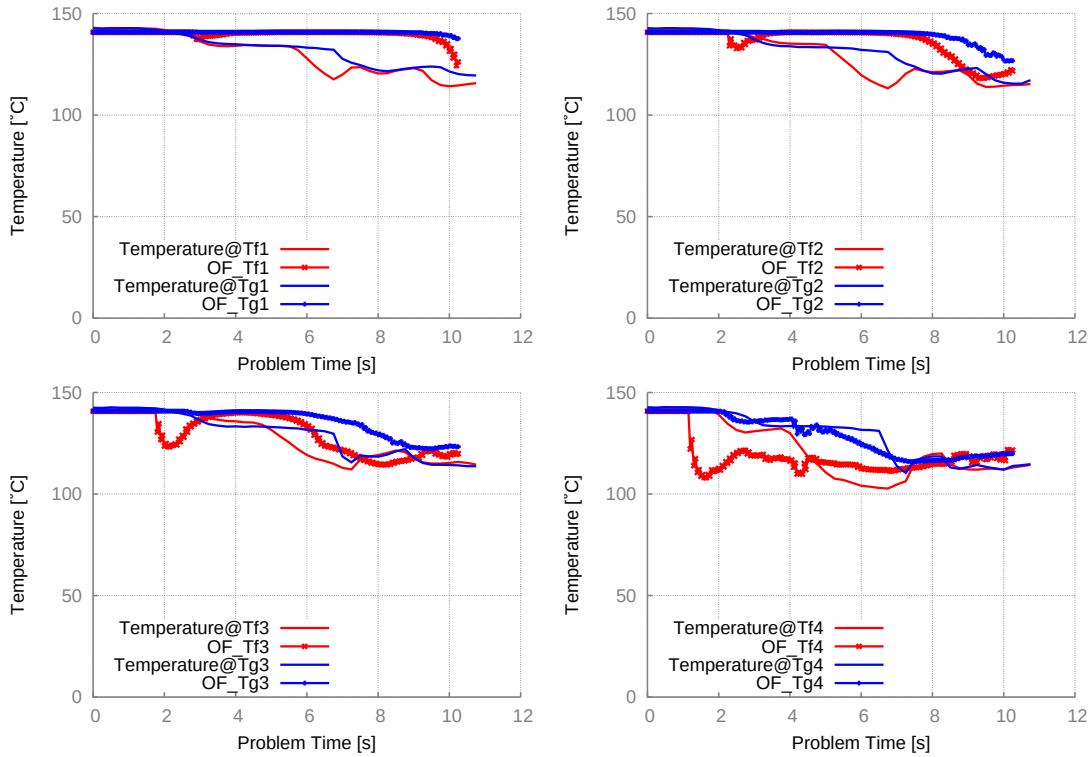

Figure 6.67: CFD results of the temperature at the thermo-couples Tf and Tg TUHH experiment Fr06T40

6.2.3 CFD Simulation of the TUHH Experiment Fr06T60

The experiment Fr06T060 provides data for the flow with the highest Froude Number (Fr) number reached in the TUHH experimental series together with the highest subcooling of the injected feed-water. According to the CFD analysis of the previously described experiments of transient two-phase flow, two performed at the TUHH and one at PMK-2, it can be expected, that both driving forces of flow pattern changes, i.e. the subcooling and the turbulence intensity will impact the two-phase flow dynamics in this experiment. The analysis of the flow evolution based on the time dependent patterns in the test-section, represented with the help of the void fraction as shown in figures 6.68 to 6.73, proves that the two-phase flow simulated in this experiment possesses the most complex dynamics of all TUHH simulated experiments. This confirms the fact that the influence of the flow turbulence considered in the mathematical formulation of the SRT based hybrid HTC is consistent with experimental observations. According to the simulation results, in the early phase of this experiment the subcooled water reaches the top of the test pipe and forms the water *fountain* already described in the previously simulated TUHH experiments. A liquid film is created as the water rejoins at the bottom of the pipe after flowing down its wall. This liquid film then flows towards the left side of the test-section and passes by the measurement location T4 according to figure 6.68. Due to the high condensation rates influenced by the high turbulence intensity and the high liquid subcooling, a liquid mass with the shape of a plug forms very close to the injection location. The stratified flow then changes to a wavy pattern after only 2.70 s and shortly thereafter this wave grows to a slug entrapping a steam pocket. The entrapment occurs at approximately 2.80 s, as shown in figure 6.70. This wave eventually grows to form a slug. This behavior can be explained by analyzing the increase in the value of the condensation HTC as shown in figure 6.81 leading together with a sufficiently high IAD resulting from high turbulence, see figure 6.87, to a significant increase in the local condensation rate. The entrapped steam bubble then rapidly collapses and the water continues to flow towards the left side of the test-section; see figure 6.71. It is important to notice that following the high condensation rates, such an important depressur-

ization appears, that the entire water inventory introduced into the test-section is drawn back to the region of the T-junction, as can be noticed in figures 6.70 and 6.71. The water film which has almost reached T3 travels upstream, even with the 1.4 slope of the pipe, due to the large local depressurization. Some more slugs are created as the flow continues to the left. These slugs travel upstream toward the injection location at the T-junction according to figures 6.72 and 6.73. Optical observations of the flow confirmed a similar flow behavior no CIWH event could be noticed in the simulations [10]. Still the flow behavior predicted by the CFD simulation describes in detail the flow pattern evolution which has to be present in a two-phase flow in order for a CIWH to occur.

The standard VOF employed method for the calculation of the IAD fails to realistically compute the interfacial area in the regions with high turbulence, i.e. the same regions showing increased HTC values. This is also one cause why no CIWH could be computed in this simulation, whereas in the experiment some events have been observed [11]. The OpenFOAM simulation temperature distribution results of this experiment and the measured data are presented in figure 6.92. As in the previous simulations of the TUHH experimental facility, the boundary conditions employed on the left and right-hand side of the test-section do not consider the finite steam inventory available in the real facility. Consequently, a constant pressure is kept during the early phase of the simulation due to inflow of saturated steam.

The comparison of the temperature trends measured at T4 shows that the subcooled water reaches the location of the thermo-couples Tf4 and Tg4 sooner in the simulation than in the experiment. Still, the overall trend recorded by Tf4: initially decreasing then increasing back to the saturation temperature and then both temperatures Tf4 and Tg4 decreasing, is also observed in the experiment. The fact that the temperature first decreases close to Tf4 and then it increases back to the saturation temperature both in the simulation and in the experiment proves that the subcooled liquid reaches the location of Tf4 and then is drawn back to the location of the T-junction. Considering that the liquid has to overcome the slope of the test-section, only heavy condensation rates close to the injection point

can explain such a behavior. This proves that the mechanistic SRT based HTC model realistically captures the influence of the turbulence thus underlining the need for more than one eddy length scale for the calculation of the surface renewal period.
Even if the exact time point at which the phenomenon of flow reversal occurs is under-predicted by the simulation, the insights into the complex two-phase flow dynamics is of great value. The time needed in the experiment until the pipe cross section close to T4 is filled with subcooled water is longer than in the simulation meaning that the flow takes longer in the experiment to transition from stratified to slug.
The comparison of the temperature trends at T3 also shows the similarity observed at T4. The time at which subcooled water reaches the temperature probes is again under-predicted. Nevertheless, in both the simulation and the recorded data, first a liquid film reaches Tf3 and an additional 2.0 s are needed until subcooled water reaches the top mounted Tg3 thus filling up the entire pipe cross section at this location.

The simulation results better fit the experimental data as the flow reaches the location of T2 and T1. The predictions of the time point when the subcooled water reaches the thermo-couples are more accurate and the time taken by the water to fill the entire cross section in the case of the CFD simulation is also in good agreement with the measured data. In general, the long time behavior of the temperature trends in the simulation and experiment based on the recorded and calculated data at the probes locations appears very similar.
Compared to the other two simulated experiments at the TUHH facility discussed above, the flow pattern changes the earliest in this experiment clearly indicating the simultaneous influence of both the high volumetric flow rate delivered by the pump, which induces a higher turbulence, as well as the high liquid subcooling. In the experiment with low volumetric flow rate, the flow needs approximately 4.0 s to change from stratified to wavy and an additional 0.50 s to entrap a steam pocket. For the same initial conditions, the flow needs only approximately 3.60 s

to change from stratified to wavy flow in the case with a higher volumetric flow rate but with a similar low subcooling. Then an additional 0.40 s are required to entrap the steam pocket. If both the volumetric flow rate and the subcooling are high, these times are decreased to approx. 2.60 s for the first major change in the flow pattern and only 0.10 s more for a steam bubble entrapment.

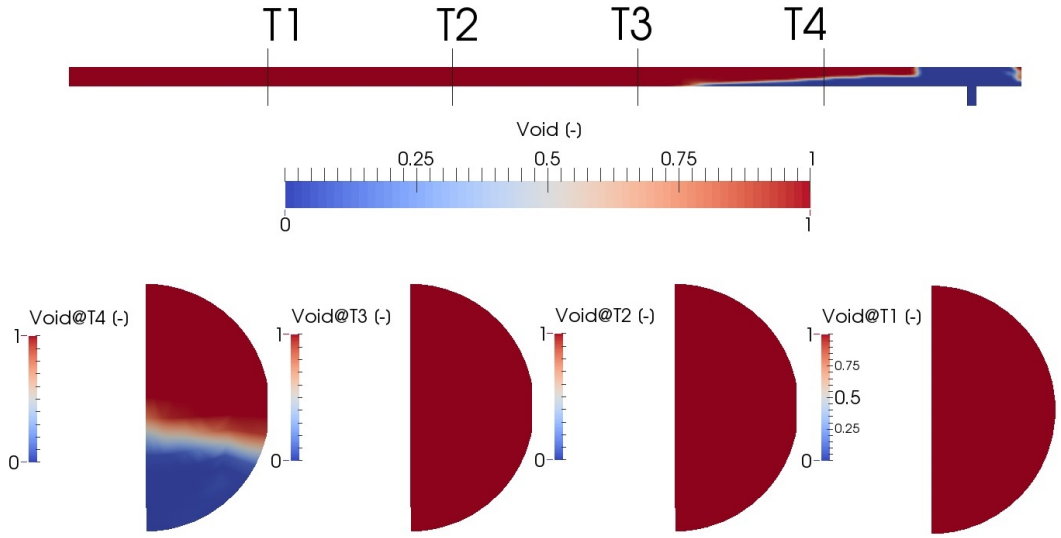

Figure 6.68: CFD results of the fully developed 'water fountain' with built up water film at problem time 2.60 s, TUHH experiment Fr06T60

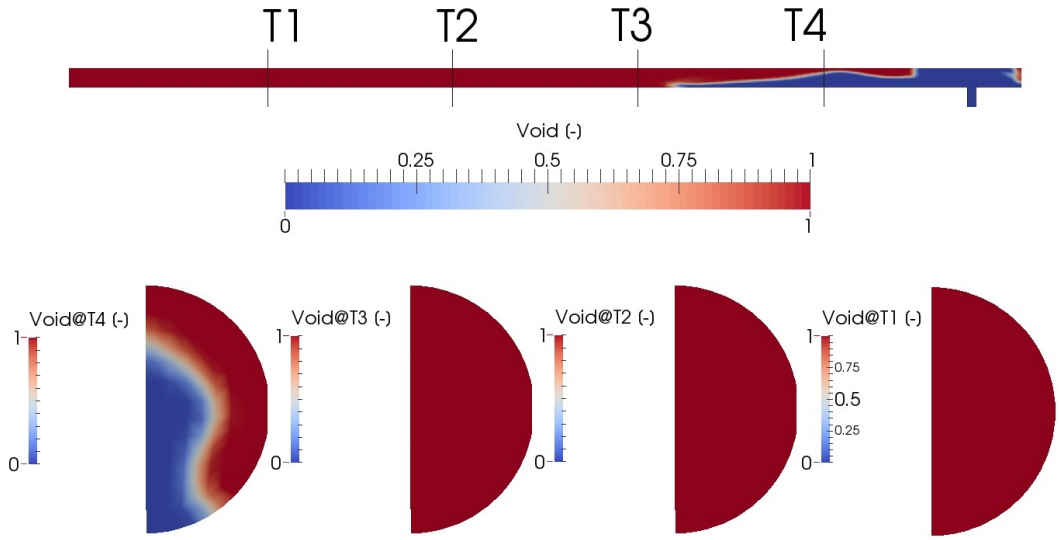

Figure 6.69: CFD results of the transition from horizontal to wavy flow at problem time 2.70 s, TUHH experiment Fr06T60

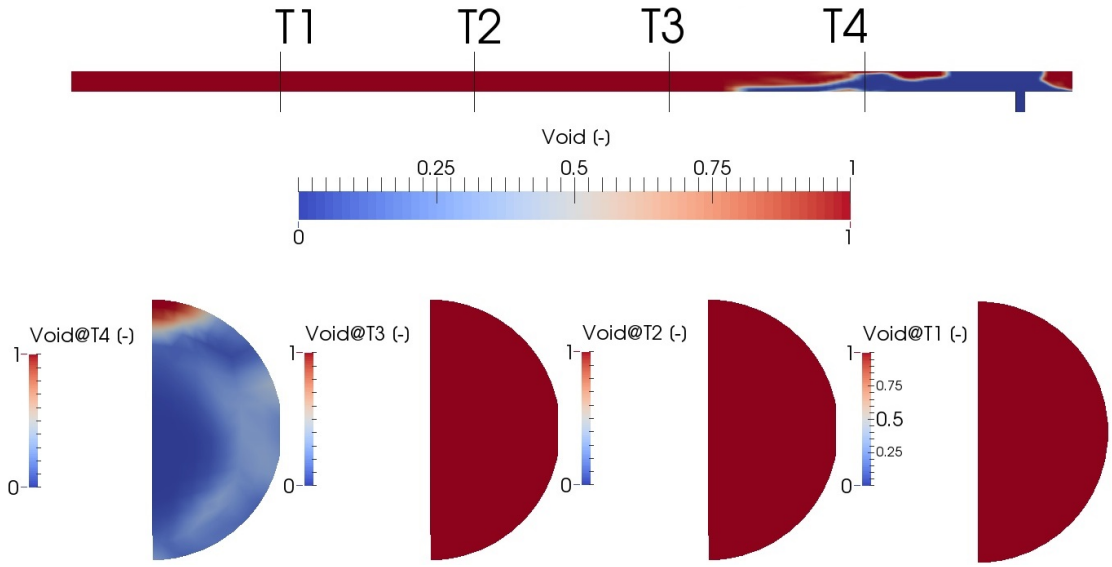

Figure 6.70: CFD results of the water wave growing to form a slug at problem time 2.80 s, TUHH experiment Fr06T60

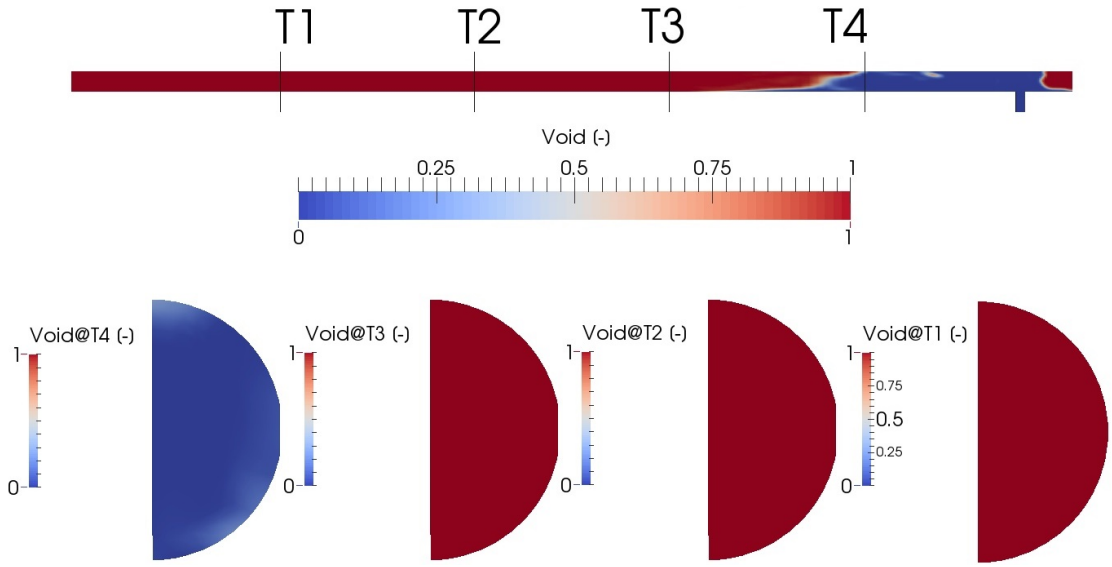

Figure 6.71: CFD results of the collapse of the entrapped steam pocket at problem time 3.00 s, TUHH experiment Fr06T60

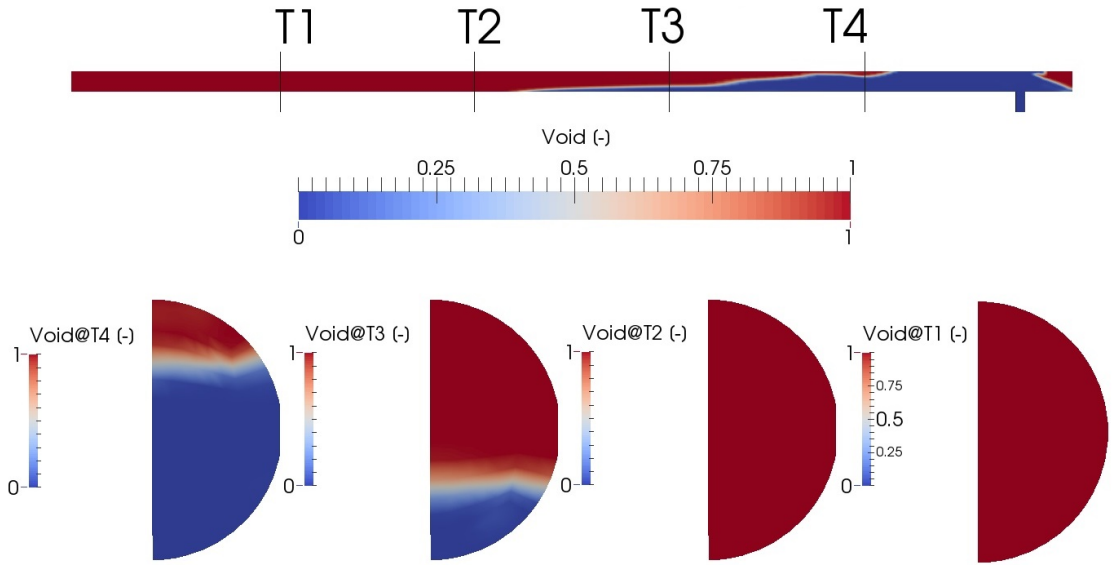

Figure 6.72: CFD results of the second water wave growing to form a slug at problem time 3.75 s, TUHH experiment Fr06T60

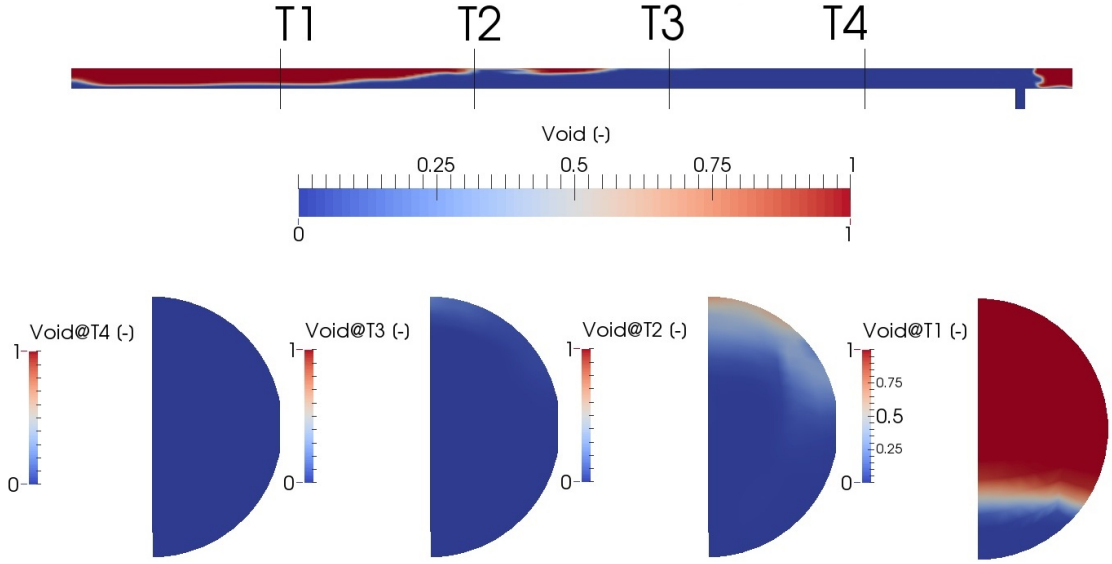

Figure 6.73: CFD results of the third water wave growing to form a slug at problem time 5.90 s, TUHH experiment Fr06T60

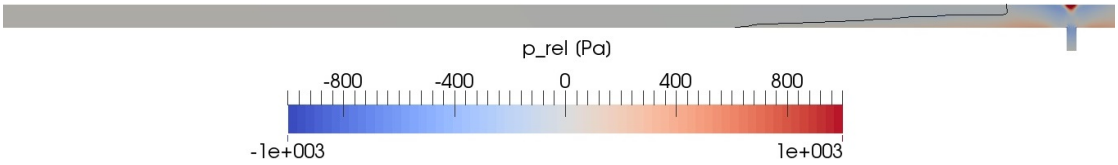

Figure 6.74: CFD results of the relative pressure field with 0.5 void fraction contour line at problem time 2.60 s, TUHH experiment Fr06T60

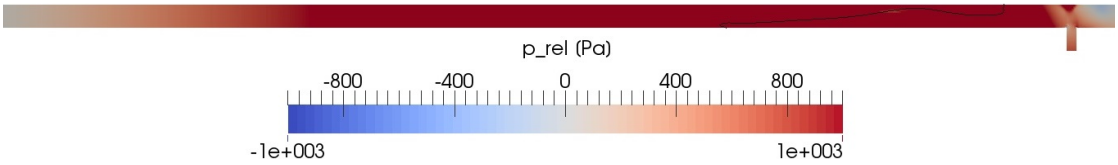

Figure 6.75: CFD results of the relative pressure field with 0.5 void fraction contour line at problem time 2.70 s, TUHH experiment Fr06T60

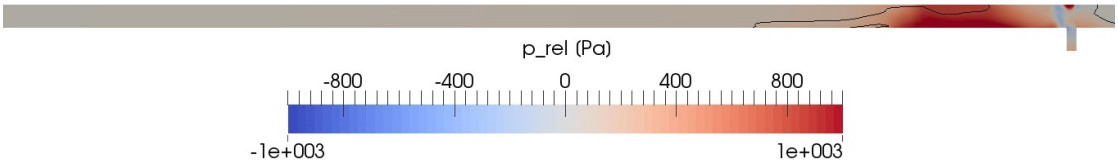

Figure 6.76: CFD results of the relative pressure field with 0.5 void fraction contour line at problem time 2.80 s, TUHH experiment Fr06T60

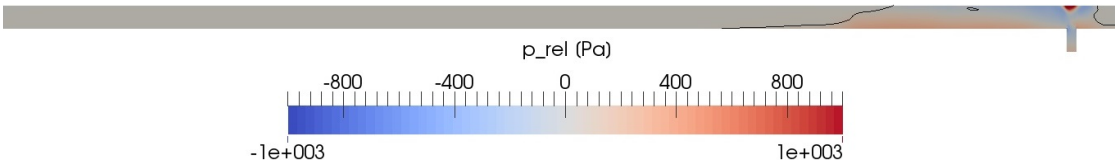

Figure 6.77: CFD results of the relative pressure field with 0.5 void fraction contour line at problem time 3.00 s, TUHH experiment Fr06T60

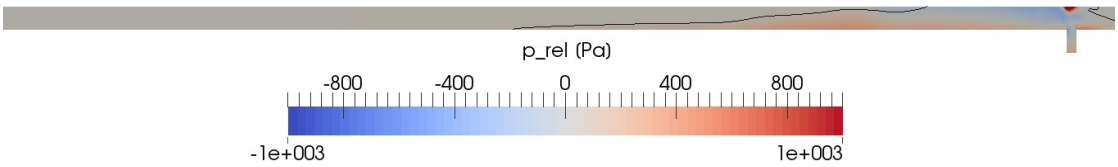

Figure 6.78: CFD results of the relative pressure field with 0.5 void fraction contour line at problem time 3.75 s, TUHH experiment Fr06T60

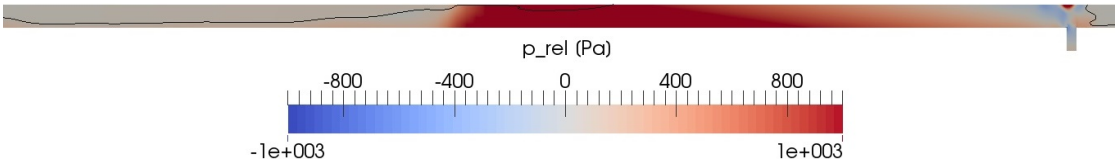

Figure 6.79: CFD results of the relative pressure field with 0.5 void fraction contour line at problem time 5.90 s, TUHH experiment Fr06T60

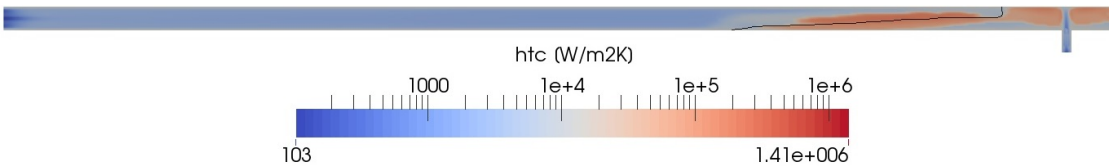

Figure 6.80: CFD results of the HTC field with 0.5 void fraction contour line at problem time 2.60 s, TUHH experiment Fr06T60

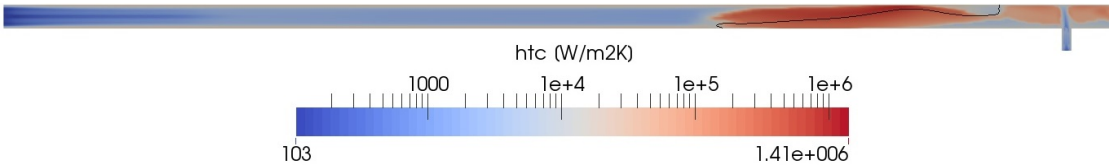

Figure 6.81: CFD results of the HTC field with 0.5 void fraction contour line at problem time 2.70 s, TUHH experiment Fr06T60

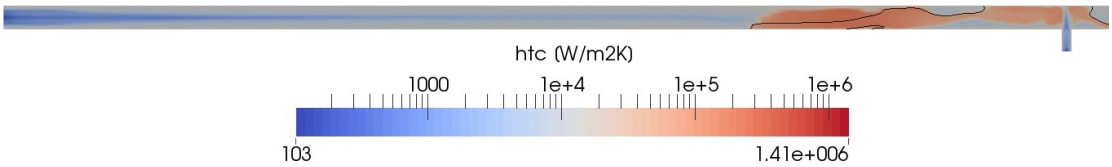

Figure 6.82: CFD results of the HTC field with 0.5 void fraction contour line at problem time 2.80 s, TUHH experiment Fr06T60

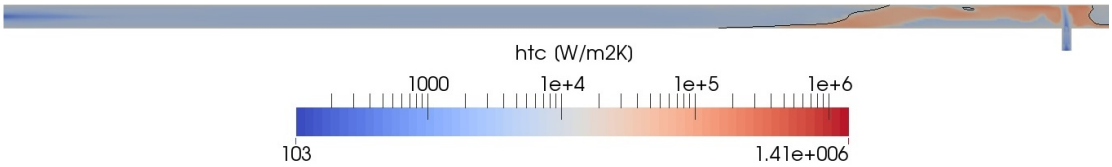

Figure 6.83: CFD results of the HTC field with 0.5 void fraction contour line at problem time 3.00 s, TUHH experiment Fr06T60

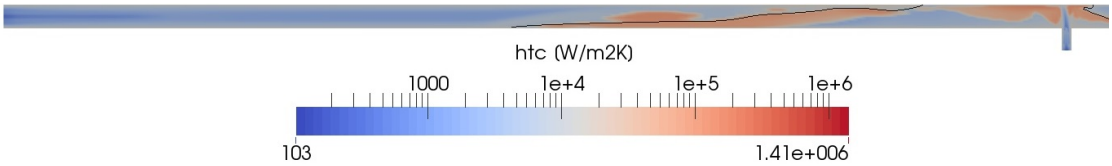

Figure 6.84: CFD results of the HTC field with 0.5 void fraction contour line at problem time 3.75 s, TUHH experiment Fr06T60

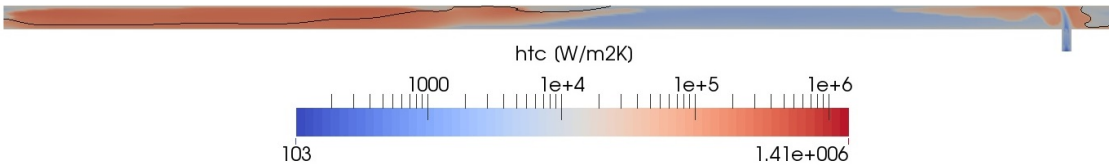

Figure 6.85: CFD results of the HTC field with 0.5 void fraction contour line at problem time 5.90 s, TUHH experiment Fr06T60

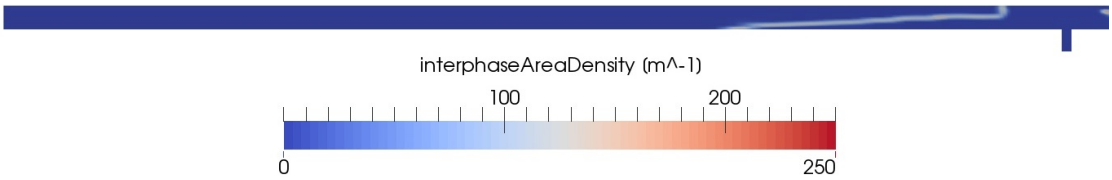

Figure 6.86: CFD results of the fully developed 'water fountain' with built up water film at problem time 2.60 s, TUHH experiment Fr06T60

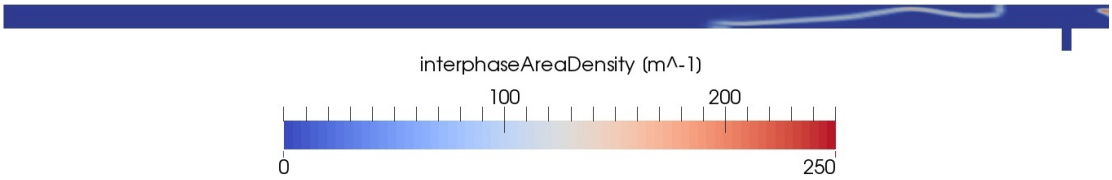

Figure 6.87: CFD results of the transition from horizontal to wavy flow at problem time 2.70 s, TUHH experiment Fr06T60

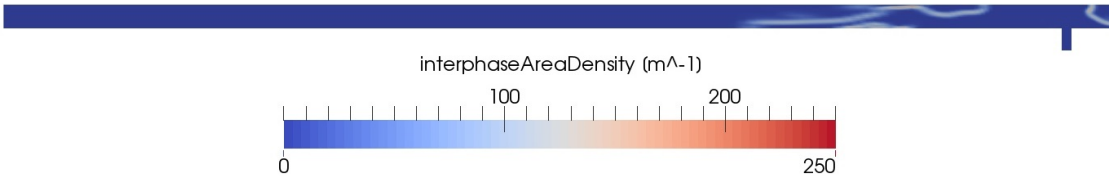

Figure 6.88: CFD results of the water wave growing to form a slug at problem time 2.80 s, TUHH experiment Fr06T60

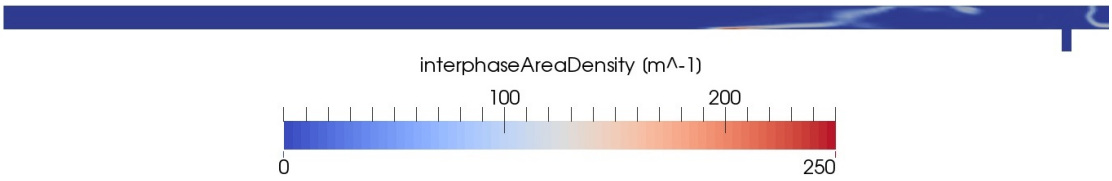

Figure 6.89: CFD results of the collapse of the entrapped steam pocket at problem time 3.00 s, TUHH experiment Fr06T60

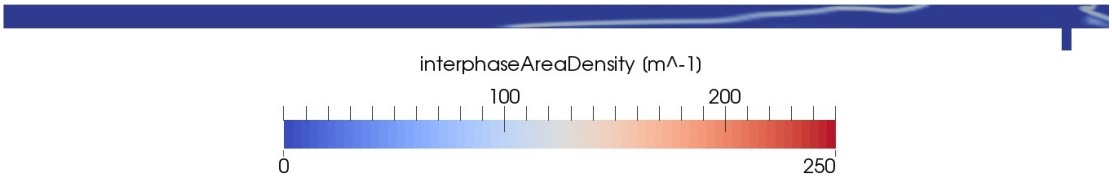

Figure 6.90: CFD results of the second water wave growing to form a slug at problem time 3.75 s, TUHH experiment Fr06T60

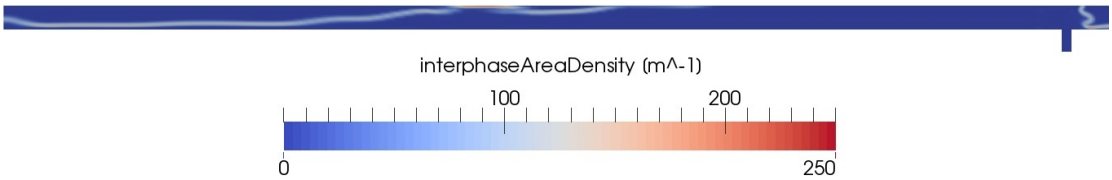

Figure 6.91: CFD results of the third water wave growing to form a slug at problem time 5.90 s, TUHH experiment Fr06T60

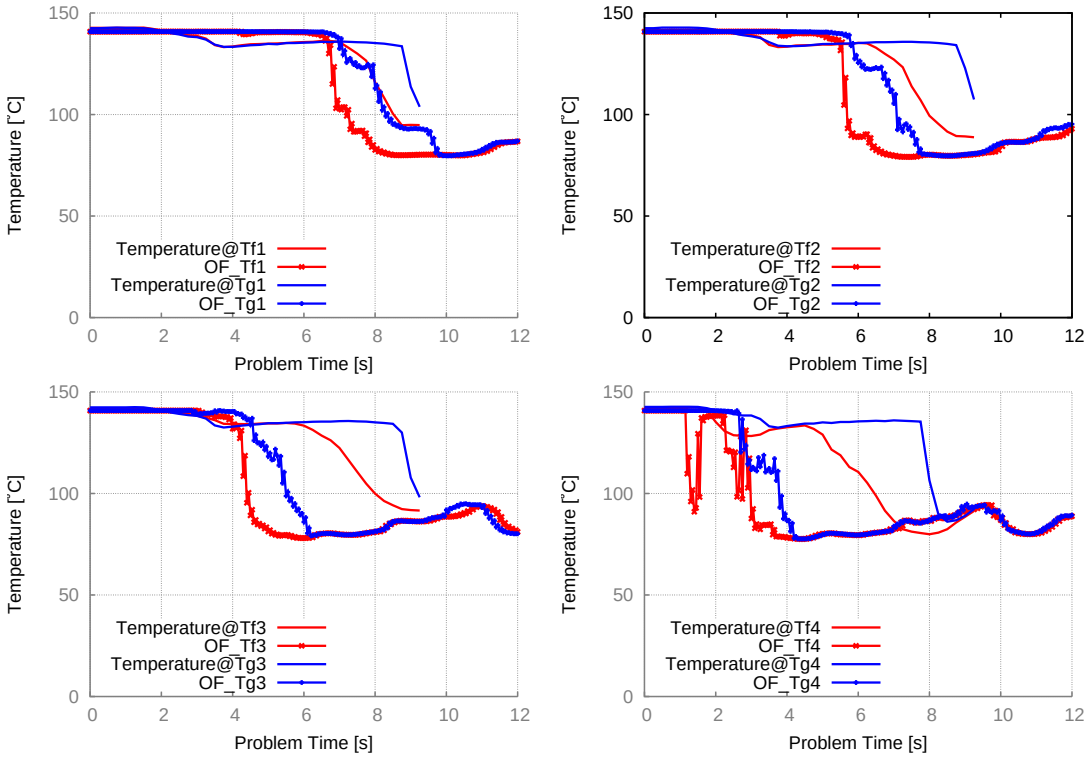

Figure 6.92: CFD results of the temperature at the thermo-couples Tf and Tg, TUHH experiment Fr06T60

Chapter 7

Conclusions and Outlook

This work presents state of the art CFD and system code simulations of two-phase flow with direct contact condensation acting as the onset for water hammer phenomena. Additionally a new hybrid HTC model is developed, implemented and assessed for the simulation of condensation induced water hammer phenomena. The new hybrid surface renewal theory based HTC model was successfully assessed against measurement data from a horizontal quasi-steady state experiment. Afterwards the same model is assessed against measurement data recorded at four more complex transient flow experiments performed at the PMK-2 and the TUHH facilities. The assessment against data acquired during transient two-phase flow experiments is very important because in such experiments one of the key variables in the flow pattern evolution is the condensation rate which can act as the driving force for water hammer. The computer simulations performed with the newly developed hybrid HTC model have proven to not require any parameter tuning by the user for the realistic simulation of two-phase flow with DCC. This improvement enhances the predictive capabilities of such computer codes.
After the threshold of the turbulent Reynolds number, a key variable of the hybrid HTC model, was determined, CFD simulations could predict the interface morphology in transient two-phase flow with DCC in high detail. The employed VOF method can handle complex interface morphology, for example breaking waves or rolling wave crests, as presented in figure 6.24, even if the region above the water

bulk, the transition from the color blue to the color red, is a 'smeared' area of several cells. This smeared field requires additional modeling of the entrapped steam bubbles in the water phase and the liquid droplets in steam bulk, for more accurate simulations. The CFD simulations of the PMK-2 experiment highlighted the requirement of a hybrid HTC model. These simulations of the PMK-2 experiment with the hybrid HTC model matched with good accuracy the measurement data while the simulations using only the individual SRT based HTC models failed. The model relying only on macroscale eddies for the calculation of the HTC model underpredicted the resulting condensation rate and failed to correctly estimate the phase change induced flow regime transition. On the other hand, the microscale based HTC model overpredicted the condensation rate and resulted in a flow regime transition too early in the simulation compared with the measurement data. Still the microscale based HTC model underlined the capabilities of ANSYS CFX to simulate CIWH phenomena.

The OpenFOAM simulations of the TUHH experiments provided high resolution results of the interface morphology. All three simulated experiments followed the scenario of a growing 'water fountain' as the subcooled water was injected into the test-section, a developing peripheral flow and eventually a bubble entrapment.

Regarding the computer simulations of the TUHH experiments, it can be concluded that for the experiments where the subcooling was low, approximately 40 K, the time points at which the liquid reaches the thermo-couples are predicted with very good temporal accuracy. Thus the two-phase flow dynamic is predicted correctly with the VOF method in combination with the hybrid HTC model. Additionally, the computed temperatures are consistent with the measurement data. Comparing the two experiments with the 40 K subcooling, it can be noticed that the turbulence feedback in the calculation of the HTC using the hybrid SRT approach is correctly accounted for.

The TUHH experiment with the high injection rate plus the high subcooling shows, an overlapped effect due to the subcooling and the increased turbulence on the two-phase flow dynamics. During this simulation the flow pattern changes the earliest of the three TUHH experiments clearly indicating the simultaneous influence of

both the high volumetric flow rate delivered by the pump and the high subcooling. In the experiment with the low volumetric flow rate and low subcooling, the flow needs approximately 4.00 s to change from stratified to wavy and an additional 0.50 s to trap a steam pocket. In the experiment with the high injection rate but with the low subcooling, the flow needs only approx. 3.60 s to change from stratified to wavy flow; to entrap a steam pocket an additional 0.40 s problem time is required. If both the volumetric flow rate and the subcooling are high, these time periods are decreased to approximately 2.60 s for the first major change in the flow pattern and only 0.10 s more seconds for a steam bubble entrapment. Considering that the pump needs approximately 2.60 s to reach its maximum volumetric flow, the shorter time needed in the experiment with the 60 K subcooling, is a direct and clear cause of the increased subcooling.

Even if the results of all CFD simulations matched with very good accuracy the measurement data, no pressure surges could be realistically simulated with any of the CFD tools. The reasons why no CIWH could be reliably simulated with any of the CFD tools is on one hand the lack of robust high order numerical schemes for solving the individual terms of the two-phase flow conservation equations and on the other hand, the fact that the model used for the calculation of the IAD within VOF has no feedback due to an increase of the turbulence. At this point, this seems to be a limitation of the standard VOF methodology for the simulations of CIWH phenomena. The available method for calculating the IAD in VOF models requires a very fine nodalization of the computational domain whereas, if improved models are used, the IAD could be more easily modeled accounting also for the local turbulence intensity. Such models should consider, in the calculation of the interfacial area characteristic turbulence indicators such as the TKE and the eddy dissipation rate.

The capability of tracking the two-phase flow with such spatial resolution proves the potential of VOF and the hybrid HTC model to also realistically simulate the complex Pressurized Thermal Shock (PTS) phenomenon, a two-phase flow scenario

where cold water touches hot walls. PTS increases the material thermal fatigue, potentially resulting in small cracks in the pipe structure. The phenomenon of PTS is caused by the variation over a short period of time of high thermal stresses due to dilatation or contraction within a system component. Stresses above the material yield strength can arise if the thermal dilatation or contraction is constrained. It could be noticed during both the simulations of the PMK-2 and the TUHH facilities that the temperature of the water touching the pipe walls was oscillating. Using the VOF method the phenomenon of temperature layering can be analyzed as the results of the simulations show. The fact that this effect is caught by the CFD simulation is of potential interest for the application of the hybrid HTC for other transient scenarios.
These local effects observed in the CFD simulations could not be caught with the traditional 1D approach of system codes but on the other hand system code simulations are less computational power-consuming and less prone to simulation crashes or numerically induced variable oscillations as in the case of the CFD simulations.

The hybrid HTC model was also successfully implemented into the German system code ATHLET. System codes are still widely used for the safety assessment of large systems such as industrial scale facilities especially for long lasting transients. The system code simulations represented the measurement data qualitatively well. The idea of employing a quasi-2D computational domain for the ATHLET simulations, with interconnected 1D components using cross-connection objects, requires additional model development and additional validation work. Still this set-up could simulate effects, such as wave growing more realistically in horizontal or nearly horizontal two-phase flow. Nevertheless, ATHLET could predict the overall behavior of the flow quite well and as in the case of the CFD simulation, a direct link between subcooling turbulence on one hand and the flow pattern, on the other hand, could be observed. The advantage of system code analysis of large facilities is the possibility of having an entire complex representations of components. In this way, closed piping systems can be simulated without the need of using sim-

plified BCs, which affect the simulation results, as in the case of CFD analysis. A short sensitivity study based on the influence of the dimensionless numbers Re, Ja, Fr and At has been performed for both the system code simulation results and the experimental data. A similar dependency on the key dimensionless numbers has been observed between computer simulations and recorded data. These simulations even predicted the pressure surges recorded in the different experiments. The concomitant and complementary use of multi-dimensional CFD tools and fast running system codes is the key in analyzing the CIWH phenomenon in piping systems. The sequence of events observed in all computer simulations performed with ANSYS CFX, OpenFOAM and ATHLET presented the typical behavior for a CIWH event:

- As the water injection velocity was low enough, a tongue of liquid formed at the bottom of the pipe,
- Due to steam condensation a counter-current flow is initiated which leads to the instability of the interface and generates a plug,
- The pressure decrease in the entrapped steam pocket, accelerates the water fronts.

This behavior was also described by [33] to be the onset of CIWH events. The key feedbacks of the variables influencing the two-phase flow dynamics typical during a CIWH event are correctly captured by the hybrid HTC model. This is the case both in combination with the VOF in the case of the CFD simulations and the two-fluid model employed in ATHLET. Computer tools, which correctly capture the complex two-phase flow dynamics emerging during a CIWH event, can help to create pressure surge mitigation and avoidance strategies, due to the complementary information delivered by the different approaches. CFD simulations deliver high-resolution results of the complex two-phase flow demanding high computational power. The performed system code simulations proved that in combination with the hybrid HTC model these computer tools are capable to deliver qualitatively good results of the overall flow behavior together with a good prediction of eventual pressure peaks. Still the exact magnitude of the CIWH is difficult to

predict because of the stochastic nature of surface waves which eventually evolve to slugs and the resulting steam pocket entrapment.
An additional variable which has to be investigated for its role in triggering CIWH, is the pump start-up behavior. It was underlined, also during the performed simulations that the slugging can be triggered before the pump reaches its maximum flow rate. As a consequence CIWH event could arise in the start-up phase before the pump delivers enough flow rate to fill the pipe with water.

The newly developed HTC model adds to the predictive capabilities of any two-phase flow computer simulation due to its mechanistic character. Its capabilities to reliably simulate complex two-phase flow dynamics were proven by the validation of CFD and system code simulations against experimental measurement data. Overall system safety enhancements can only be established by replacing as many empirically developed models as possible with mechanistic ones, such as the newly developed hybrid SRT based HTC model. Still the hybrid HTC model needs state of the art models for the best estimate simulation of the complex two-phase flow phenomenon during a CIWH, especially for the calculation of the interfacial area density combined with reliable high order numerical schemes.

Appendix A

Appendix 1 PMK-2 Experiments Series

Table A.1: Experiment matrix of the PMK-2 CIWH-series, performed at the PMK-2 facility in Budapest Hungary.

Run ID [-]	$p[bar]$	$T_{liq}[°C]$	$\Delta T[°C]$	$\dot{m}[kg/s]$	**p increase in the exp. [bar]**	**p increase in the sim. [bar]**
3	9.8	30	149	1.2	129.9	39.4
4	11.5	30	156	0.66	13.9	110.4
5	14.5	25	172	1.01	156.4	112.2
6	15	30	168	1.66	165.5	13.9
7	10.2	17	163	1	23.7	47.1
8	10.9	40	144	1.2	11.1	59.1
9	11	57	127	1.2	20.9	15.5
10	20.1	61	151	1.5	5.8	1.8
11	20.2	72	140	1	71.6	3.7
12	20	50	162	1	80.8	32.3

continued on next page

Table A.1 – continued from previous page

Run ID [-]	$p[bar]$	$T_{liq}[°C]$	$\Delta T[°C]$	$\dot{m}[kg/s]$	**p increase in the exp. [bar]**	**p increase in the sim. [bar]**
13	20.1	26	186	0.7	9.7	5.8
14	20.1	60	152	0.7	3.7	2.9
15	20.2	30	182	1.2	96.3	19.0
16	10	35	145	1	147.0	100.0
17	10.1	40	140	1	125.4	96.6
18	10.1	37	143	1	157.6	83.3
19	11.4	55	125	1	175.2	26.1
20	11.7	53	131	1	117.5	30.8
21	15	72	126	1	197.7	2.0
22	20.1	50	162	1	196.7	33.2
23	20	35	177	1	210.0	25.0
24	23	45	175	1	160.5	13.3
25	10	44	136	1	34.7	24.4
26	30	97	137	1	0.0	4.1
27	30	110	124	0.73	0.0	1.4
28	30	103	131	1.71	3.3	0.4
29	35	110	133	1.71	0.0	0.2
30	35	123	131	1	0.0	0.3
31	35	140	103	0.73	0.0	1.6
32	40	130	120	1	0.0	1.0
33	40	124	126	0.73	0.0	0.8
34	40	120	130	1	0.0	1.2
35	40	68	182	1	0.0	5.0

Bibliography

[1] USNRC. *TRACE V5.0 Theory Manual: Field Equations, Solution Methods, and Physical Models.*

[2] N.E. Todreas and M.S. Kazimi. *NUCLEAR SYSTEMS I, Thermal Hydraulics Fundamentals.* Taylor & Francis, 1990.

[3] H. Austregesilo, C. Bals, A. Hora, G. Lerchl, and P. Romstedt. *ATHLET Mod 2.2 Cycle A Models and Methods GRS - P - 1 / Vol 4 Rev. 2.* GRS, July 2009.

[4] S.C. Ceuca and R. Macián-Juan. CFD Simulation Of Direct Contact Condensation with ANSYS CFX using locally defined Heat Transfer Coefficients. *Proceedings of the 20th International Conference on Nuclear Engineering collocated with the ASME 2012 Power Conference*, 2012.

[5] H.K. Versteeg and W. Malalasekera. *An Introduction to Computational Fluid Dynamics.* Longman Scientific & Technical, 1995.

[6] D. Lucas. Deliverable D 2.1.2: Review of the existing Data Basis For the Validation of Models for PTS. Technical report, Technical report, 2005.

[7] J. Karl and D. Hein. Measuring Water Temperature Profiles at Stratified Flow by means of Linear Raman Spectroscopy. *Proceedings of the Japanese-German Symposium on Multiphase Flow*, 1997.

[8] H.-M Prasser, Gy. Ézsöl, G. Baranyai, and T. Sühnel. Spontaneous Water Hammers in a Steam Line in Case of Cold Water Ingress. *Multiphase Science and Technology*, 20:265–289, 2008.

[9] H. Swidersky, A. Schaffrath, and A. Dudlik. Computational Models to determine Fluiddynamical Transients due to Condensation Induced Water Hammer (CIWH). *Proceedings of the 14th International Topical Meeting on Nuclear Reactor Thermal-Hydraulics (NURETH-14)*, 14, 2011.

[10] C. Urban and M. Schlüter. Optical Investigations on key Phenomena of Condensation Induced Water Hammers. *Proceedings of the 15th International Topical Meeting on Nuclear Reactor Thermal-Hydraulics (NURETH-15)*, 2013.

[11] C. Urban and M. Schlüter. Untersuchungen zu Kondensationsschlägen in Rohrleitungssystemen: Experimentelle Ergebnisse an der Technischen Universität Hamburg-Harburg (in German). *1. Projektstatusgespräch zur BMBF geförderten Nuklearen Sicherheitsforschung*, 2013.

[12] S.C. Ceuca and R. Macián-Juan. Benchmark of Surface Renewal Theory based Heat Transfer Coefficients for the Simulations of Direct Contact Condensation in Pipes using the 1D and 3D Approach. *Proceedings of the 15th International Topical Meeting on Nuclear Reactor Thermal-Hydraulics (NURETH-15)*, 2013.

[13] C. Martin, R. Brown, and J. Brown. *Condensation-Induced Hydraulic Shock Laboratory Study.* American Society of Heating, Refrigeration, and Air Conditioning Engineers - ASHRAE 970-RP, 2007.

[14] M. Ishii and T. Hibiki. *Thermo-fluid Dynamics of Two-phase Flow.* Springer Science+Business Media, Inc., 2006.

[15] John R. Thome. *Engineering Data Book III.* Wolverine Tube, Inc Online, 2010.

[16] J. Weisman and S.Y. Kang. Flow Pattern Transitions in Vertical and Upwardly Inclined Lines. *International Journal Multiphase Flow*, 7:271–291, 1981.

[17] Y. Taitel D. Barenea, O. Shoham and A. E. Dukler. Gas-Liquid Flow in Inclined Tubes: Flow Pattern Transitions for Upward Flow. *Chemical Engineering Science*, 40:131–136, 1985.

[18] O. Baker. Designing for Simultaneous Flow of Oil and Gas. *Oil and Gas Journal*, 53:185–195, 1954.

[19] G.A. Gregory J.M. Mandhane and K. Aziz. A Flow Pattern Map for Gas-Liquid Flow in Horizontal Pipes. *International Journal Multiphase Flow*, 1:537–553, 1974.

[20] Y. Taitel and A.E. Dukler. A Model for Predicting Flow Regime Transitions in Horizontal and near Horizontal Gas-Liquid Flow. *Journal of the American Institute of Chemical Engineers*, 22:47–55, 1976.

[21] S. Koyama H. Haraguchi and T. Fujii. Condensation of Refrigerants HCFC 22, HFC 134a, and HCFC 123 in a Horizontal Smooth Tube (2nd report, Proposal of Empirical Expressions for Local Heat Transfer Coefficient). *Trans. JSME*, 60(574):245–252, 1994.

[22] A. Cavallini, G. Censi, D. Del Col, L. Doretti, G.A. Longo, and L. Rossetto. In-Tube Condensation of Halogenated Refrigerants. *ASHRAE Transactions*, 108:1:146–161, 2002.

[23] A. Cavallini, G. Censi, D. Del Col, L. Doretti, G.A. Longo, L. Rossetto, and C. Zilio. Condensation Inside and Outside Smooth and Enhanced Tubes - A Review of Recent Research. *International Journal of Refrigeration*, 26:1:373–392, 2003.

[24] J. El Hajal J.R. Thome and A. Cavalini. Condensation in Horizontal Tubes, Part 2: New Heat Transfer Model Based on Flow Regimes. *International Journal of Heat and Mass Transfer*, 46:3365–3387, 2003.

[25] J.R. Thome J. El Hajal and A. Cavalini. Condensation in Horizontal Tubes, Part 1: Two-Phase Flow Pattern Map. *International Journal of Heat and Mass Transfer*, 46:3349–3363, 2003.

[26] D.J. Korteweg. Über die Fortpflanzungsgeschwindigkeit des Schalles in elastischen Röhren. (On the velocity of propagation of sound in elastic tubes.). *Annalen der Physik und Chemie, New Series 5*, 5:525–542, 1878.

[27] L. Allievi. Theory of Water Hammer (translated from Italian by E. E. Halmos for the American Society of Civil Engineers, 1925). Technical report, printed by R. Garoni, 1913.

[28] L. Bergeron. *Water Hammer in Hydraulic and Wave Surges in Electricity.* John Wiley and Sons Inc. New York, 1960.

[29] G.R. Rich. Water Hammer Analysis by Laplace Mellin Transformation. *Transaction American Society of Mechanical Engineers*, pages 361–376, 1945.

[30] H.W. Reddick and F.H. Miller. *Advanced Mathematics for Engineer.* John Wiley and Sons Inc. New York, 1957.

[31] A. Sommerfield. *Partial Differential Equations in Physics.* Academic Press New York, 1949.

[32] Y. Chou and P. Griffith. Admitting Cold Water into Steam Filled Pipes without Waterhammer due to Steam Bubble Collapse. *Nuclear Engineering and Design*, 121:367–378, 1990.

[33] P. Griffith. Screening Reactor Steam/Water Piping Systems for Water Hammer, NUREG/CR-6519. Technical report, USNRC, 1997.

[34] J.A. Block et al. An Evaluation of PWR Steam Generator Water Hammer, NUREG-0291. Technical report, USNRC, 1977.

[35] A.B. Jackobek and P. Griffith. Investigation of Cold Leg Water Hammer in a PWR due to the Admission of Emergency Core Cooling during a Small Break LOCA, NUREG/CR-3895. Technical report, USNRC, 1984.

[36] S.C. Lee. Stability of Steam-Water Countercurrent Stratified Flow, NUREG/CR-4416. Technical report, USNRC, 1985.

[37] H.-M Prasser, Gy. Ézsöl, and G. Baranyai. Water Hammer Tests, Condensation caused by Cold Water Injection into Main Steam-Line of VVER-440-type PWR - Quick-Look Report (QLR). Technical report, WAHALoads project deliverable D48, 2004.

[38] H.-M Prasser, Gy. Ézsöl, and G. Baranyai. Water Hammer Tests, Condensation caused by Cold Water Injection into Main Steam-Line of VVER-440-type PWR Ű Data Evaluation Report (DER). Technical report, WAHALoads project deliverable D51, 2004.

[39] W. Schnellhammer. Rohrleitungskräfte bei Überspeisung der Frischdampfleitung infolge Fehlöffnens eines Hauptspeisewasserregelventils - Arbeitsbericht (in german). Technical report, AREVA Nuclear Power, 2008.

[40] S. Dirndorfer, M. Dörfler, H. Kulisch, and A. Malcherek. Condensation-Induced Water Hammer - Overview and Own Experiments. *Proceedings of the 14th International Topical Meeting on Nuclear Reactor Thermal-Hydraulics (NURETH-14)*, 14, 2011.

[41] N. Joukowsky. Über den hydraulischen Stoss in Wasserleitungsröhren (On the Hydraulic Hammer in Water Supply Pipes). *Mémoires de l'Académie Impériale des Sciences de St.-Pétersbourg, Series 8*, 9(5), 1900.

[42] D. Lucas, D. Bestion, E. Bodèle, P. Coste, M. Scheuerer, F. D'Auria, D. Mazzini, B. Smith, I. Tiselj, A. Martin, D. Lakehal, J.-M. Seynhaeve, R. Kyrki-Rajamäki, M. Ilvonen, and J. Macek. An Overview of the Pressurized Thermal Shock Issue in the Context of the NURESIM Project. Technical report, European Union, 2009.

[43] D. Lucas, D. Bestion, P. Coste, P. Pouvreau, Ch. Morel, A. Martin, M. Boucker, E. Bodele, M. Schmidtke, M. Scheuerer, B. Smith, M. T. Dhotre,

B. Niceno, D. Lakehal, M. C. Galassi, D. Mazzini, F. D'Auria, Z. Bartosiewicz, J.-M. Seynhaeve, I. Tiselj, L. Łtrubelj, M. Ilvonen, R. Kyrki-Rajamäki, V. Tanskanen, M. Laine, and J. Puustinen. Main Results of the European Project NURESIM on the CFD-Modelling of Two-Phase Pressurized Thermal Shock (PTS). *Kerntechnik*, 74:238–242, 2009.

[44] H. Ruile, J. Karl, and D. Hein. Kühlmittelerwärmung bei Direktkontaktkondensation an horizontalen Schichten und vertikalen Streifen zur Quantifizierung des druckbelasteten Thermoschocks. Technical report, BMFT-Forschungsvorhaben 1500906, Abschlußbericht, Lehrstuhl für Thermische Kraftanlagen, TU München, Germany., 1995.

[45] ECORA. Two-Phase Flow Water Hammer Transients and Induced Loads on Materials and Structures of Nuclear Power Plants (Ecora Project Report). Technical report, Technical report, 2004.

[46] Y. Egorov, M. Boucker, Martin A, S. Pigny, M. Scheuerer, and S. Willemsen. Validation of CFD Codes with PTS-Relevant Test Cases. Technical report, Technical report, 2004.

[47] G. Kocamustafaogullari and M. Ishii. Foundations of the Interfacial Area Transport Equation and its Closure Relations. *International Journal Heat and Mass Transfer*, 38:481–493, 1995.

[48] C. M. Rhie and W. L. Chow. A Numerical Study of the Turbulent Flow past an Isolated Airfoil with Trailing Edge Separation. *AIAA Journal*, 21:1525–1532, 1983.

[49] G. Lerchl and H. Austregesilo. *ATHLET Mod 2.2 Cycle A User's Manual GRS - P - 1 / Vol 1 Rev. 5.* GRS, July 2009.

[50] H. Austregesilo and K. Trambauer. Modelling of the Interfacial Area Concentration in the System Code ATHLET. *Proceedings of the 11th International Topical Meeting on Nuclear Reactor Thermal-Hydraulics (NURETH-11)*, 2005.

[51] C.W. Hirt and B.D. Nichols. Volume of Fluid (VOF) Method for the Dynamics of Free Boundaries. *Journal of Computational Physics*, 39:207–225, 1981.

[52] H. Rusche. Computation Fluid Dynamics of Dispersed Two-Phase Flow at High Phase Factions. Technical report, PhD Thesis, University of London UK, 2002.

[53] R. I. Issa. Solution of the Implicit Discretized Fluid Flow Equations by Operator Splitting. *Mechanical Engineering Rep.*, FS:82–15, 1982.

[54] B. E. Launder and D. B. Spalding. The Numerical Computation of Turbulent Flows. *Comput. Methods Appl. Mech. Eng.*, 3:269–289, 1974.

[55] D.C. Wilcox. *Turbulence Modeling for CFD*. DCW Industries Inc., 1998.

[56] R. Higbie. The Rate of Absorption of a Pure Gas into a Still Liquid during a Short Time of Exposure. *Transactions of the American Institute of Chemical Engineers*, 31:365–389, 1935.

[57] P.V Danckwerts. Significance of Liquid- Film Coefficients in Gas Absorption. *Industrial and Engineering Chemistry*, 43:1460–1467, 1951.

[58] H.L. Torr and J.M. Marchello. Film-Penetration Model for Mass and Heat Transfer. *Journal of the American Institute of Chemical Engineers*, 4:97–101, 1958.

[59] S. Banerjee. A Surface Renewal Model for Interfacial Heat and Mass Transfer in Transient Two-Phase Flow. *International Journal Multiphase Flow*, 4:571–573, 1978.

[60] R.B. Duffey and E.D. Hughes. Gas Mass Transfer for Stratified Flows, BNL–61801(Rev.6/95). Technical report, DOE, 1995.

[61] W.J. Brtko and R.L.Kabel. Transfer of Gases at Natural Air-Water Interfaces. *Journal of Physical Oceanography*, 8:543–556, 1978.

[62] E.D. Hughes and R.B. Duffey. Direct Contact Condensation and Momentum Transfer in Turbulent Separated Flows. *International Journal Multiphase Flow*, 17:599–619, 1991.

[63] L. Shen, G.S. Triantafyllou, and D.K.P. Yue. Turbulent Diffusion near a Free Surface. *Journal of Fluid Mechanics*, 407:145–166, 2000.

[64] N. I. Kolev. *Multiphase Flow Dynamics II.* Springer, 2007.

[65] N. I. Kolev. *Multiphase Flow Dynamics I.* Springer, 2007.

[66] M. Scheuerer. Selection of PTS-Relevant Test Cases. Technical report. Technical report, European Commission 5th EURATOM Framework Programme 1998-2002, 2002.

[67] H.-M Prasser, A. Böttger, and J. Zschau. A new Electrode-Mesh Tomograph for Gas-Liquid Flows. *Flow Measurement and Instrumentation*, 9:111–119, 1998.

[68] I.F. Barna, A.R. Imre, G. Baranyai, and Gy. Ézsöl. Experimental and Theoretical Study of Steam Condensation Induced Water Hammer Phenomena. *Nuclear Engineering and Design*, 240:146–150, 2010.

[69] E. Carpintero-Rogero. *Experimental Investigation of Developing Plug and Slug Flows.* PhD thesis, Technische Universität München, Germany, 2009.

[70] S.G. Bankoff and H.J. Kim. Local Condensation Rates in Nearly Horizontal Stratified Countercurrent Flow of Steam and Cold Water. *Heat Transfer AIChE Symposium Series*, 79:225:209–223, 1983.

[71] H.J. Kim and S.G. Bankoff. Local Heat Transfer Coefficients for Condensation in Stratified Countercurrent Steam-Water Flows. *Journal of Heat Transfer*, 105:706–711, 1983.

[72] S.C. Lee and S.G. Bankoff. Stability of Steam-Water countercurrent Flow in an Inclined Channel: Part II - Condensation-Induced Waterhammer, NUREG/CR-2289. Technical report, USNRC, 1981.

[73] I.S. Lin, S.G. Bankoff, R.S. Tankin, and M.C. Yuen. Cocurrent Steam/Water Flow in a Horizontal Channel. *Journal of Heat Transfer*, 106:900–902, 1984.

[74] S.C. Lee and S.G. Bankoff. Parametric effects on the onset of flooding in flat-plate geometries. *International Journal of Mass Transfer*, 27:10:1691–1700, 1984.

[75] S.G. Bankoff and S.C. Lee. Condensation in Stratified Flow. *Multiphase Science and Technology*, 3:1-4:398–422, 1984.

[76] P. Griffith and J.R Silva. Steam Bubble Collapse Induced Water Hammer in Draining Pipes. *Proceedings of the Pressure Vessels and Piping Conference (PVP)*, 231:115–119, 1992.

[77] R.W. Bjorge and P. Griffith. Initiation of Water Hammer in horizontal and nearly horizontal Pipes containing Steam and sub-cooled Water. *ASME Journal of Heat Transfer*, 106:835–840, 1984.

[78] Y. Chou and P. Griffith. Avoiding Steam-Bubble-Collapse-Induced Water Hammers in piping Systems, EPRI Research Project NP-6647. Technical report, EPRI, 1997.

[79] S. Komori, R. Nagaosa, and Y. Murakami. Turbulence Structure and Mass Transfer across a sheared Air-Water Interface in Wind-Driven Turbulence. *Journal of Fluid Mechanics*, 249:161–193, 1993.

[80] S.V. Patankar. *Numerical Heat Transfer and Fluid Flow.* Taylor & Francis, 1980.

[81] S. Banerjee, D. S. Scott, and E. Rhodes. Mass Transfer to Falling Wavy Liquid Films in Turbulent Flow. *Ind. Engng Chem. Fundam.*, 7:22–26, 1968.

[82] N.E. Todreas and M.S. Kazimi. *NUCLEAR SYSTEMS II, Elements of Thermal Hydraulic Design.* Taylor & Francis, 1990.

[83] P. Saha. An Evaluation of Condensation-Induced Wter Hammer in Preheat Steam Generator, NUREG/CR-1606. Technical report, USNRC, 1980.

[84] R.W. Bjorge. Initiation of Water Hammer in Horizontal or Nearly-Horizontal Pipes Containing Steam and Subcooled Water, PhD-Thesis. Technical report, MIT, Department of Mechanical Engineering, 1983.

[85] T. Fujii and K. Akagawa. Analysis of Water Hammer in Bubbly Flows (1st Report, Two-component, Two-phase Flow. *Bulletin of JSME*, 29:1746–1751, 1986.

[86] A. Dudlik and A. Schaffrath. Forschungsantrag Untersuchungen zu Kondensationsschlägen in Rohrleitungssystemen - Condensation Induced Water Hammer, CIWA, Rev.1. Technical report, Fraunhofer UMSICHT, 2010.

[87] S.C. Ceuca and R. Macián-Juan. Validation of a Hybrid Surface Renewal Theory Based HTC Model for the Simulation of Condensation Induced Water Hammer. *Proceedings of the 21th International Conference on Nuclear Engineering*, 2013.

[88] *ANSYS CFX User Manual, Release 14.5.* ANSYS, 2014.

[89] *OpenFOAM User Manual, Version 1.7.1.* OpenFOAM, 2010.